Design, Manufacturing, and Testing of an Active Twist Rotor

by

SangJoon Shin

B.S., Aerospace Engineering, Seoul National University (1989)

M.S., Aerospace Engineering, Seoul National University (1991)

Submitted to the Department of Aeronautics and Astronautics
in partial fulfillment of the requirements for the degree of

Master of Science in Aeronautics and Astronautics

at the

MASSACHUSETTS INSTITUTE OF TECHNOLOGY

June 1999

© Massachusetts Institute of Technology 1999. All rights reserved.

Author .....
Department of Aeronautics and Astronautics
May 12, 1999

Certified by .....
Carlos E. S. Cesnik
Assistant Professor of Aeronautics and Astronautics
Thesis Supervisor

Accepted by .....
Jaime Peraire
Chairman, Department Graduate Committee

Aero

MASSACHUSETTS INSTITUTE OF TECHNOLOGY
JUL 15 1999
LIBRARIES

Design, Manufacturing, and Testing of an Active Twist Rotor

by

SangJoon Shin

Submitted to the Department of Aeronautics and Astronautics
on May 12, 1999, in partial fulfillment of the
requirements for the degree of
Master of Science in Aeronautics and Astronautics

Abstract

An Active Twist Rotor (ATR) is developed for future implementation of the individual blade control for vibration and noise reduction in helicopters. The rotor blade is integrally twisted by direct strain actuation using active fiber composites (AFC). In order to design and analyze an active blade, a general framework is proposed. A multi-cell thin-walled active composite beam model is developed. The model is validated against a combination of other theoretical models and experimental data. Actuation trend studies are conducted by examining the formulation, and the results are verified by numerical examples. Design requirements are proposed by combining general ones applicable to passive model-scaled rotor blade and specific ones to the current ATR blade. A design flowchart is established for the current design task of the ATR blade since it enables systematic handling of a number of the parameters. Several different concepts of ATR candidates are suggested, and compared with each other with regard to the requirements. Other design aspects such as manufacturing simplicity and cost-effectiveness are also considered in the process. The final design is selected, and final adjustments are added to it in order to simplify its manufacturing. A prototype blade is manufactured in accordance with the final design. A couple of testing articles are fabricated in advance to the full-span prototype in order to debug the manufacturing process. Various tests are conducted with the testing articles and the final prototype to verify the design and correlate with model predictions. A maximum static tip twist of 1.5° (peak-to-peak) was achieved at half of the designed operating electric field before five of the 24 AFC packs failed. Electrical breakdown of the embedded active material caused degradation of twist actuation in the prototype blade, and the causes are presently under investigation. The ATR prototype blade is leading to a complete fully-articulated four-blade active twist rotor system for future wind tunnel tests.

Thesis Supervisor: Carlos E. S. Cesnik
Title: Assistant Professor of Aeronautics and Astronautics

Acknowledgments

I greatly appreciate Dr. Carlos E. S. Cesnik, who is my advisor, for his guidance and supervision throughout the entire process of this thesis. Without his encouragement, this thesis would not exist. I would also like to express my gratefulness to Dr. Nesbitt W. Hagood and Dr. Steven R. Hall, for sharing their profound knowledge with me regarding any problems occurred during the process.

I am grateful to Dr. John Rodgers and Mr. Eric Prechtl, for their help and effort on the manufacturing and experiments. Special thanks to Mr. John Kane for letting me work in the excellent laboratory environment.

I would definitely like to thank Dr. W. Keats Wilkie and Mr. Paul Mirick, for the financial support and kind help on the manufacturing, and also Mr. Matthew L. Wilbur for supporting with CAMRAD II results.

I would also thank Mr. Woo-Sok Chang and Dr. Jae-Hyuk Oh, for their encouragement and friendship, which helped me to carry out this thesis.

I would appreciate my parents for the endless love and support, and also, my sister, brother-in-law, and brother. Especially, I would like to thank my fiancee, JeeYoung, for her encouragement and understanding.

Contents

1 Introduction **23**

1.1 Helicopter Vibrations 23

1.2 Helicopter Vibration Alleviation 24

1.3 Previous Work Related with Integral Twist Actuation 26

1.4 Present Work 27

2 Active Blade Structural Analysis **29**

2.1 Overview 29

2.2 Cross-section Analysis 30

2.3 1-D Beam Analysis 37

2.3.1 Extended active beam equations 38

2.3.2 Inertial properties 43

2.4 Three-dimensional Stress Recovery Formulation 45

3 Validation of the Proposed Active Structural Model **47**

3.1 Overview 47

3.2 Box-Beam Case 48

3.3 Single-Cell Active Blade Results 49

3.3.1 Cross-section results 49

3.3.2 Beam results 52

3.4 Two-Cell Active Blade Results 54

4 Study on the Actuation Constants **59**

4.1 Overview . . . 59
4.2 Analytical Examination of Actuation Components . . . 60
4.3 Numerical Examination of Actuation Components . . . 63
4.4 Twist-Related Relationship from the Present Formulation . . . 65
4.5 Twist Actuation Results . . . 67
4.5.1 Two-cell box beam cases . . . 67
4.5.2 ATR blade cases . . . 68

5 Design Requirements and Procedure 75
5.1 Overview . . . 75
5.2 Design Requirements . . . 75
5.3 Design Flowchart . . . 81
5.4 Structural Integrity Substantiation . . . 85

6 ATR Design Results 89
6.1 Overview . . . 89
6.2 Active Spar Candidates and Variations . . . 90
6.2.1 Analysis of the active spar candidates . . . 90
6.2.2 Variations of the active spar candidates . . . 95
6.3 Analysis of the Active Fairing Candidates . . . 96
6.4 Analysis of the Active Box Beam Candidates . . . 100
6.5 Selection of the Final Design and Improvement . . . 104

7 ATR Prototype Blade Manufacturing 107
7.1 Overview . . . 107
7.2 Miscellaneous Items . . . 107
7.2.1 Integral blade root . . . 107
7.2.2 AFC packs . . . 108
7.2.3 Flexible circuit . . . 110
7.2.4 Foam cores and ballast weights . . . 111
7.3 Testing Articles . . . 111

7.4 Prototype blade 113
7.5 Summary of Manufacturing Issues and Recommendations 117

8 ATR Prototype Blade Testing **119**
8.1 Overview 119
8.2 Blade Root Test 120
8.3 Blade Torsional Stiffness Measurement 121
8.4 Bench Actuation Test 124
8.5 Frequency Response Test 126

9 Conclusions and Recommendations **129**
9.1 Summary 129
9.2 Conclusions 131
9.3 Recommendations 132

A Cross-Sectional Formulation **135**

B 1-D Blade Formulation **139**

C Material Properties **141**

D Detailed Dimensions of the ATR Prototype Blade **143**

E Activities Listing of the Prototype Blade Manufacturing **151**

List of Figures

1-1 Aerodynamic environment in forward flight 24

2-1 Two-cell thin-walled closed-section beam 31
2-2 Branches for integration of a two-cell thin-walled cross section 36
2-3 Blade frames 39

3-1 Two-cell thin-walled box beam definition 49
3-2 Single-cell active blade cross section (NACA 0012) 51
3-3 Single-cell active blade tip twist 52
3-4 Single-cell active blade twist distribution 53
3-5 Schematic diagram of the complete CH-47D active blade section [28] . 55
3-6 Schematic diagram of the CH-47D spar [28] 55

4-1 Flapwise deflection of the single-cell active blade under bending actuation 64
4-2 Baseline configurations of two-cell box beams 67
4-3 Schematic diagram of the ATR blade design 69
4-4 Twist actuation result of two-cell ATR blade 70
4-5 Baseline configuration of D-spar single-cell derivative beam (dimensions are in inches) 71
4-6 Baseline configuration of single-cell airfoil-shaped derivative beam (dimensions are in inches) 71
4-7 Twist actuation result of D-spar single-cell beam 72
4-8 Twist actuation result of single-cell airfoil-shaped beam 73

5-1 Original design of the baseline passive blade 81

5-2 Flowchart of the ATR blade design tasks 82
5-3 Flowchart of the ATR blade design tasks (cont'd) 83
5-4 CAMRAD II prediction of flapwise bending moment 86
5-5 CAMRAD II prediction of chordwise bending moment 87
5-6 CAMRAD II prediction of torsional moment 87

6-1 Schematic diagram of the several ATR design candidates 90
6-2 Schematic diagram of the active spar candidate (all dimensions are in inches). 91
6-3 Twist actuation trend for the active spar ATR candidates with respect to the number of AFC packs embedded across the thickness 92
6-4 Schematic diagram of the active box beam candidate (all dimensions are in inches). 100
6-5 Schematic diagram of the final selected design 106

7-1 Drawing of 3-dimensional blade root stack 108
7-2 Detail of the blade root construction 109
7-3 Final AFC pack design used in the ATR prototype blade 109
7-4 AFC packs being inserted during the prototype manufacturing 110
7-5 Strain gauges attached upon the foam cores 114
7-6 Blade mold in which the spar assembly is sitting with dummy fairing backup and strain gauge wires are extracted at root along the small trough 115
7-7 Prototype spar sitting inside the blade mold clamped with the fixtures at the leading edge and the tip 116
7-8 Final ATR prototype blade 117

8-1 Testing article showing catastrophic failure under tensile loading . . . 121
8-2 ATR prototype clamped at root with the rig 122

8-3 ATR prototype blade clamped at the testing rig with the laser sensors illuminating the reflecting strips (weights hung at the end of cables for torque the blade tip are also shown). 123
8-4 Torsional stiffness results for the spar and full blade - comparison between measurements and theoretical results 123
8-5 Distribution diagram of each specific AFC pack in the prototype blade 125
8-6 Actuation results of the ATR prototype blade having only 19 out of the 24 AFC packs working (voltage levels are peak-to-peak, no DC offset) 126
8-7 ATR prototype blade tip twist response as function of applied electric field (no DC offset) 127
8-8 ATR prototype blade bench response of embedded strain gauges vs. AFC excitation frequency 128
8-9 ATR prototype blade bench tip twist actuation response vs. AFC excitation frequency 128

D-1 Cross-section schematic of the ATR blade and the dimension of the ballast weights 144
D-2 Cross-section schematic of the front spar foam core (dimensions include oversize) 145
D-3 Cross-section schematic of the fairing foam core (dimensions include oversize) 145
D-4 Spanwise distribution of the 24 AFC packs at the top and bottom surface of ATR prototype blade 146
D-5 Drawing of the three E-Glass skin plies which cover the whole span (all dimensions are in inches) 147
D-6 Drawing of the auxiliary S-Glass pieces which fill the gap between inboard/outboard end and the first/last AFC pack space (all dimensions are in inches) 147
D-7 Drawing of six-layer flexible circuit showing the location of each solder pads 148

D-8 Location of the strain gauge bridges along the span of ATR prototype blade 149

List of Tables

3.1 Properties of AS4/3506-1 Graphite/epoxy – "L" direction is along the fibers and "N" is normal to laminate 48

3.2 Non-zero stiffness results (N, N m, N m^2) for two-cell box beam (1 extension; 2 torsion; 3, 4 bending) 49

3.3 Material properties used in the single-cell active blade (Q_{ij} are the laminate reduced stiffness of the actuator pack) 50

3.4 Non-zero stiffness (N, N m, N m^2) and forcing vector (N, N m) results for airfoil-shaped cross section – (K_{ij}: 1 extension; 2 torsion; 3, 4 bending) 51

3.5 Non-zero stiffness (N, N m, N m^2) and forcing vector (N, N m) results for CH-47D D-spar only – (K_{ij}: 1 extension; 2 torsion; 3, 4 bending) . 56

3.6 Non-zero stiffness (N, N m, N m^2) and forcing vector (N, N m) results for CH-47D active blade section (front D-spar + fairing) – (K_{ij}: 1 extension; 2 torsion; 3, 4 bending) 56

3.7 Twist actuation rate comparison for CH-47D active blade (D-spar only and full cross-section: analyses and experiment) 57

4.1 Analytical expressions of the actuation components for single-cell active beam 61

4.2 Numerical comparison of actuation vector components for airfoil-shaped beam 64

4.3 Analytical results of two-cell box beam 68

5.1 General properties of the existing baseline rotor 76

5.2 Structural properties of the existing baseline rotor blade (at $0.5R$) . . 76
5.3 Summary of rotor blade scaling parameters 78

6.1 Lay-up information of four active spar candidates 91
6.2 Analysis results of four active spar candidates (^{1} cantilevered boundary condition at root) 93
6.3 Comparison of candidate No. 2 against requirement 94
6.4 Lay-up information of the variations of active spar candidates 97
6.5 Analysis results of the variations of active spar candidates 98
6.6 Ultimate strength data of AFC material 98
6.7 Lay-up information of the active fairing candidates 99
6.8 Analysis results of the active fairing candidates 99
6.9 Lay-up information of the active box beam candidates 101
6.10 Analysis results of the active box beam candidates 103
6.11 Result of the final design compared with requirements 105

8.1 Tensile load test on 3/4-radius blade spar (blade station in inches) . . 120
8.2 Sequence and condition of AFC pack failure during the actuation test 125
8.3 Twist actuation of the ATR prototype blade ($\circ/m, 2,000$ $V_{pp}/0$ V_{DC}) 125

9.1 Hover test plan for the ATR prototype blade (TDT at Langley) . . . 133

C.1 Properties of the AFC packs 141
C.2 Properties of the composite materials used in the ATR protype blade 141
C.3 Capacitance history of the AFC packs 142

D.1 Part list of ATR prototype blade lay-up 143

Nomenclature

$\mathbf{a}$	global frame attached to the hub
A_e	inner area enclosed by all sections
A_{ei}	inner area enclosed by the i-th cell only
$A(s)$	axial stiffness in the shell frame
$A^{(a)}(s)$, $C^{(a)}(s)$	actuation contribution to the shell energy functional
$\mathbf{b}$	undeformed reference frame of the blade
$\mathbf{B}$	deformed reference frame of the blade
$B(s)$	coupling between axial and shear stiffness in the shell frame
$C(s)$	shear stiffness in the shell frame
C^{ba}	transformation matrix from a to b
C^{Ba}	transformation matrix from a to B
C	rotation matrix, product of C^{ab} and C^{Ba}
d	characteristic dimension of the beam cross section
d_{kij}	piezoelectric electromechanical coupling tensor
$D^{\alpha\beta\gamma\delta}$	two-dimensional Hookean tensor
e_1	unit vector $[1,\ 0,\ 0]^T$
E^{ijkl}	Hookean tensor
E_k	electric field vector
f_a	external forces vector
f_{u_i}, f_{ψ_i}, f_{F_i} f_{M_i}, f_{P_i}, f_{H_i}	beam element functions explicitly integrated

F_1	beam axial force
$F_1^{(a)}$	actuation component of beam axial force
F_B	internal force column vector in the **B** frame
$F_B^{(a)}$	actuation column vector for internal force
$g_1(s)$	warping due to axial strain
$g_2(s),\ g_3(s)$	warping due to bending strain
G_{eff}	effective wall shear stiffness
G_{LT}	shear modulus in the ply coordinate
$G(s)$	torsion-related warping
h	thickness of the shell surface
H_B	angular momentum column vector
I	3×3 inertial matrix
$[J]$	Jacobian matrix in the Newton-Raphson formulation
K	kinetic energy density per unit span of the blade
$[K]$	general 6×6 stiffness matrix
K_{ij}	beam stiffness components
L	length of the shell
Δl_i	length of the i-th spanwise beam element
m	blade mass per unit span length
m_a	external moment vector
M_1	beam torsional moment
$M_2,\ M_3$	beam bending moments
$M_1^{(a)}$	actuation component of beam torsional moment
$M_2^{(a)},\ M_3^{(a)}$	actuation components of beam bending moments
M_B	internal moment column vector in the **B** frame
$M_B^{(a)}$	actuation column vector for internal moment
$\mathbf{n}$	normal vector of an arbitrary point perpendicular to the surface
N	number of blades

$N_{\alpha\beta}$	stress tensor in the shell frame
P_B	linear momentum column vector
$\mathbf{r}$	position vector of an arbitrary point in the surface
r_t	projection of the position vector $\mathbf{r}$ on $\mathbf{t}$
r_n	projection of the position vector $\mathbf{r}$ on $\mathbf{n}$
R	radius of curvature of the shell middle surface
$s,\ \xi$	coordinate with respect to the middle surface point along the surface
s^E_{ijkl}	elastic compliance tensor at constant electric field
$\mathbf{t}$	tangent vector of an arbitrary point along the surface
u_a	displacement vector measured in the $\mathbf{a}$ frame
$u_i(x)$	displacement field of the cross-section reference point
$u_i,\ \theta_i,\ F_i$ $M_i,\ P_i,\ H_i$	constant vectors of the corresponding quantities at each node i
U	energy density of a three-dimensional elastic body
$\hat{U}$	approximation of the energy density U
$v_1,\ v_s,\ v_\xi$	displacement field of an arbitrary point in the shell frame
$v_1^{(a)}(s)$	actuation contribution to the out-of-plane displacement
v_a	initial velocity of a generic point on the $\mathbf{a}$ frame
V_B	linear velocity column vector in the $\mathbf{B}$ frame
w_1	out-of-plane warping function
w_a	initial angular velocity of a generic point on the $\mathbf{a}$ frame
$\overline{\delta W}$	virtual work of applied loads per unit span
x	beam axial coordinate
X	column matrix of the unknowns in one-dimensional beam formulation
$\bar{X}$	steady components of the unknowns X
$\check{X}(t)$	transient components, or the perturbed motion

$y,\ z$	Cartesian coordinates with respect to the reference point in the cross section
Z_a	arbitrary vector Z represented with respect to **a** frame
Z_b	arbitrary vector Z represented with respect to **b** frame
Z_B	arbitrary vector Z represented with respect to **B** frame
$\tilde{Z_{jk}}$	$= Z_i\ e_{ijk}$
$\gamma,\ \kappa$	generalized strain column vectors
$\overline{\gamma}_{ij}$	shell in-plane strain
Δ	3×3 identity matrix
$\varepsilon_{ij}^{(m)}$	mechanical strain tensor
ε_{ij}	total strain tensor
$\varepsilon_{ij}^{(nm)}$	non-mechanical strain tensor
θ	rotation vector expressed in terms of Rodrigues parameters
ξ	local coordinate of each beam finite element
$\overline{\delta \mathsf{A}}$	virtual action at the ends of the beam and at the ends of the time interval
$\delta\Pi_a$	variational quantity of total potential energy in the **a** frame
$\delta\Pi_i$	$\delta\Pi$ over the i-th element
ρ	weight density of the blade
ρ_{ij}	shell surface curvature
σ_{ij}	stress tensor
$\phi(x)$	twist angle of the cross section
Φ	shell energy per unit middle surface area
Φ_i	ith-order approximation of the shell energy functional
ψ	blade azimunth angle
$\Psi(E_3)$	quadratic terms in the electric field
Ω_B	angular velocity column vector in the **B** frame
$< (\bullet) >$	$= \int_{-h(s)/2}^{+h(s)/2} (\bullet)\ d\xi$

$'$	derivative with respect to the beam span coordinate, x_1
$\oint(\,)\,ds$	anticlockwise integration along all the sections
$\oint_i(\,)\,ds$	anticlockwise integration along the i-th cell section only
*	geometrically exact kinematical quantity in the $\mathbf{a}$ frame
$\hat{(\,)}$	boundary values of the corresponding quantities

Chapter 1

Introduction

1.1 Helicopter Vibrations

The rotor system is the main source of helicopter vibrations, and the resulting vibratory load becomes a dominant factor of reducing the life of fatigue-critical components. These vibrations also limit the performance of the helicopters such as forward flight speeds, and tend to decrease payload due to the addition of extra vibration-alleviation devices.

The primary source of the rotor system vibration is oscillatory airloads acting on the rotor blades, and these oscillatory airloads are caused by the unsteady aerodynamic environment of the main rotor especially in forward flight.

A typical forward flight aerodynamic environment of the helicopter main rotor is illustrated in Figure 1-1, where helicopter flight velocity adds to the blade element rotating velocities on the advancing side ($\psi = 90°$), and subtracts from it on the retreating side ($\psi = 270°$). Therefore, the aerodynamic environment is characterized as follows: high tip Mach number on the advancing side, and blade stall effects on the retreating side. A reverse flow region is also generated on the retreating side. Such a complicated environment results in an instantaneous asymmetry of the aerodynamic loads acting among the blades at different azimuthal locations. The vibratory response of a flexible blade structure adds more complexity on the air loads asymmetry. This asymmetry is transmitted to the fuselage at the frequency of N/rev,

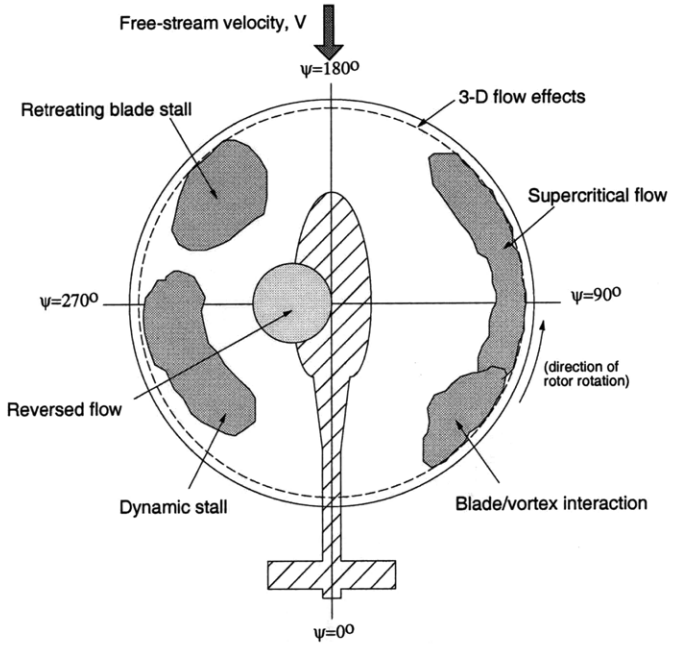


Figure 1-1: Aerodynamic environment in forward flight

where N is the number of blades in the rotor. This mechanism becomes a primary source of fuselage excitation.

The rotor blades usually have a built-in twist which is to relieve the lift difference between the inboard and outboard sections when hover, and it gives an advantage of increasing payload. However, the larger the rotor blades have the built-in twist, the more severe fuselage vibrations become in forward flight. Therefore, helicopter designers traditionally take a trade-off value of the built-in twist considering between the hover performance and the forward flight vibrations.

1.2 Helicopter Vibration Alleviation

There has been much effort to alleviate the vibration from the early stages of helicopter development [1, 2]. The vibration alleviating methodologies employed by the helicopter designers may be categorized into the following three groups:

1. Varying passive structural properties of the rotor system or fuselage by tuning its dynamic characteristics;

2. Employing passive or active vibration absorbing devices either at the rotating system or the fixed system;

3. Direct modification of the excitation forces, principally aerodynamic forces to reduce vibration.

Among these methodologies, employing vibration absorbers has been widely adopted by the helicopter industry, and the absorbers produce counteracting inertial and damping forces [3]. However, such mechanisms introduce significant cost, in terms of weight and complexity, as well as potential aerodynamic performance degradation. Therefore, an effort to modify directly the excitation forces has been suggested, that is, to eliminate or reduce vibrations by modifying unsteady aerodynamic forces acting on the rotor blades.

Higher harmonic control (HHC), one of such ideas, is accomplished by manipulating a conventional swashplate to enable blade pitch control of a higher multiple frequency than an integer multiple of rotating frequency, i.e., $(kN \pm 1)/rev$. Individual blade control (IBC) installs a pitch actuator in each blade rather than modulating the swashplate, and allows for blade pitch control at arbitrary frequencies.

HHC with a conventional swashplate presents limitations associated with weight penalty and hydraulic power requirement as well as severe fatigue induced at actuator components. On the contrary, by using active material actuators installed directly in the blade, IBC can be implemented without great increase in weight and complexity [4]. Such active material actuators, employed either by discrete flap-actuation mechanisms or embedded along the blade to induce twist, also have the advantage of requiring only electrical power to operate. Especially, the induced-strain twist rotor based on embedded active fiber composites (AFC) is mechanically simple and does not require additional device into the rotating system. Recent experimental research on the strain-induced twist rotor blade has shown that high levels of twist actuation are achievable [5, 6].

1.3 Previous Work Related with Integral Twist Actuation

There have been several approaches in the literature to take advantage of active materials for individual blade control [2, 4]. The one of interest in the present study is the integral actuation through the use of active fiber composites (AFC) with interdigitated electrodes [7]. This actuator concept provides a feasible way of integrally actuate a rotor blade instead of the direct use of piezoceramic crystals.

The same concept using piezoceramic crystals was studied by Chen and Chopra [8, 9] in a 6-ft diameter 2-bladed Froude-scaled rotor model with banks of piezoceramic crystal elements in $\pm 45°$ embedded in the upper and lower surfaces of the test blade. They also developed a simple composite beam model with piezoelectric actuator in order to predict the static response. There have been improvements in the actuation levels by using dual-layer actuators and the maximum experimental tip twist actuation obtained was of the order of 0.5° still below the 1° to 2° necessary for the possible vibration reduction applications.

On the other hand, preliminary results from the AFC concept obtains the level of authority needed from the actuator. Basic material characterization and proof of concept of an integral twisted-actuated rotor blade have been under investigation at MIT's Active Materials and Structures Laboratory [5, 10]. Experimental work related with active twist rotor blades based on such AFC plies has also been conducted. In a bench test of a 1/16th Froude-scaled model rotor blade, duPlessis and Hagood [11] have reported achieving static twist of up to 1.4°. Rodgers, Hagood and Weems [5] also have reported achieving twist actuation rates of up to 1.3°/m in the preliminary testing of a 1/6th Mach-scaled active CH-47D rotor blade. In the consecutive hover testing, it was also proved that the concept of AFC technologies is enough for withstanding the combined steady centrifugal loads and unsteady aerodynamic loads acting on the blade at the worst loading condition [6].

Several analytical models were developed to analyze and design such active twist rotor blades (Song and Librescue [12]; duPlessis and Hagood [11]; Wilkie, Belvin and

Park [13]), and these models are all based on the single-cell closed-section passive beam structural model suggested by Rehfield [14] with its assumed displacement field in the cross-section. However, there is no guarantee for consistent accuracy on the result of a non-asymptotical (passive) composite cross-sectional model theory (see, for example, Cesnik and Hodges [15]).

Wilkie, Belvin and Park [13] have presented an aeroelastic analysis of a helicopter rotor blade in hover with active twist capabilities, and showed a possibility of vibration reduction with a simple scheme of open-loop twist control. Wilkie [16] also suggested a closed-loop control of twist actuation as future research to reduce the vibrations.

Derham and Hagood [17] examined the vibration reduction potential of a proposed 1/6th Mach-scaled model rotor using a modified version of Boeing Helicopter's proprietary comprehensive rotor analysis code. This analysis indicated that 70% to near 100% reductions in the primary frequency component of the vertical hub shear load could be obtained by applying an appropriately phased twisting actuation moment.

1.4 Present Work

The objective of this thesis is to consistently analyze, design, and manufacture a prototype Active Twist Rotor (ATR) blade in order to explore helicopter vibration reduction capabilities. As the first step, an analytical model of an active beam structure is developed to analyze various design candidates. The analysis is for a two-cell thin-walled closed-section composite beam with anisotropic active plies embedded in it. Within the analytical model developed, the static and dynamic behavior of the active beam structure is analyzed through a two-step process: a linear two-dimensional analysis over the cross section, and a geometrically non-linear beam analysis along the span.

A verification process is conducted in each step of the analytical model development. The correlation effort with other existing analytical models and experimental results obtained from small-scaled active rotor blades are performed for cross-sectional stiffness constants, actuation (forcing vector) constants, and global blade structural

behavior. Studies are conducted to better understand the discrepancies between the Rehfield-based models and the present asymptotical one, as well as the design paradigm associated with the relation between torsional stiffness and twist actuation.

With the aid of the developed model, structural stiffness and inertia design of the prototype ATR blade are carried out. Blade dynamic characteristics, such as twist actuation and natural frequencies, are guaranteed within the requirements. For the static strength requirement, a comprehensive rotorcraft analysis code, CAMRAD II, is used to simulate critical forward flight conditions and the peak values of the vibratory loads within the blades are extracted.

Several candidates with different geometrical distribution of active material are proposed and tested in terms of satisfying the requirements. A final design is selected which also takes into account the cost effectiveness associated with AFC's. A prototype ATR blade was manufactured and bench test was also followed to assess the actuation performance and structural integrity.

Chapter 2

Active Blade Structural Analysis

2.1 Overview

An analytic formulation for a two-cell thin-walled composite beam with integral anisotropic piezoelectric actuators is derived to design and analyze an active twist helicopter rotor blade. It is an asymptotically correct formulation stemming from shell theory.

The present analysis extends previous work done for modeling generically passive blades [15, 18, 19]. The approach is based on the two-step solution of the original three-dimensional blade representation by means of an asymptotical approximation: a linear two-dimensional cross-sectional analysis and a nonlinear one-dimensional global analysis [15]. The resulting model is expected to correctly predict the behavior of helicopter blades, accounting for the presence of different materials (passive and active) and an approximation of the actual blade shape.

The cross-sectional analysis revises and extends the closed form solution of a thin-walled, multi-cell asymptotic formulation presented by Badir [20]. The variational-asymptotical method [21] is used to formulate the stiffness constants of a two-cell cross section with the active plies consisting of piezoelectric fibers. This cross-sectional analysis is a specialized case of the general framework established in [15]. It provides the expressions for the asymptotically-correct cross-sectional stiffness constants in closed form, facilitating design-trend studies. These stiffness constants will then be

used in a beam finite element discretization of the blade reference line. The exact intrinsic equations for the one-dimensional analysis of rotating beams considering small strains and finite rotations developed by Hodges [18] and implemented by Shang and Hodges [22] is extended to take into account the changes in the constitutive relation. Subject to external loads, active ply induced strains, and specific boundary conditions, the one-dimensional (beam) problem can be solved for displacements, rotations, and strains of the reference line. Finally, these results could be combined with information from the cross-sectional analysis in a set of recovering relations for stress/strain distribution at each ply of the blade. This structural representation serves the basis for an aeroelastic blade design model.

2.2 Cross-section Analysis

Stiffness constants for an anisotropic thin-walled two-cell beam is obtained from a variational-asymptotical formulation originally presented by Badir [20]. Herein, the original formulation is expanded to deal with the effects associated with the presence of active materials, the final expressions for the stiffness constants are corrected of misprints, and a validation study of such formulation (not presented in [20]) is presented in Chapter 3. In this section, the main steps of the cross-sectional analysis derivation is presented based on a linear beam formulation. Even though the one-dimensional (1-D) beam formulation that follows is intrinsically nonlinear, there is no loss of generality at this level to use a geometrically linear beam assumption.

Consider a slender thin-walled elastic cylindrical shell as shown in Fig. 2-1. It is assumed that

$$\frac{d}{L} \ll 1, \quad \frac{h}{d} \ll 1, \quad \frac{h}{R} \ll 1 \tag{2.1}$$

where L is length of the shell, h is thickness, $-\frac{h(s)}{2} < \xi < \frac{h(s)}{2}$, R is the radius of curvature of the middle surface, d is a characteristic cross-section dimension, and s is defined in Fig. 2-1.

The tangent vector $\mathbf{t}$, the normal vector $\mathbf{n}$ and the projection of the position vector

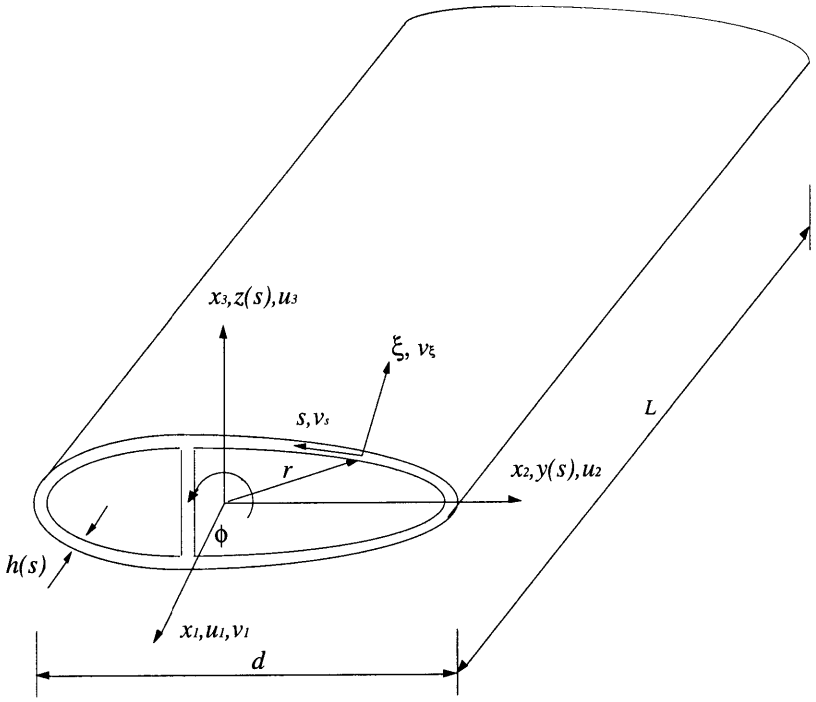


Figure 2-1: Two-cell thin-walled closed-section beam

$\mathbf{r}$ on $\mathbf{t}$ and $\mathbf{n}$ are expressed on the Cartesian and curvilinear coordinates as

$$\begin{aligned} \mathbf{t} &= \frac{d\mathbf{r}}{ds} = \frac{dy}{ds}\,\mathbf{b}_2 + \frac{dz}{ds}\,\mathbf{b}_3 \\ \mathbf{n} &= \mathbf{t} \times \mathbf{b}_1 = \frac{dz}{ds}\,\mathbf{b}_2 - \frac{dy}{ds}\,\mathbf{b}_3 \\ r_t &= \mathbf{r} \cdot \mathbf{t} = y\frac{dy}{ds} + z\frac{dz}{ds} \\ r_n &= \mathbf{r} \cdot \mathbf{n} = y\frac{dz}{ds} - z\frac{dy}{ds} \end{aligned} \tag{2.2}$$

and $\mathbf{b}_i$ are shown in Fig. 2-3.

The energy density of a three-dimensional (3-D) elastic body is a quadratic form of the strains

$$U = \frac{1}{2} E^{ijkl} \varepsilon_{ij}^{(m)} \varepsilon_{kl}^{(m)} \tag{2.3}$$

where $i, j, k, l = 1, 2, 3$; the material properties are expressed by the Hookean tensor E^{ijkl}. The mechanical strain $\varepsilon_{ij}^{(m)}$ is the difference between the total strain ε_{ij} and

the non-mechanical strain $\varepsilon_{ij}^{(nm)}$, i.e.,

$$\varepsilon_{ij}^{(m)} = \varepsilon_{ij} - \varepsilon_{ij}^{(nm)} \tag{2.4}$$

and the total strain can be written in terms of two-dimensional (2-D) strain measures as

$$\varepsilon_{ij} = \overline{\gamma}_{ij} + \xi\rho_{ij} \tag{2.5}$$

where $\overline{\gamma}_{ij}$ is in-plane strain components, and ρ_{ij} is the shell curvature.

Considering the non-mechanical strain coming only from piezoelectric actuation, the expression of non-mechanical strain $\varepsilon_{ij}^{(nm)}$ from a linear piezoelectric constitutive relation [23] is given as

$$\varepsilon_{ij} = s_{ijkl}^{E}\sigma_{kl} + d_{kij}E_k \tag{2.6}$$

where ε_{ij} is the total strain tensor, s_{ijkl}^{E} is the elastic compliance tensor at constant electric field, σ_{ij} is the stress tensor, d_{kij} is the piezoelectric electromechanical coupling tensor, E_k is the electric field vector.

The first term in the right-hand side of Eq. (2.6) represents mechanical strain $\varepsilon_{ij}^{(m)}$ and the second one represents the non-mechanical strain, which will be denoted by $\varepsilon_{ij}^{(a)}$ since it results from actuation only.

The 3-D strain energy is then minimized with respect to ε_{i3}, (the through-the-thickness stress components are considerably smaller than the remaining components) in order to obtain the formula corresponding to shell

$$\hat{U} = \min_{\varepsilon_{i3}} U = \frac{1}{2} D^{\alpha\beta\gamma\delta}\varepsilon_{\alpha\beta}^{(m)}\varepsilon_{\gamma\delta}^{(m)} \tag{2.7}$$

where $D^{\alpha\beta\gamma\delta}$ is the 2-D Hookean tensor (see, for example, [20]), and $\alpha,\ \beta,\ \gamma,\ \delta = 1, 2$.

From practical considerations, one may assume that only E_3 exists (the notation for the electric field follows conventional piezoelectric notation. Note, however, that in the case of AFC, the so-called E_3 runs along the piezo fibers). The 2-D strain

expression becomes

$$\begin{aligned} \varepsilon_{\alpha\beta}^{(m)} &= \varepsilon_{\alpha\beta} - \varepsilon_{\alpha\beta}^{(a)} \\ &= \overline{\gamma}_{\alpha\beta} + \xi\rho_{\alpha\beta} - d_{3\alpha\beta}E_3 \end{aligned} \tag{2.8}$$

Substitute Eq. (2.8) into Eq. (2.7) and integrate over the thickness ξ to get a shell energy Φ per unit middle surface area

$$\begin{aligned} 2\Phi &= \{< D^{\alpha\beta\gamma\delta} > \overline{\gamma}_{\alpha\beta} - 2 < D^{\alpha\beta\gamma\delta} d_{3\gamma\delta} E_3 >\}\overline{\gamma}_{\gamma\delta} \\ &+ 2\{< D^{\alpha\beta\gamma\delta}\xi > \overline{\gamma}_{\alpha\beta} - < D^{\alpha\beta\gamma\delta} d_{3\gamma\delta} E_3 \xi >\}\rho_{\gamma\delta} \\ &+ < D^{\alpha\beta\gamma\delta}\xi^2 > \rho_{\alpha\beta}\rho_{\gamma\delta} + \Psi(E_3) \end{aligned} \tag{2.9}$$

where

$$< (\bullet) >= \int_{-h(s)/2}^{+h(s)/2} (\bullet)\, d\xi \tag{2.10}$$

The function $\Psi(E_3)$ in Eq. (2.9) represents the quadratic terms in the electric field. Since the electric field is prescribed in the actuation problem, this term does not enter in the further derivation of the beam stiffnesses and actuation constants.

From the variational-asymptotical method [21], the shell energy functional after the first-order approximation reduces to

$$\begin{aligned} 2\Phi_1 &= \min_{\overline{\gamma}_{22}} 2\Phi \\ &= \{A\overline{\gamma}_{11} - 2A^{(a)}\}\overline{\gamma}_{11} + 2B\overline{\gamma}_{11}\overline{\gamma}_{12} + \{C\overline{\gamma}_{12} - 2C^{(a)}\}\overline{\gamma}_{12} - \Psi_2(E_3) \end{aligned} \tag{2.11}$$

The variables A, B, and C represent the axial, coupling, and shear stiffness, respectively, while the actuation contribution to the energy is represented by the new terms $A^{(a)}$, $C^{(a)}$, and $\Psi_2(E_3)$, *i.e.*

$$\begin{aligned} A &= < D^{1111} > - \frac{< D^{1122} >^2}{< D^{2222} >} \\ B &= 2\left(< D^{1112} > - \frac{< D^{1122} >< D^{1222} >}{< D^{2222} >}\right) \end{aligned}$$

$$
\begin{aligned}
C &= 4\left(< D^{1212} > - \frac{< D^{1222} >^2}{< D^{2222} >}\right) \\
A^{(a)} &= < D^{11\gamma\delta} d_{3\gamma\delta} E_3 > - \frac{< D^{1122} >}{< D^{2222} >} < D^{22\gamma\delta} d_{3\gamma\delta} E_3 > \\
C^{(a)} &= 2\left(< D^{12\gamma\delta} d_{3\gamma\delta} E_3 > - \frac{< D^{1222} >}{< D^{2222} >} < D^{22\gamma\delta} d_{3\gamma\delta} E_3 >\right)
\end{aligned}
\tag{2.12}
$$

The shear flow N_{12} is found to be constant and the hoop-stress resultant N_{22} vanishes

$$
\begin{aligned}
N_{11} &= \frac{\partial \Phi_1}{\partial(\overline{\gamma}_{11})} = (A(s)\overline{\gamma}_{11} + B(s)\overline{\gamma}_{12}) - A^{(a)}(s) \\
N_{12} &= \frac{\partial \Phi_1}{\partial(2\overline{\gamma}_{12})} = \frac{1}{2}(B(s)\overline{\gamma}_{11} + C(s)\overline{\gamma}_{12}) - \frac{1}{2}C^{(a)}(s) \\
&= \text{constant}
\end{aligned}
\tag{2.13}
$$

leading to a warping function w_1 associated with the first-order approximation as follows

$$
\frac{\partial w_1}{\partial s} = \frac{4}{C}\,(\text{constant}) - 2\,\frac{C}{B}u_1' + \frac{2}{C}\,C^{(a)} - u_2'\,\frac{dy}{ds} - u_3'\,\frac{dz}{ds} - \phi'\,r_n \tag{2.14}
$$

Using the single-value condition on the function w_1

$$
\oint_i \frac{\partial w_1}{\partial s}\,ds = 0 \tag{2.15}
$$

for the i-th closed cell (I for first cell and II for second cell) determines the expression of the "constant" in Eqs. (2.13) and (2.14).

The displacement field from the second-order approximation becomes

$$
\begin{aligned}
v_1 &= u_1(x) - y(s)\,u_2'(x) - z(s)\,u_3'(x) + \\
&\quad + G(s)\,\phi'(x) + g_1(s)\,u_1'(x) + g_2(s)\,u_2''(x) + g_3(s)\,u_3''(x) + \\
&\quad + v_1^{(a)}(s) \\
v_s &= u_2(x)\,\frac{dy}{ds} + u_3(x)\,\frac{dz}{ds} + \phi(x) r_n
\end{aligned}
\tag{2.16}
$$

$$v_\xi = u_2(x)\,\frac{dz}{ds} - u_3(x)\,\frac{dy}{ds} - \phi(x) r_t$$

where

$$v_1^{(a)}(s) = \begin{cases} \int_0^s \{2g_1^{(a)} - C^{(a)}(\tau)\} c(\tau) d\tau \\ \quad \text{with } s = 0 \rightarrow s_1 \text{ (left branch)} \\ \int_{s_1}^s \{2(g_1^{(a)} - g_2^{(a)}) - C^{(a)}(\tau)\} c(\tau) d\tau \\ \quad \text{with } s = s_1 \rightarrow s_2 \text{ (web)} \\ \int_{s_2}^s \{2g_2^{(a)} - C^{(a)}(\tau)\} c(\tau) d\tau \\ \quad \text{with } s = s_2 \rightarrow s_3 \text{ (right branch)} \end{cases}$$

$$\begin{aligned} g_1^{(a)} &= \frac{2\{(b_2+b_5) f_1^{(a)} + b_2 f_2^{(a)}\}}{(b_1+b_2)(b_2+b_5) - b_2^2} \\ g_2^{(a)} &= \frac{2\{(b_1+b_2) f_2^{(a)} + b_2 f_1^{(a)}\}}{(b_1+b_2)(b_2+b_5) - b_2^2} \\ f_1^{(a)} &= \oint_I c C^{(a)} ds \\ f_2^{(a)} &= \oint_{II} c C^{(a)} ds \end{aligned} \tag{2.17}$$

with b_i, c defined in the Appendix A, and each integration being evaluated along the corresponding branch of the two-cell cross section. The integration subscripts I and II denote anticlockwise integration over the left and right cell, respectively (Fig. 2-2).

The strain field associated with Eq. (2.16) is

$$\begin{aligned} \overline{\gamma}_{11} &= u_1'(x) - y(s)\, u_2''(x) - z(s)\, u_3''(x) \\ 2\overline{\gamma}_{12} &= (\frac{dG}{ds} + r_n)\, \phi' + \frac{dg_1}{ds}\, u_1' + \frac{dg_2}{ds}\, u_2'' + \frac{dg_3}{ds}\, u_3'' + \frac{dv_1^{(a)}}{ds} \\ \overline{\gamma}_{22} &= 0 \end{aligned} \tag{2.18}$$

The constitutive relations can be written in terms of stress resultants and kinematic variables by relating the traction F_1, torsional moment M_1, and bending mo-

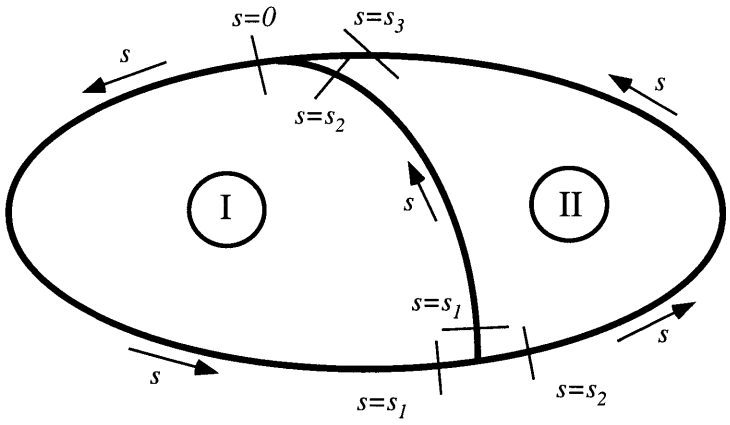


Figure 2-2: Branches for integration of a two-cell thin-walled cross section

ments M_2, M_3 to the shear flow and axial stress as follows:

$$\begin{aligned}
F_1 &= \frac{\partial \Phi_2}{\partial u_1'} = \oint \int \sigma_{11}\, d\xi ds = \oint N_{11}\, ds \\
M_1 &= \frac{\partial \Phi_2}{\partial \phi'} = \oint \int \sigma_{12}\, r_n(s)\, d\xi ds \\
&= \oint N_{12}\, r_n(s)\, ds \\
M_2 &= \frac{\partial \Phi_2}{\partial (-u_3'')} = \oint \int \sigma_{11}\, z(s)\, d\xi ds \\
&= \oint N_{11}\, z(s)\, ds \\
M_3 &= \frac{\partial \Phi_2}{\partial u_2''} = -\oint \int \sigma_{11}\, y(s)\, d\xi ds \\
&= -\oint N_{11}\, y(s)\, ds
\end{aligned} \tag{2.19}$$

Substituting Eq. (2.13) and Eq. (2.18) into Eq. (2.19) one gets

$$\begin{aligned}
F_1 &= \oint N_{11}\, ds \\
&= \oint \{A\overline{\gamma}_{11} + B\overline{\gamma}_{12} - A^{(a)}\}\, ds \\
&= \oint [A\{u_1' - yu_2'' - zu_3''\} + \frac{1}{2}\{(\frac{dG}{ds} + r_n)\, \phi' + \frac{dg_1}{ds}\, u_1' + \frac{dg_2}{ds}\, u_2'' \\
&\quad + \frac{dg_3}{ds}\, u_3'' + \frac{dv_1^{(a)}}{ds}\} - A^{(a)}]\, ds \\
&= K_{11}\, u_1' + K_{12}\, \phi' + K_{13}\, u_3'' + K_{14}\, u_2'' + \oint (\frac{B}{2}\, \frac{dv_1^{(a)}}{ds} - A^{(a)})\, ds
\end{aligned} \tag{2.20}$$

and similarly with the other three moment equations. The first four terms in the final part of the right-hand side of Eq. (2.20) correspond to the stiffness coefficients for an anisotropic two-cell beam. (Detailed expressions of K_{ij} and relevant parameters are in the Appendix A.) The last term (following those) results from piezoelectric actuation, and can be regarded as a forcing vector. The general form of the constitutive relation can be written as

$$\begin{Bmatrix} F_1 \\ M_1 \\ M_2 \\ M_3 \end{Bmatrix} = \begin{bmatrix} K_{11} & K_{12} & K_{13} & K_{14} \\ K_{12} & K_{22} & K_{23} & K_{24} \\ K_{13} & K_{23} & K_{33} & K_{34} \\ K_{14} & K_{24} & K_{34} & K_{44} \end{bmatrix} \begin{Bmatrix} u_1' \\ \phi' \\ -u_3'' \\ u_2'' \end{Bmatrix} - \begin{Bmatrix} F_1^{(a)} \\ M_1^{(a)} \\ M_2^{(a)} \\ M_3^{(a)} \end{Bmatrix} \tag{2.21}$$

Explicit expressions of piezoelectric actuation contributing to the constitutive relation are given by

$$\begin{aligned} F_1^{(a)} &= \oint \{A^{(a)} - \frac{B}{C} C^{(a)}\} \, ds + 2g_1^{(a)} \oint_I \frac{B}{C} \, ds + 2g_2^{(a)} \oint_{II} \frac{B}{C} \, ds \\ M_1^{(a)} &= -2g_1^{(a)} \, A_{eI} - 2g_2^{(a)} \, A_{eII} \\ M_2^{(a)} &= -\oint \{A^{(a)} - \frac{B}{C} C^{(a)}\} z \, ds - 2g_1^{(a)} \oint_I \frac{B}{C} z \, ds - 2g_2^{(a)} \oint_{II} \frac{B}{C} z \, ds \\ M_3^{(a)} &= \oint \{A^{(a)} - \frac{B}{C} C^{(a)}\} y \, ds + 2g_1^{(a)} \oint_I \frac{B}{C} y \, ds + 2g_2^{(a)} \oint_{II} \frac{B}{C} y \, ds \end{aligned} \tag{2.22}$$

where integral without any subscripts $\oint$ denotes over-all-section evaluation, which is a summation of evaluations over $s = 0 \rightarrow s_1$, $s = s_1 \rightarrow s_2$ and $s = s_2 \rightarrow s_3$.

2.3 1-D Beam Analysis

A nonlinear one-dimensional global analysis considering small strains and finite rotations is presented here as a direct expansion of the mixed variational intrinsic formulation of moving beams originally presented by Hodges [18], and implemented in [22]. The notation used in this section is based on matrix notation and is consistent with the original work of [18] and [22]. Some steps are repeated here to help clarifying the modifications in this extended formulation.

2.3.1 Extended active beam equations

As shown in Fig. 2-3, a global frame denoted a is rotating with the rotor, with its axes labeled as a_1, a_2 and a_3. The undeformed reference frame of the blade is denoted b, with its axes labeled as b_1, b_2 and b_3, and the deformed reference frame denoted B, with its axes labeled as B_1, B_2 and B_3, though not shown in the figure. Any arbitrary vector Z represented by its components in one of the basis may be converted to another basis like

$$Z_b = C^{ba} Z_a, \quad Z_B = C^{Ba} Z_a \tag{2.23}$$

where C^{ba} is the transformation matrix from a to b, and C^{Ba} is that from a to B. There are several ways to express the transformation matrices. C^{ba} can be expressed in terms of direction cosines from the initial geometry of the rotor blade, while C^{Ba} contains the unknown rotation variables.

As described in details in [18], the variational formulation is derived from Hamilton's principle which can be written as

$$\int_{t_1}^{t_2} \int_0^l [\delta(K - U) + \overline{\delta W}] \, dx_1 dt = \overline{\delta \mathsf{A}} \tag{2.24}$$

where t_1 and t_2 are arbitrarily fixed times, K and U are the kinetic and potential energy densities per unit span, respectively. $\overline{\delta \mathsf{A}}$ is the virtual action at the ends of the beam and at the ends of the time interval, and $\overline{\delta W}$ is the virtual work of applied loads per unit span.

Taking the variation of the kinetic and potential energy terms with respect to V_B and Ω_B, the linear and angular velocity column vectors, and with respect to γ and κ, the generalized strain column vectors,

$$\begin{aligned} F_B &= \left(\frac{\partial U}{\partial \gamma}\right)^T, \quad M_B = \left(\frac{\partial U}{\partial \kappa}\right)^T \\ P_B &= \left(\frac{\partial K}{\partial V_B}\right)^T, \quad H_B = \left(\frac{\partial K}{\partial \Omega_B}\right)^T \end{aligned} \tag{2.25}$$

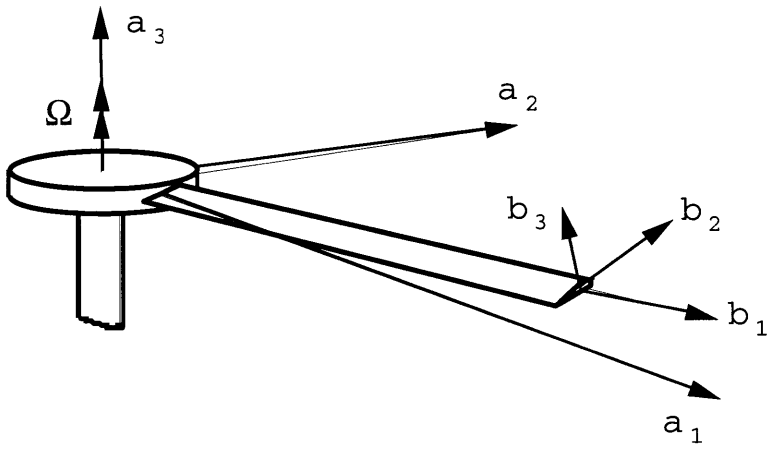


Figure 2-3: Blade frames

where F_B and M_B are internal force and moment column vectors, and P_B and H_B are linear and angular momentum column vectors, respectively.

The geometrically exact kinematical relations in the a frame are given by

$$\begin{aligned} \gamma^* &= C^{Ba}\left(C^{ab}e_1 + u_a'\right) - e_1 \\ \kappa^* &= C^{ba}\left(\frac{\Delta - \frac{\tilde{\theta}}{2}}{1 + \frac{\theta^T\theta}{4}}\right)\theta' \\ V_B^* &= C^{Ba}\left(v_a + \dot{u}_a + \tilde{\omega}_a u_a\right) \\ \Omega_B^* &= C^{ba}\left(\frac{\Delta - \frac{\tilde{\theta}}{2}}{1 + \frac{\theta^T\theta}{4}}\right)\dot{\theta} + C^{Ba}\omega_a \end{aligned} \tag{2.26}$$

where u_a is the displacement vector measured in the a frame, θ is the rotation vector expressed in terms of Rodrigues parameters, e_1 is the unit vector $[1,\ 0,\ 0]^T$, Δ is the 3×3 identity matrix, v_a and w_a are the initial velocity and initial angular velocity of a generic point on the a frame. $\tilde{(\ )}$ operator applied to a column vector is defined as:

$$\tilde{Z} = \begin{bmatrix} 0 & -Z_3 & Z_2 \\ Z_3 & 0 & -Z_1 \\ -Z_2 & Z_1 & 0 \end{bmatrix} \tag{2.27}$$

To form a mixed formulation, Lagrange's multipliers are used to enforce V_B, Ω_B,

γ and κ to satisfy the geometric equations in Eq. (2.26).

Manipulating the equations according to [22], one can obtain the a frame version of the variational formulation based on exact intrinsic equations for dynamics of moving beams as

$$\int_{t_1}^{t_2} \delta\Pi_a \, dt = 0 \tag{2.28}$$

where

$$\begin{aligned}
\delta\Pi_a \;=\; & \int_0^l \{\delta u_a'^T C^T C^{ab} F_B + \delta u_a^T [(C^T C^{ab} P_B)^\bullet + \tilde{\omega}_a C^T C^{ab} P_B] \\
& + \overline{\delta\psi}_a'^T C^T C^{ab} M_B - \overline{\delta\psi}_a^T C^T C^{ab} (\widetilde{e_1} + \tilde{\gamma}) F_B \\
& + \overline{\delta\psi}_a^T [(C^T C^{ab} H_B)^\bullet + \widetilde{\omega}_a C^T C^{ab} H_B + C^T C^{ab} \widetilde{V}_B P_B] \\
& - \overline{\delta F}_a^T [C^T C^{ab} (e_1 + \gamma) - C^{ab} e_1] - \overline{\delta F}_a'^T u_a \\
& - \overline{\delta M}_a^T (\Delta + \frac{\tilde{\theta}}{2} + \frac{\theta\theta^T}{4}) C^{ab} \kappa - \overline{\delta M}_a' \theta \\
& + \overline{\delta P}_a^T (C^T C^{ab} V_B - v_a - \widetilde{\omega}_a u_a) - \overline{\delta P}_a^T \dot{u}_a \\
& + \overline{\delta H}_a^T (\Delta - \frac{\tilde{\theta}}{2} + \frac{\theta\theta^T}{2}) (C^T C^{ab} \Omega_B - \omega_a) \\
& - \overline{\delta H}_a^T \dot{\theta} - \delta u_a^T f_a - \overline{\delta\psi}_a^T m_a \} dx_1 \\
& - \left| (\delta u_a^T \hat{F}_a + \overline{\delta\psi}_a^T \hat{M}_a - \overline{\delta F}_a^T \hat{u}_a - \overline{\delta M}_a^T \hat{\theta} \right|_0^l
\end{aligned} \tag{2.29}$$

and the rotation matrix C is the product $C^{ab}C^{Ba}$ and express it in terms of θ as

$$C = \frac{(1 - \frac{\theta^T\theta}{4})\Delta - \tilde{\theta} + \frac{\theta\theta^T}{2}}{1 + \frac{\theta^T\theta}{4}} \tag{2.30}$$

In Eq. (2.29), f_a and m_a are the external forces and moment vectors respectively, which result from aerodynamics loads. The $\hat{(\,)}$ terms are boundary values of the corresponding quantities. The generalized strain and force measures, and velocity and momentum measures are related through the constitutive relations in the following

form:

$$\begin{Bmatrix} F_B \\ M_B \end{Bmatrix} = [K] \begin{Bmatrix} \gamma \\ \kappa \end{Bmatrix} - \begin{Bmatrix} F_B^{(a)} \\ M_B^{(a)} \end{Bmatrix} \tag{2.31}$$

$$\begin{Bmatrix} P_B \\ H_B \end{Bmatrix} = \begin{bmatrix} m\Delta & 0 \\ 0 & I \end{bmatrix} \begin{Bmatrix} V_B \\ \Omega_B \end{Bmatrix}$$

and these expressions are solved for γ, κ, V_B, and Ω_B as function of the other measures and constants and used in Eq. (2.29). The stiffness $[K]$ is in general a 6×6 matrix, function of material distribution and cross sectional geometry. As described in [24], the 6×6 stiffness matrix can be reduced to a 4×4 one. The latter is used in this thesis, where the stiffness matrix and column vector for the piezoelectric actuation are described in Eq. (2.21).

Adopting a finite element discretization by dividing the blade into N elements, Eq. (2.28) is written as

$$\int_{t_1}^{t_2} \sum_i \delta\Pi_i \, dt = 0 \tag{2.32}$$

where index i indicates the i-th element with length Δl_i, $\delta\Pi_i$ is the corresponding spatial integration of the function in Eq. (2.29) over the i-th element. Due to the formulation's weakest form, the simplest shape functions can be used. Therefore, the following transformation and interpolation are applied within each element [22]:

$$x = x_i + \xi \Delta l_i, \; dx = \Delta l_i \, d\xi, \; (\,)' = \frac{1}{\Delta l_i} \frac{d}{d\xi}(\,) \tag{2.33}$$

$$\begin{aligned}
\delta u_a &= \delta u_i(1-\xi) + \delta u_{i+1}\xi, & u_a &= u_i \\
\overline{\delta\psi}_a &= \overline{\delta\psi}_i(1-\xi) + \overline{\delta\psi}_{i+1}\xi, & \theta &= \theta_i \\
\overline{\delta F}_a &= \overline{\delta F}_i(1-\xi) + \overline{\delta F}_{i+1}\xi, & F_B &= F_i \\
\overline{\delta M}_a &= \overline{\delta M}_i(1-\xi) + \overline{\delta M}_{i+1}\xi, & M_B &= M_i \\
\overline{\delta P}_a &= \overline{\delta P}_i, & P_B &= P_i \\
\overline{\delta H}_a &= \overline{\delta H}_i, & H_B &= H_i
\end{aligned}$$

where u_i, θ_i, F_i, M_i, P_i and H_i are constant vectors at each node i, and all δ quantities are arbitrary. ξ varies from 0 to 1.

With these shape functions, the spatial integration in Eq. (2.32) can be performed explicitly to give

$$\begin{aligned}\sum_{i=1}^{N} \quad & \{\delta u_i^T f_{u_i} + \overline{\delta\psi}_i^T f_{\psi_i} + \overline{\delta F}_i^T f_{F_i} + \overline{\delta M}_i^T f_{M_i} + \overline{\delta P}_i^T f_{P_i} + \overline{\delta H}_i^T f_{H_i} \\ & + \delta u_{i+1}^T f_{u_{i+1}} + \overline{\delta\psi}_{i+1}^T f_{\psi_{i+1}} + \overline{\delta F}_{i+1}^T f_{F_{i+1}} + \overline{\delta M}_{i+1}^T f_{M_{i+1}}\} \\ = \quad & \delta u_{N+1}^T \hat{F}_{N+1} + \overline{\delta\psi}_{N+1}^T \hat{M}_{N+1} - \overline{\delta F}_{N+1}^T \hat{u}_{N+1} - \overline{\delta M}_{N+1}^T \hat{\theta}_{N+1} \\ & - \delta u_1^T \ \hat{F}_1 - \overline{\delta\psi}_1^T \hat{M}_1 + \overline{\delta F}_1^T \ \hat{u}_1 - \overline{\delta M}_1^T \ \hat{\theta}_1\end{aligned} \tag{2.34}$$

where the f_{u_i}, f_{ψ_i} ,..., $f_{M_{i+1}}$ are the element functions explicitly integrated from the formulation.

In each element function, γ and κ should be replaced with a form that is a function of F_B and M_B using the inverse form of Eq. (2.31), along with the piezoelectric forcing vector $F_B^{(a)}$ and $M_B^{(a)}$. So does V_B and Ω_B with a form function of P_B and H_B. Detailed expressions of the element functions in Eq. (2.34) are shown in the Appendix B with the changes due to the presence of actuators embedded in the structure.

Since each δ-quantity is arbitrary, Eq. (2.34) yields a group of equations that can be written in operator form as

$$G(X, \dot{X}, \bar{F}) = 0 \tag{2.35}$$

where X is the column matrix of unknowns and G is a column matrix of functions. $\bar{F}$ is a column matrix containing the external nodal loads. Both X and G are of dimension $18N + 12$, in the case of a cantilever beam.

The solutions of interest for Eq. (2.35) can be expressed as a combination of two components as follows [22]:

$$X = \bar{X} + \check{X}(t) \tag{2.36}$$

where $\bar{X}$ is the steady component, which is independent of time, and $\check{X}(t)$ is the transient components of the solution, or, the perturbed motion, which contains the time dependency.

In the steady state, $\check{X}(t) = 0$, and the equation becomes:

$$G(\bar{X},\ 0, \bar{F}) = 0 \tag{2.37}$$

or simply:

$$G(\bar{X}, \bar{F}) = 0 \tag{2.38}$$

Following the solution procedure for the nonlinear equation, Eq. (2.38), adopted in [22], the use of the Newton-Raphson method requires gradient information. The Jacobian matrix can be derived explicitly by differentiation:

$$[J] = \left[\frac{\partial G}{\partial \bar{X}}\right] \tag{2.39}$$

leading to a very sparse matrix, that enables an efficient calculation of the solution. Notice that the presence of actuation on the blade changes the original terms of the Jacobian in a similar manner it does in Eq. (2.34).

The solution from the 1-D beam analysis provides blade displacement and generalized stress fields due to external loading and piezoelectric actuation, which are of interest in the analysis of static and dynamic deformations, and aeroelastic stability.

2.3.2 Inertial properties

In order to calculate the dynamic characteristics of a blade and inertial loads exerted by its mass distribution, the 6×6 inertial matrix is generally required as in Eq. (2.31). Notice that all the off-diagonal elements in the inertial matrix will vanish if the center of gravity is used as the cross-section reference point. Therefore, for generality, consider the evaluation of the 6×6 inertial matrix with respect to an arbitrary point other than the center of gravity. According to the general derivation of the geometrically exact one-dimensional intrinsic equations of [18], the linear momentum

P_B and the angular momentum H_B in the cross section can be represented as follows:

$$\begin{aligned} P_B &= m(V_B - \tilde{\xi}_B\, \Omega_B) \\ H_B &= i_B\, \Omega_B + m\, \tilde{\xi}_B\, V_B \end{aligned} \tag{2.40}$$

One can rewrite Eq. (2.40) in a matrix form, which is the desired 6×6 inertial matrix

$$\left\{ \begin{array}{c} P_B \\ H_B \end{array} \right\} = \left[\begin{array}{cc} m & -m\, \tilde{\xi}_B \\ m\, \tilde{\xi}_B & i_B \end{array} \right] \left\{ \begin{array}{c} V_B \\ \Omega_B \end{array} \right\} \tag{2.41}$$

where,

$$\begin{aligned} m &= \int\int_{A(x_1)} \rho\, \Delta\, \sqrt{g}\, dx_2\, dx_3 \\ m\, \tilde{\xi}_B &= \int\int_{A(x_1)} \rho\, \tilde{\xi}_B\, \sqrt{g}\, dx_2\, dx_3 \\ i_B &= \int\int_{A(x_1)} \rho\, (\xi_B^T\, \xi_B\, \Delta - \xi_B \xi_B^T)\, \sqrt{g}\, dx_2\, dx_3 \end{aligned} \tag{2.42}$$

Again,

$$\begin{aligned} \xi_B &= \left\{ \begin{array}{ccc} 0 & x_2 & x_3 \end{array} \right\}^T \\ \sqrt{g} &= 1 - x_2\, k_{b_3} + x_3\, k_{b_2} \end{aligned}$$

where, k_{b_2}, k_{b_3} are two components of the initial curvature of the beam; Δ and $\tilde{(\,)}$ have the same definition as used in Section 2.3. Explicitly, Eq. (2.42) can be written as:

$$m = \int\int_{A(x_1)} \left[\begin{array}{ccc} \rho & 0 & 0 \\ 0 & \rho & 0 \\ 0 & 0 & \rho \end{array} \right] dx_2\, dx_3$$

$$m\,\tilde{\tilde{\xi}}_B = \int\int_{A(x_1)} \begin{bmatrix} 0 & -\rho\,x_3 & \rho\,x_2 \\ \rho\,x_3 & 0 & 0 \\ -\rho\,x_2 & 0 & 0 \end{bmatrix} dx_2\,dx_3 \tag{2.43}$$

$$i_B = \int\int_{A(x_1)} \begin{bmatrix} \rho\,(x_2^2+x_3^2) & 0 & 0 \\ 0 & \rho\,x_3^2 & -\rho\,x_2\,x_3 \\ 0 & -\rho\,x_2\,x_3 & \rho\,x_2^2 \end{bmatrix} dx_2\,dx_3$$

2.4 Three-dimensional Stress Recovery Formulation

The three-dimensional stress state in the beam under any specified load can be recovered from the formulation established above. This will be used to examine the structural integrity of the designed beam structure, where the stress state existing in each lay-up ply should be estimated and compared with the strength of its material.

Using the inverse form of the one-dimensional global beam constitutive relation, Eq. (2.44), the strain and curvature measures of the beam reference line are obtained at each blade station as a function of the internal forces and moments as:

$$\begin{Bmatrix} \gamma \\ \kappa \end{Bmatrix} = [K]^{-1} \begin{Bmatrix} F_B \\ M_B \end{Bmatrix} \tag{2.44}$$

The strains in the shell coordinate system, i.e., $\bar{\gamma}_{11}$, $\bar{\gamma}_{12}$, are obtained from γ and κ using the strain field relation, Eq. (2.18), which corresponds to the strains in the laminate coordinate, denoted as $\bar{\epsilon}^{(k)}$.

According to the classical laminated plate theory [25], $\bar{\epsilon}^{(k)}$ can be converted to the strains in the k-th ply coordinate, $\epsilon^{(k)}$, as follows

$$\bar{\epsilon}^{(k)} = T_\epsilon^{(k)}\,\epsilon^{(k)} \tag{2.45}$$

where $T_{\epsilon}^{(k)}$ is a transformation matrix between the material and the laminate coordinates, and it is a function of the orientation angle of the k-th ply. Then, $\epsilon^{(k)}$ can be converted to the stress within the ply, $\sigma^{(k)}$, using the stiffness matrix $Q^{(k)}$ based on the plane-stress condition:

$$\sigma^{(k)} = Q^{(k)} \epsilon^{(k)} \tag{2.46}$$

By adopting either maximum stress criteria or maximum strain criteria, the first ply failure may be verified.

Chapter 3

Validation of the Proposed Active Structural Model

3.1 Overview

In order to validate the formulation, a verification process is carried out in each step of the development. The numerical results are divided in cross-sectional stiffness and actuation (forcing vector) constants, and global blade structural behavior.

A passive two-cell box beam is considered at first to compare the stiffness constants from the present formulation with the other existing asymptotically-correct model. Verification of actuation constants is performed using two different experimental active blades, and through which the blade structural behavior can also be verified. One is a single-cell airfoil-shaped beam with one layer of AFC at the top and bottom surfaces [11]. The other is a 1/6th Mach-scaled CH-47D helicopter rotor blade modified with AFC plies insertion at the front spar skins [6]. However, due to limitation on other existing active beam models to single-cell cross sections (for example, [11]), numerical results considering only the front D-spar are available for direct comparison.

3.2 Box-Beam Case

Regarding the cross-sectional analysis, the stiffness coefficients and forcing vector in the constitutive relation, Eq. (2.21), are verified by comparing the result with other formulations.

The formulation for the passive stiffness coefficients for an anisotropic two-cell beam used here was first derived in [20], but it was not validated there. So, after re-deriving and making corrections to the stiffness constant expressions, numerical tests were conducted for two-cell beams without piezoelectric actuators. Results from the present formulation were then compared with the ones generated using VABS (Variational-Asymptotical Beam Section Analysis) [15], a general asymptotically-correct finite-element-based cross-sectional analysis intended for modeling arbitrary geometry (including multiple-cell).

Table 3.1: Properties of AS4/3506-1 Graphite/epoxy – "L" direction is along the fibers and "N" is normal to laminate

$E_{LL} = 142$ GPa	$E_{NN} = E_{TT} = 9.8$ GPa
$G_{LT} = G_{LN} = 6.0$ GPa	$G_{TN} = 4.80$ GPa
$\nu_{LT} = \nu_{LN} = 0.3$	$\nu_{TN} = 0.42$
Thickness $= 0.127$ mm	

As an example, consider the box beam configuration represented in Fig. 3-1, the material properties of which are given in Table 3.1. VABS was run with the cross section being discretized with 364 six-node isoparametric elements for a total of 909 nodes.

A comparison of the stiffness coefficients from both theories is provided in Table 3.2. The present formulation is in good agreement with VABS, with the errors well within the range expected for this kind of thin-walled cross-sectional formulation [15]. Results for other cross sections could be shown, but the conclusion are similar to this one due to the nature of the asymptotical formulation. The limiting assumption is that the thickness of the wall compared to the cross-sectional characteristic dimension must be small compared to unit.

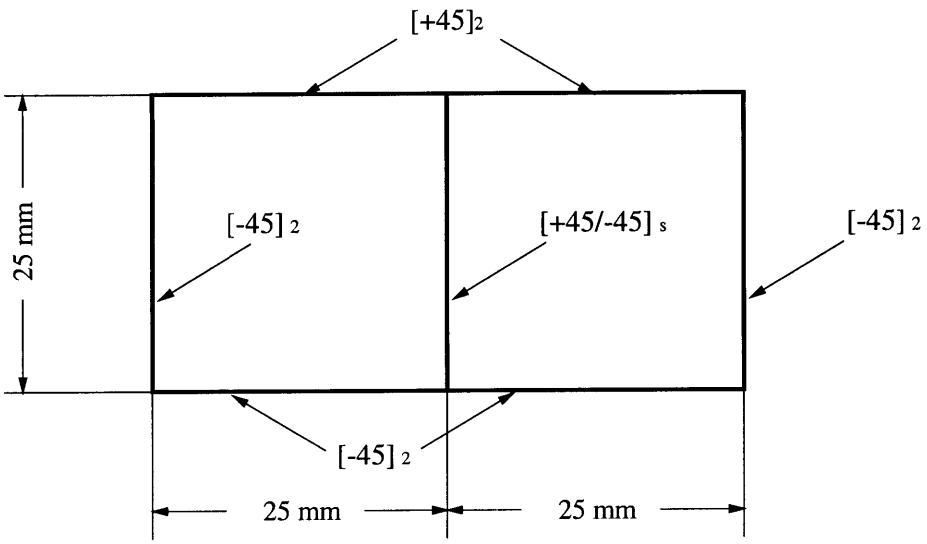


Figure 3-1: Two-cell thin-walled box beam definition

Table 3.2: Non-zero stiffness results (N, N m, N m^2) for two-cell box beam (1 extension; 2 torsion; 3, 4 bending)

K_{ij}	**Present**	**VABS**	% Difference
K_{11}	$8.472\ 10^5$	$8.477\ 10^5$	-0.1
K_{12}	$-1.828\ 10^3$	$-1.794\ 10^3$	$+1.9$
K_{13}	$6.395\ 10^2$	$6.337\ 10^2$	$+0.9$
K_{22}	$1.299\ 10^2$	$1.278\ 10^2$	$+1.6$
K_{23}	$4.547\ 10^1$	$4.461\ 10^1$	-1.9
K_{33}	$9.631\ 10^1$	$9.567\ 10^1$	$+0.7$
K_{44}	$2.075\ 10^2$	$2.070\ 10^2$	$+0.2$

3.3 Single-Cell Active Blade Results

3.3.1 Cross-section results

For a preliminary assessment of the piezoelectric actuation change in the constitutive relation, results from the present formulation is compared against [11]. This work incorporates active material capabilities into Rehfield's formulation [14] to model single-cell composite beams with distributed, planar, anisotropic actuator.

The test case chosen here is an airfoil-shaped cross section with piezoelectric actuators attached at the upper and lower surfaces. This is one of the model beams fabricated and tested by duPlessis and Hagood [11] using AFC. In each AFC pack, the

Table 3.3: Material properties used in the single-cell active blade (Q_{ij} are the laminate reduced stiffness of the actuator pack)

E-Glass (Style 120 Fabric)	E_L	14.8 GPa
	E_T	13.6 GPa
	ν_{LT}	0.19
	t_{ply}	203.2 νm
	G_{LT}	1.9 GPa
AFC (PZT-5H)	Q_{11}	32.8 GPa
	Q_{12}	6.26 GPa
	Q_{22}	17.3 GPa
	Q_{66}	5.5 GPa
	d_{31}	381 pm/V
	d_{32}	-160 pm/V
	t_{ply}	168.9 μm

piezoelectric (PZT-5H) fibers are aligned in +45° in order to maximize the twist actuation. The cross-sectional geometry is shown in Fig. 3-2, and the material properties are presented in Table 3.3.

Since the formulation presented in [11] is based on a 7 × 7 stiffness matrix that besides the classical degrees of freedom also includes (two) transverse shear and (one) restrained warping, a condensation to a 4 × 4 matrix is necessary for comparison. This is done through the minimization of the strain energy with respect to the extra degrees of freedom as described, for example, in [24]. Also, the 7 × 1 forcing vector can be reduced to 4 × 1 representation through a similar procedure. Only then, a comparison of the results can be made. The predicted stiffness coefficients and forcing vector induced by an electric field of -1800 V / 1.114×10^{-3} mm are presented in Table 3.4. The tension axis was used for the beam reference line due to restrictions on the formulation of [11] (this comes from the original assumption on the original Rehfield model). This, however, is not a restriction for the present formulation.

From Table 3.4, the results for the stiffness constants show very good agreement between the two formulations. In fact, this level of agreement, mainly on the torsional stiffness, is a coincidence for this case, due to the layup used. In general, the torsional stiffness will be different since Rehfield's torsional warping only coincides with the asymptotically correct one for laminates with specific characteristics [26]. For the

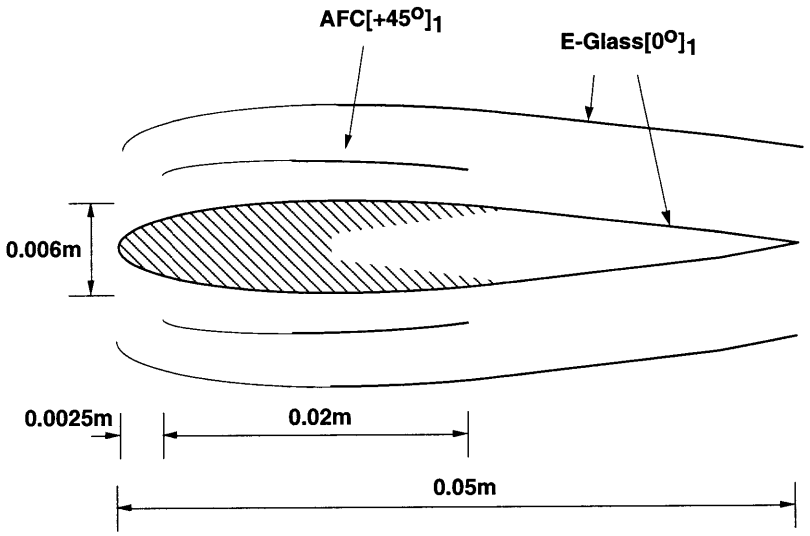


Figure 3-2: Single-cell active blade cross section (NACA 0012)

Table 3.4: Non-zero stiffness (N, N m, N m^2) and forcing vector (N, N m) results for airfoil-shaped cross section – (K_{ij}: 1 extension; 2 torsion; 3, 4 bending)

K_{ij}	**Present**	**Ref. [11]**	% Diff.
K_{11}	$7.552\ 10^5$	$7.585\ 10^5$	-0.4
K_{12}	$4.541\ 10^1$	$4.574\ 10^1$	-0.7
K_{22}	1.848	1.848	0.0
K_{33}	3.996	4.021	-0.6
K_{44}	$1.487\ 10^2$	$1.490\ 10^2$	-0.2
$F_1^{(a)}$	$-3.255\ 10^1$	$-4.117\ 10^1$	-20.9
$M_1^{(a)}$	$-1.170\ 10^{-1}$	$-1.179\ 10^{-1}$	-0.8
$M_3^{(a)}$	$-2.557\ 10^{-3}$	$-3.192\ 10^{-3}$	-19.8

forcing vector terms, $M_1^{(a)}$ is in very good agreement with condensed results of [11]. The agreement was less than satisfactory for the induced axial force $F_1^{(a)}$ and lead-lag bending $M_3^{(a)}$, even though they are of secondary importance for direct shear actuation for this blade. In general, however, as in the case of the torsional stiffness constant, similar conclusion can be reached for the components of the forcing vector, since they are function of the warping field present in the formulation [27]. This reinforces the importance of a consistent asymptotical formulation when dealing with cross-sectional characterization.

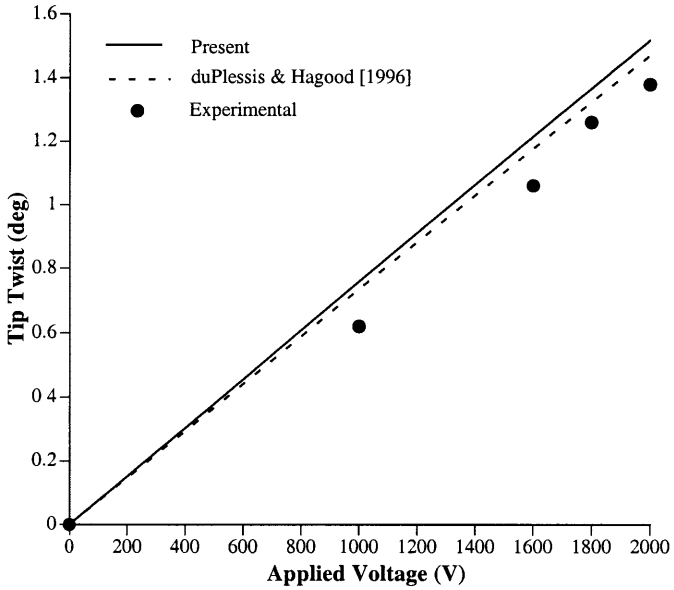


Figure 3-3: Single-cell active blade tip twist

3.3.2 Beam results

The impact of eventual discrepancies at the cross-sectional level can be better evaluated when carried on to the next level, *i.e.*, the 1-D analysis, and compared to experimental results.

Considering the present formulation and the previous model beam of [11], cross-sectional results can be used in the 1-D beam analysis that considers the effects of embedded actuation. Global (1-D) twist results are presented in Figs. 3-3 and 3-4. Fig. 3-3 shows the variation of the blade tip twist as function of applied voltage in the AFC. As one can see, there are no significant differences between the present theory and the one of [11]. Both predictions are higher than the experimental measurements and this may be partially attributed to the fact that the foam core present in the blade (originally used to facilitate blade manufacturing) has not been modeled by either formulations. If one looks at the extension deformation due to $F_1^{(a)}$, that would show much higher discrepancies than the ones found in Fig. 3-3. However, the absolute values of deformation are small and not of practical concern for this example. This may change if one uses extension-twist coupling effects for twist actuation, or even for purely bending actuation.

In order to quantify the warping restrained and main transverse shear effects

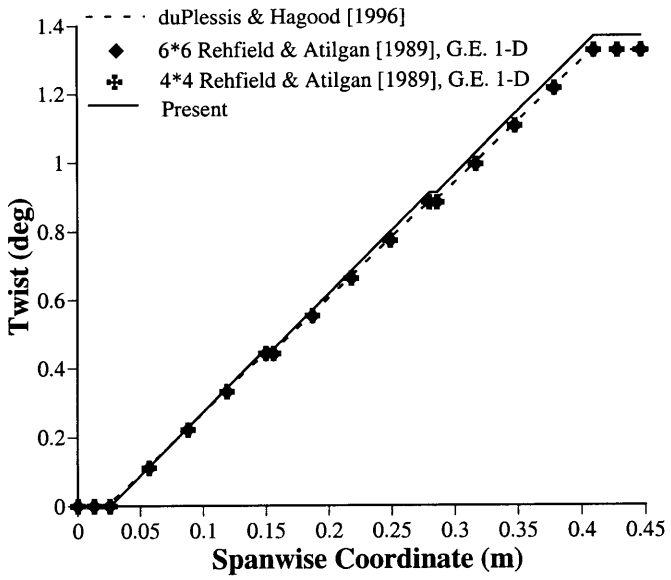


Figure 3-4: Single-cell active blade twist distribution

at the cross-sectional modeling for this single-cell active blade, a numerical study was performed among the different cross-sectional analysis. Results are presented in Fig. 3-4 for the twist distribution along the spanwise coordinate for a constant applied voltage of 1800 V. The results labeled "duPlessis & Hagood [1996]" are from [11], and they include effects of restrained warping and main transverse shear stiffness, presenting a 7×7 stiffness matrix (although not asymptotically correct for generic layups). The 1-D analysis is linear. The results labeled "6×6 Rehfield & Atilgan [1989], G.E. 1-D" refers to stiffness constants based on the previous formulation but without the restrained warping row and column, reducing the stiffness matrix from the 7×7 to a 6×6 matrix, and the present geometrically-exact 1-D formulation (this is not an issue at this point, since the twist is small enough for a linear approximation). Next, the "4×4 Rehfield & Atilgan [1989], G.E. 1-D" has the condensed 4×4 stiffness matrix from the previous 6×6 formulation, then eliminating the main transverse shear terms. Notice that the non-classical coupling effects due to transverse shear have not been neglected. All the above are plotted in Fig. 3-4 along with the present formulation. As one would expect, the restrained warping effects are minimum for a closed-cell beam. For this beam, also the main transverse shear effects are not significant, and a 4×4 stiffness formulation is sufficient to account for all the major

effects for quasi-static behavior.

3.4 Two-Cell Active Blade Results

A 1/6th Mach-scaled two-cell CH-47D helicopter rotor blade section with AFC plies embedded within the front D-spar [6] is used to validate actuation constants and global blade structural behavior of a multi-cell beam of the present formulation. Both analytical prediction using the modified Rehfield model [11] and experimental data from the prototype blade are compared with the results from the present formulation. The cross-sectional and spanwise design of CH-47D active blade are shown in Fig. 3-5.

In a preliminary stage, a test specimen which contains only the front D-spar section is fabricated (see Fig. 3-6), and twist actuation measurement is obtained [5].

The comparison with the present formulation is summarized in Table 3.5 where the cross-sectional analysis results considering only single-cell to model the front D-spar is shown. It is noticed that the components related with the torsional deformation, such as torsional stiffness K_{22} and twisting actuation moment $M_1^{(a)}$, are still in good agreement with each other. This seems to be another case in which both analytical models give coinciding results for those components. Detailed discussion on such discrepancies of the results from both analytical models is provided in Chapter 4 pursuing both analytical approach and numerical calculation on the different ply lay-up configurations.

The result considering the whole elements in the cross section, i.e., front spar and fairing, is provided in Table 3.6. The result denoted by "Ref. [11] + ad hoc corrections" is obtained by combining the analysis result considering the front D-spar and some appropriate stiffness constants corresponding to the remaining components like skin plies of the fairing, core material, and tungsten weights that are inserted at the nose section. These corrections were introduced by Boeing Helicopter engineers based on their experience, and it is reported in [28]. The correlation is not as good as in the previous case, and the analysis capability of the present formulation limited to the skin plies is one of the factors which makes the discrepancy.

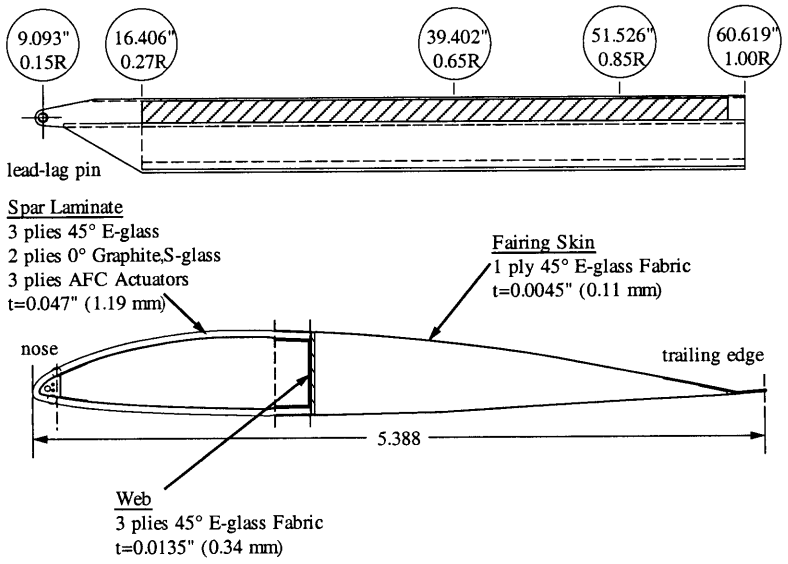


Figure 3-5: Schematic diagram of the complete CH-47D active blade section [28]

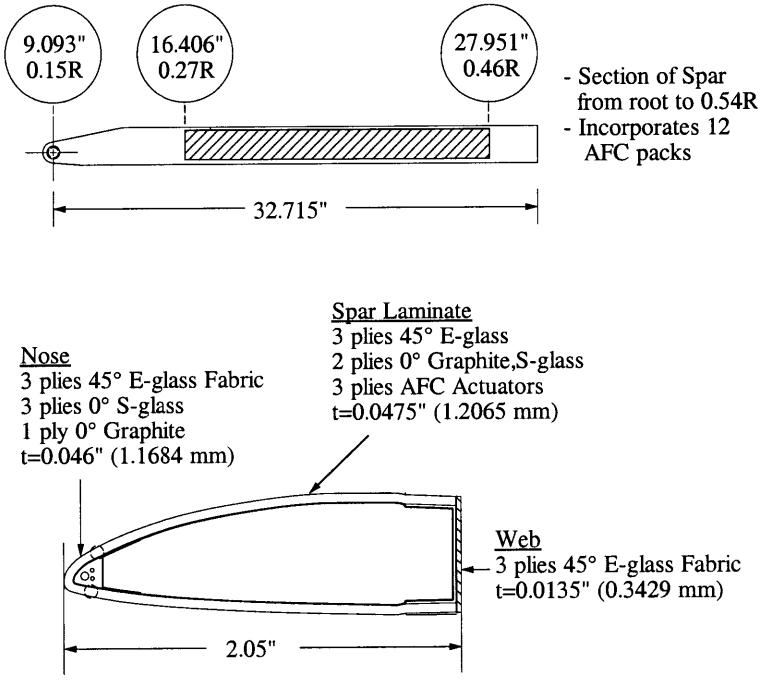


Figure 3-6: Schematic diagram of the CH-47D spar [28]

Table 3.5: Non-zero stiffness (N, N m, N m^2) and forcing vector (N, N m) results for CH-47D D-spar only – (K_{ij}: 1 extension; 2 torsion; 3, 4 bending)

	Present	**Ref. [11]**	% Difference
K_{11}	$4.662\ 10^6$	$4.663\ 10^6$	-0.01
K_{12}	$-2.947\ 10^2$	$-2.948\ 10^1$	-0.02
K_{22}	$8.862\ 10^1$	$8.862\ 10^1$	0.0
K_{33}	$1.793\ 10^2$	$1.710\ 10^2$	+4.8
K_{44}	$1.145\ 10^3$	$1.142\ 10^3$	+0.28
$F_1^{(a)}$	$7.139\ 10^1$	$6.784\ 10^1$	+4.9
$M_1^{(a)}$	2.496	2.496	-0.02

Table 3.6: Non-zero stiffness (N, N m, N m^2) and forcing vector (N, N m) results for CH-47D active blade section (front D-spar + fairing) – (K_{ij}: 1 extension; 2 torsion; 3, 4 bending)

	Present	**Ref. [11] + ad hoc corrections**	% Difference
K_{11}	$5.171\ 10^6$	$5.989\ 10^6$	-13.6
K_{12}	$-3.012\ 10^2$	$-2.948\ 10^2$	+2.2
K_{22}	$9.872\ 10^1$	$1.085\ 10^2$	-9.1
K_{33}	$1.908\ 10^2$	$1.818\ 10^2$	+4.9
K_{44}	$4.390\ 10^3$	$3.923\ 10^3$	+11.9
$F_1^{(a)}$	$8.442\ 10^1$	$6.784\ 10^1$	+24.4
$M_1^{(a)}$	2.362	2.312	+2.1

The twist actuation rate results are in Table 3.7, and the experimental data using the test specimen are also compared with the analysis results. As it is expected, the result from the present formulation shows an overestimated twist rate. The discrepancies are primarily caused by the limited capability of the present analysis to model minor structural members like foam cores and ballast weights. Another limitation is that the present model is valid only when dealing with thin-walled section; however, the CH-47D active blade has a quite thick wall section at the front D-spar. Furthermore, the experimental twist actuation of the CH-47D active blade may be lower than originally expected from a flawless construction. After slicing the CH-47D

Table 3.7: Twist actuation rate comparison for CH-47D active blade (D-spar only and full cross-section: analyses and experiment)

	D-Spar only		D-Spar+Fairing	
	Twist Actuation (deg/m)	Difference	Twist Actuation (deg/m)	Difference
Present	3.13	27%	2.86	38%
Ref. [11]	3.13	27%	-	-
Ref. [11] + ad hoc corrections	2.81	16%	2.55	23%
Experiment [6]	2.46	-	2.06	-

examining the inner structure, it turned out that some defects developed within the blade during its manufacturing partially degraded its actuation performance [28].

Chapter 4

Study on the Actuation Constants

4.1 Overview

As described in Chapter 2 and 3, the analytical model established in this thesis shows a good correlation with the other existing analytical models and experimental data, especially in terms of the stiffness constants in the 2-D constitutive relations, Eq. (2.21).

As for the piezoelectric actuation vector, there has been few analytical models developed so far to analyze even a single-cell beam, and no attempt has been reported yet in the literature for the multiple-cell active beam analysis. The most popular class of single-cell active beam model encountered in the literature is based on the passive beam structural modeling of Rehfield [14] (e.g., Song and Librescu [12] ; duPlessis and Hagood [11] ; Wilkie, Belvin and Park [13]) as discussed in Chapter 1. The model developed and implemented by duPlessis and Hagood [11] is selected for this study as a representative for this class, and it is referred to herein as *modified Rehfield model*. In what follows, the difference between these two analytical models is further investigated by analytical and numerical comparisons, especially regarding the actuation constants.

The aeroelastic requirements tend to restrict the range of variation of the blade torsional stiffness, and it is necessary to find the relation between that and the maximum twist actuation obtained in a realistic integrally twisted multi-cell blade. This

chapter also concentrates on studying the relation between twist actuation and torsional stiffness of active rotor blades by analytical as well as numerical examples. Results indicate that potential improvement may be in the opposite direction to the conventional design belief that "by reducing torsional stiffness, one would get a larger twist actuation."

4.2 Analytical Examination of Actuation Components

The present cross-sectional analysis yields the constitutive relation based on a 4×4 stiffness matrix and an additional column vector associated with the actuation effects as in Eq. (2.21).

The formulation adopted in the modified Rehfield model is based on a 7×7 stiffness matrix, where (two) transverse shear and restrained warping degrees of freedom are explicitly added to the four classical degrees of freedom. Therefore, a consistent condensation to a 4×4 matrix is necessary for a meaningful comparison between them. This condensation is implemented through minimization of the potential energy with respect to the extra degrees of freedom as described, for example, in Hodges, Atilgan, Cesnik and Fulton [24]. A 7×1 actuation vector can be reduced to a 4×1 representation in a similar procedure. The analytical reduction procedure on the modified Rehfield model results in reasonably complex expressions for the actuation components. The 4×4-base expressions of both theories are presented in Table 4.1, and the reduced equations for the modified Rehfield method is based on the assumption of a beam without twist-shear coupling.

As one can see, the expressions due not coincide in general and this can be attributed in large by the different (out-of-plane) warping functions used in the formulation (inplane warping became negligible due to the thin-walled assumption). Rehfield [14] uses an *ad hoc* warping function, while the present asymptotical method calculates it from the basic original shell statement. Discussion of the difference in

Table 4.1: Analytical expressions of the actuation components for single-cell active beam

$F_1^{(a)}$	**Present**	$\oint A^{(a)}ds - \oint \frac{B}{C}C^{(a)}ds + \frac{\oint \frac{B}{C}ds}{\oint \frac{1}{C}ds}\oint \frac{1}{C}C^{(a)}ds$
	modified Rehfield	$\oint A^{(a)}ds - \frac{\oint C(\frac{\partial y}{\partial s})ds}{\oint C(\frac{\partial y}{\partial s})^2 ds}\oint C^{(a)}(\frac{\partial y}{\partial s})ds - \frac{\oint C(\frac{\partial z}{\partial s})ds}{\oint C(\frac{\partial z}{\partial s})^2 ds}\oint C^{(a)}(\frac{\partial z}{\partial s})ds$
$M_1^{(a)}$	**Present**	$\frac{\oint \frac{1}{C}C^{(a)}ds}{\oint \frac{1}{C}ds}A_e$
	modified Rehfield	$\frac{\oint \frac{1}{G_{eff}}C^{(a)}ds}{\oint \frac{1}{G_{eff}}ds}A_e$
$M_2^{(a)}$	**Present**	$\oint A^{(a)}zds - \oint \frac{B}{C}C^{(a)}zds + \frac{\oint \frac{B}{C}zds}{\oint \frac{1}{C}ds}\oint \frac{1}{C}C^{(a)}ds$
	modified Rehfield	$\oint A^{(a)}zds + \oint \left\{\langle \xi D^{11\gamma\delta}d_{3\gamma\delta}E_3\rangle - \frac{\langle \xi D^{22\gamma\delta}d_{3\gamma\delta}E_3\rangle}{\langle D^{2222}\rangle}\right\}(\frac{\partial y}{\partial s})ds$
$M_3^{(a)}$	**Present**	$-\oint A^{(a)}yds + \oint \frac{B}{C}C^{(a)}yds - \frac{\oint \frac{B}{C}yds}{\oint \frac{1}{C}ds}\oint \frac{1}{C}C^{(a)}ds$
	modified Rehfield	$-\oint A^{(a)}yds + \oint \left\{\langle \xi D^{11\gamma\delta}d_{3\gamma\delta}E_3\rangle - \frac{\langle \xi D^{22\gamma\delta}d_{3\gamma\delta}E_3\rangle}{\langle D^{2222}\rangle}\right\}(\frac{\partial z}{\partial s})ds$

the warping function between the asymptotical formulation and others, including Rehfield [14], can be found in Berdichevsky, Armanios, and Badir [26]. However, for certain configurations, the difference vanishes and the formulations coincide. This is definitely the case for isotropic beams, where all the terms are identical. For $F_1^{(a)}$, the leading term is the same, but the two following ones are totally different. The terms in the present approach comes from the effects of warping associated with extension. The terms in the modified Rehfield are associated with the extension-shear coupling. So, all those terms will vanish and the results coincides when there is no extension-shear coupling present in the lay-ups ($B \equiv 0$). For $M_1^{(a)}$, the two expression will coincide when the beam has constant stiffness and thickness along its cross section circumference (then $C \equiv G_{eff}$). Finally, for $M_2^{(a)}$ and $M_3^{(a)}$, the leading terms are identical, but the remaining is totally different in nature. The second integral on the modified Rehfield method comes from an attempt to introduce *ad hoc* corrections due to thickness effects (thick-wall effects [11]), and it will be not considered in this comparison. The two other terms in the present formulation come from the warping associated effects, and there are two situations when they will disappear from the formulation: *i*) there is no extension-shear coupling ($B \equiv 0$); and/or *ii*) the beam has a constant stiffness (including the active layers) and thickness distribution along the cross section circumference. As one can see, for a generic lay-up, the popular Rehfield-based models will present qualitative discrepancies from the asymptotically correct one.

4.3 Numerical Examination of Actuation Components

Next, one should consider the quantitative aspects of the discrepancies described above. The example selected here is the single-cell airfoil-shaped beam with integral piezoelectric actuators that was manufactured and tested by duPlessis and Hagood [11], the same one as shown in Fig. 3-2. It is based on a NACA 0012 airfoil with $[0°]_6$ E-Glass on the contour and $[+45°]$ active fiber composite on part of the top surface and $[-45°]$ on part of the bottom surface as well. The stiffness matrix reveals that this blade presents extension-shear, extension-torsion and shear-bending couplings.

Two different actuation modes are considered here. The first one is main twist actuation, responsible for the original $\pm 45°$ orientation of active plies. The twist actuation is obtained through applying the electric field of the same sign as the sign of the active plies' angles in the upper and lower skin. As a result, a significant amount of the actuation is obtained in the twist component, $M_1^{(a)}$, and also in the extensional one, $F_1^{(a)}$. The latter is considered to result from an extension-twist coupling. The other two components in bending, $M_2^{(a)}$ and $M_3^{(a)}$, are of negligible magnitude. The numerical results are in Table 4.2 and in which a reasonably good agreement is shown for $M_1^{(a)}$. However, a greater discrepancy appears for $F_1^{(a)}$ and further numerical analysis reveals that the second integral in the present formulation plays the main part in the discrepancy. It is also worth noticing that for $M_2^{(a)}$ and $M_3^{(a)}$, the contribution from the second integral in the modified Rehfield model is not significant in this case due to the very thin wall of this airfoil-shaped cross section. Tip rotation for different levels of applied voltage was already shown in Fig. 3-3. Numerical discrepancies for the tip rotation are small and both theories compare well with experimental results.

Another possible way of actuation is main bending in which the electric field has opposite sign as compared to the previous case, inducing considerable bending in the flap direction. Table 4.2 also shows the numerical results of this case, and the only non-zero component is the flapping actuation $M_2^{(a)}$, as expected. However, a

Table 4.2: Numerical comparison of actuation vector components for airfoil-shaped beam

Type of Actuation	Analysis Model	$F_1^{(a)}$	$M_1^{(a)}$	$M_2^{(a)}$	$M_3^{(a)}$
Twist Actuation	**Present**	$-3.255\ 10^{1}$	$1.170\ 10^{-1}$	0	$-2.557\ 10^{-3}$
	modified Rehfield	$-4.117\ 10^{1}$	$1.179\ 10^{-1}$	0	$-3.192\ 10^{-4}$
Bending Actuation	**Present**	0	0	$-8.350\ 10^{-2}$	0
	modified Rehfield	0	0	$-9.243\ 10^{-2}$	0

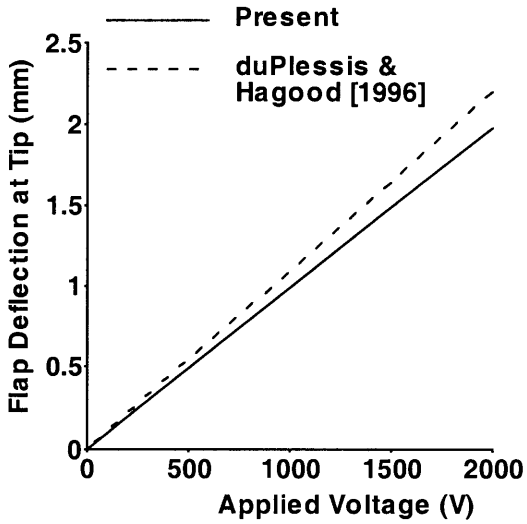


Figure 4-1: Flapwise deflection of the single-cell active blade under bending actuation

discrepancy is also found and this is resulted from the second integral in the present model, similarly to the $F_1^{(a)}$ case described above. The integral including the effect of the thickness is still ineffective in the modified Rehfield model. Experimental data for the bending actuation are not available at this point and will be conduct in the future for further accuracy assessment. However, a numerical estimation of tip flapwise bending deflection shows significant discrepancies between the two models even for this weak-actuated beam as shown in Fig. 4-1. This indicates that discrepancies can be significant on the predicted behavior of the blade response.

4.4 Twist-Related Relationship from the Present Formulation

Analytical expressions from the present model derived in Chapter 2 are given as follows for the torsional stiffness K_{22}, twisting actuation moment $M_1^{(a)}$, and a simple linear estimate of the resulting twist actuation $\theta_1'^{(a)}$ assuming no couplings with torsion.

$$K_{22} = \frac{\int_2 \frac{1}{C} ds [A_{eI}^2 + 2A_{eI}A_{eII} + A_{eII}^2] + \int_1 \frac{1}{C} ds A_{eII}^2 + \int_3 \frac{1}{C} ds A_{eI}^2}{\int_1 \frac{1}{C} ds \int_2 \frac{1}{C} ds + \int_2 \frac{1}{C} ds \int_3 \frac{1}{C} ds + \int_3 \frac{1}{C} ds \int_1 \frac{1}{C} ds} \tag{4.1}$$

$$\begin{aligned} M_1^{(a)} &= \frac{\left[\int_3 \frac{1}{C} ds \int_{1+2} \frac{1}{C} C^{(a)} ds A_{eI} + \int_1 \frac{1}{C} ds \int_{2+3} \frac{1}{C} C^{(a)} ds A_{eII}\right]}{\int_1 \frac{1}{C} ds \int_2 \frac{1}{C} ds + \int_2 \frac{1}{C} ds \int_3 \frac{1}{C} ds + \int_3 \frac{1}{C} ds \int_1 \frac{1}{C} ds} + \\ &+ \frac{\int_2 \frac{1}{C} ds \left[\int_{1+2} \frac{1}{C} C^{(a)} ds A_{eI} + \int_{2+3} \frac{1}{C} C^{(a)} ds A_{eI}\right]}{\int_1 \frac{1}{C} ds \int_2 \frac{1}{C} ds + \int_2 \frac{1}{C} ds \int_3 \frac{1}{C} ds + \int_3 \frac{1}{C} ds \int_1 \frac{1}{C} ds} + \\ &+ \frac{\int_2 \frac{1}{C} ds \left[\int_{1+2} \frac{1}{C} C^{(a)} ds A_{eII} + \int_{2+3} \frac{1}{C} C^{(a)} ds A_{eII}\right]}{\int_1 \frac{1}{C} ds \int_2 \frac{1}{C} ds + \int_2 \frac{1}{C} ds \int_3 \frac{1}{C} ds + \int_3 \frac{1}{C} ds \int_1 \frac{1}{C} ds} \end{aligned} \tag{4.2}$$

$$\begin{aligned} \theta_1'^{(a)} \approx \frac{M_1^{(a)}}{K_{22}} &= \frac{\left[\int_3 \frac{1}{C} ds \int_{1+2} \frac{1}{C} C^{(a)} ds A_{eI} + \int_1 \frac{1}{C} ds \int_{2+3} \frac{1}{C} C^{(a)} ds A_{eII}\right]}{\int_2 \frac{1}{C} ds [A_{eI}^2 + 2A_{eI}A_{eII} + A_{eII}^2] + \int_1 \frac{1}{C} ds A_{eII}^2 + \int_3 \frac{1}{C} ds A_{eI}^2} + \\ &+ \frac{\int_2 \frac{1}{C} ds \left[\int_{1+2} \frac{1}{C} C^{(a)} ds A_{eI} + \int_{2+3} \frac{1}{C} C^{(a)} ds A_{eI}\right]}{\int_2 \frac{1}{C} ds [A_{eI}^2 + 2A_{eI}A_{eII} + A_{eII}^2] + \int_1 \frac{1}{C} ds A_{eII}^2 + \int_3 \frac{1}{C} ds A_{eI}^2} + \\ &+ \frac{\int_2 \frac{1}{C} ds \left[\int_{1+2} \frac{1}{C} C^{(a)} ds A_{eII} + \int_{2+3} \frac{1}{C} C^{(a)} ds A_{eII}\right]}{\int_2 \frac{1}{C} ds [A_{eI}^2 + 2A_{eI}A_{eII} + A_{eII}^2] + \int_1 \frac{1}{C} ds A_{eII}^2 + \int_3 \frac{1}{C} ds A_{eI}^2} \end{aligned} \tag{4.3}$$

The same nomenclature is adopted as in Chapter 2 except that the following notations for the integration paths are used along with the definition in Fig. 2-2.

$$\begin{aligned} \int_1(\cdot)ds &= \int_0^{s_1}(\cdot)ds \\ \int_2(\cdot)ds &= \int_{s_1}^{s_2}(\cdot)ds \\ \int_3(\cdot)ds &= \int_{s_2}^{s_3}(\cdot)ds \end{aligned} \tag{4.4}$$

C and $C^{(a)}$ are terms proportional to the stiffness of the wall (passive and active, respectively) and their definitions are presented in Eq. (2.12). The function C can be also represented in terms of the classical laminated plate theory constants as

$$C = 4\left(A_{66} - \frac{A_{26}^2}{A_{22}}\right) \tag{4.5}$$

Note that there seems to be significant coupling between cells I and II in case of a two-cell beam for both the passive and active components, making its behavior complex. Simpler equations are obtained for the case of a single cell beam. By assuming that C becomes infinitesimal at the web in Eqs. (4.1)–(4.3), one can reduce them to a single-cell model, yielding

$$K_{22} = \frac{1}{\oint \frac{1}{C} ds} A_e^2 \tag{4.6}$$

$$M_1^{(a)} = \frac{\oint \frac{1}{C} C^{(a)} ds}{\oint \frac{1}{C} ds} A_e \tag{4.7}$$

$$\theta_1^{(a)} \approx \oint \frac{1}{C} C^{(a)} ds \frac{1}{A_e} \tag{4.8}$$

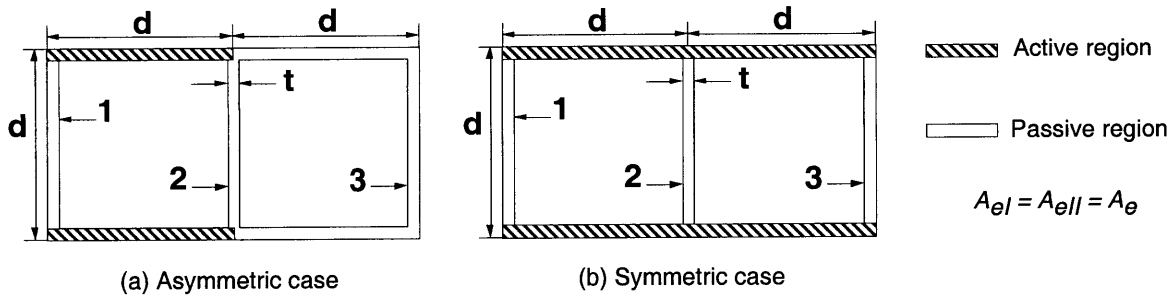


Figure 4-2: Baseline configurations of two-cell box beams

4.5 Twist Actuation Results

From the analytical results summarized in Eqs. (4.1)–(4.3), one can see that the actuation behavior of two-cell active beam is complex and little can be analytically done with those equations directly. Therefore, in what follows, two approaches are taken to study the influence of the blade torsional stiffness on the twist actuation. First, we continue the analytical study by prescribing the geometry of the cross section such that Eq. (4.3) can be simplified. Secondly, numerical studies are conducted on what will be presented as the design for the ATR blade.

4.5.1 Two-cell box beam cases

To further investigate analytically the expressions presented before, two two-cell box beams are considered: one that has symmetric distribution of active layers (top and bottom walls), and the other with asymmetric distribution. The stiffness parameter C and $C^{(a)}$ are assumed constant along the section contours. The baseline configuration of the two box beams are depicted in Fig. 4-2, and Table 4.3 summarizes the twist actuation variation when the stiffness parameter C is increased n times on the passive walls only. Note the opposite trends on the twist actuation presented in the asymmetric case for walls **1** and **3**, while changes in wall **2** do not change the twist actuation (even though all will increase the torsional stiffness). The symmetric case presents constant actuation regardless the changes on the stiffness of walls **1**, **2**, or **3**. Constant twist actuation is also obtained in the case of a single-cell active beam when C is varied on the passive regions (see Eq. (4.8)).

Table 4.3: Analytical results of two-cell box beam

	Asymmetric	Symmetric
Baseline	$\frac{\theta_1'^{(a)}}{\frac{C^{(a)}}{C}t \cdot d\frac{1}{A_e}} \approx 1$	$\frac{\theta_1'^{(a)}}{\frac{C^{(a)}}{C}t \cdot d\frac{1}{A_e}} \approx 2$
$C \rightarrow nC$ at wall **1**	$\frac{10n}{9n+1}$	2
$C \rightarrow nC$ at wall **2**	1	2
$C \rightarrow nC$ at wall **3**	$\frac{4n+6}{7n+3}$	2

4.5.2 ATR blade cases

Next, the relationship between torsional stiffness and twist actuation is investigated within variants of an ATR blade. The active regions are the front spar skins with embedded AFC layers, and all the other parts of the blade are passive (Fig. 4-3). Along with the two-cell ATR blade, two variations of single-cell version are also investigated here in order to conduct comparison between two-cell and single-cell active blade (see Fig. 4-5 and 4-6).

When the stiffness parameter C is changed - by adding or removing E-Glass plies at each region - the resulting twist actuation, twisting actuation moment, and torsional stiffness, all non-dimensionalized by the corresponding baseline values, are presented in Fig. 4-4. When adding passive plies at the nose and web, the twist actuation increases, while it decreases when the passive plies are added at the active region and fairing (Fig. 4-4 (a)). The torsional stiffness (Fig. 4-4 (b)) is proportional to the variation on the wall thickness as expected, and the twist actuation moment (Fig. 4-4 (c)) increases when increasing the stiffness in members other than the active ones. However, for some of them, the increase in the actuation moment is offset by the sharp decrease in the rate of twist (Fairing - Fig. 4-4 (a)). Therefore, the twist actuation behavior appears in some aspects similar to the one of the asymmetric box beam presented before.

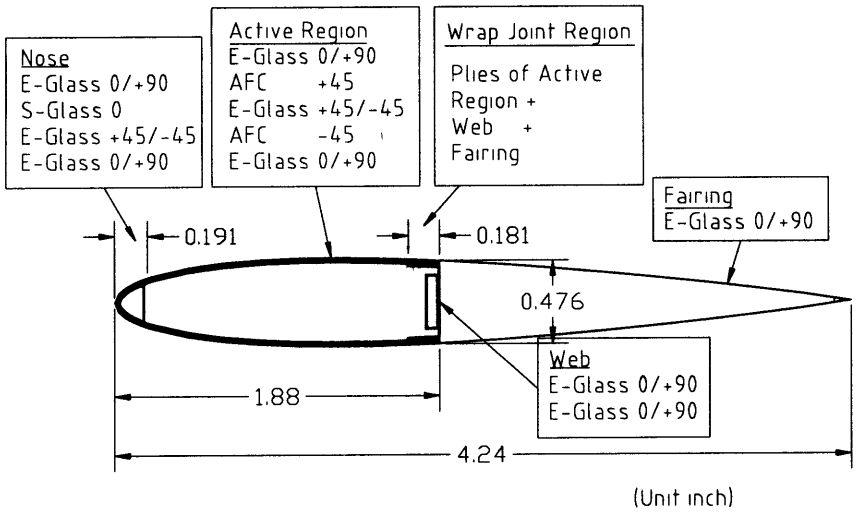
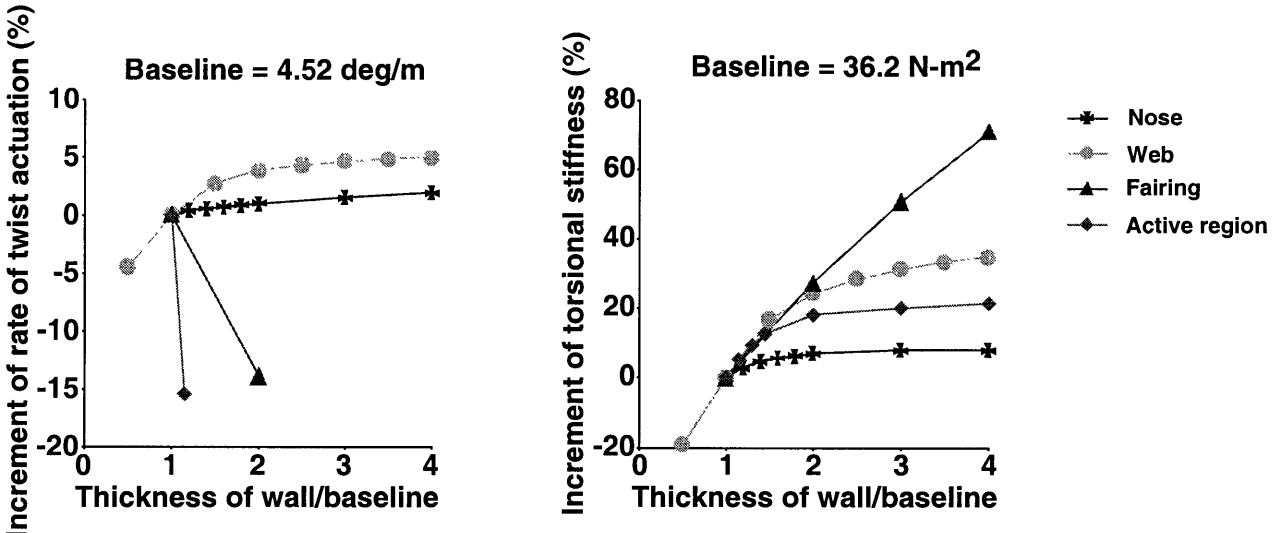


Figure 4-3: Schematic diagram of the ATR blade design

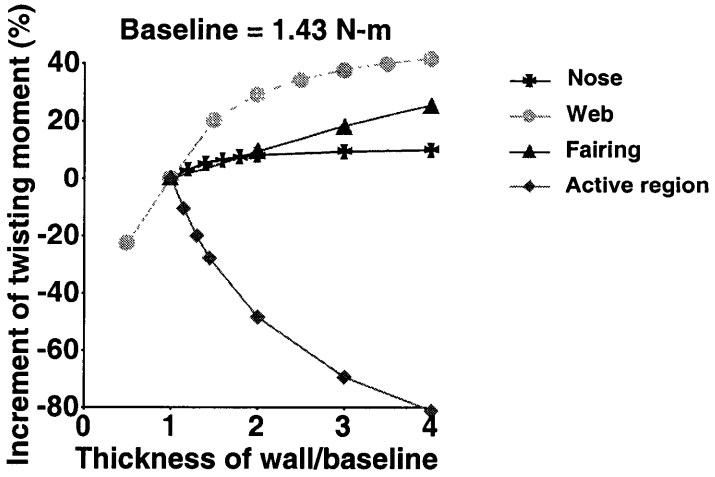
Thus, in summary, net changes of twist actuation in the two-cell active beam is dependent upon the local stiffness variation of either active region or passive region. Also, it is found that there is a possibility of twist actuation increase in the currently considered configuration even when adding passive plies at the region other than the active one (i.e., web and nose). This is in contrast to the results obtained if one considers a single cell blade, where the twist actuation is at best not altered when stiffness is added to passive regions, dropping significantly when the additional stiffness happens at the active regions only.

To illustrate this issue even further, consider two possible single-cell derivatives of the ATR blade. One is the configuration in which the fairing part is eliminated, and which is referred to as "D-spar single-cell beam" (Fig. 4-5). The other is one without the web, and it is called just "single-cell airfoil-shaped beam" (Fig. 4-6). The results for both configurations are plotted in Fig. 4-7, and 4-8, respectively. As it is expected already from the analytical expressions, (4.6)–(4.8), the twist actuation is not changed by adding or removing passive plies at regions other than the active region. The decrease of twist actuation when increasing the local stiffness of the active region could be clearly seen in Eq. (4.8). So, in the example of the D-spar case, accounting for the stiffness effects of the fairing by adding it to the stiffness of



(a) Twist Actuation

(b) Torsional stiffness



(c) Twisting actuation moment

Figure 4-4: Twist actuation result of two-cell ATR blade

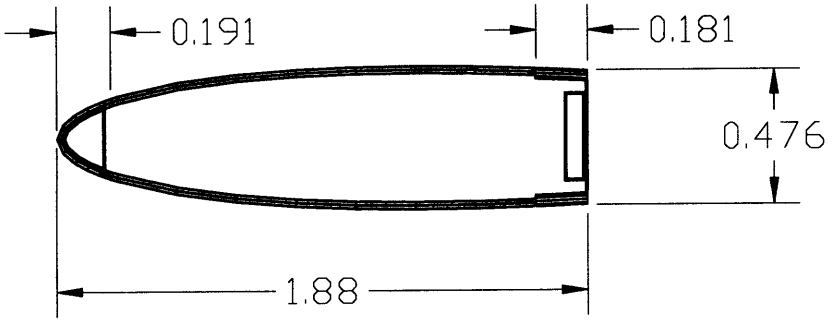


Figure 4-5: Baseline configuration of D-spar single-cell derivative beam (dimensions are in inches)

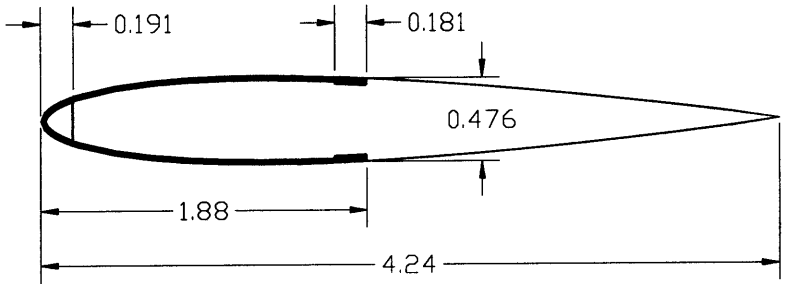
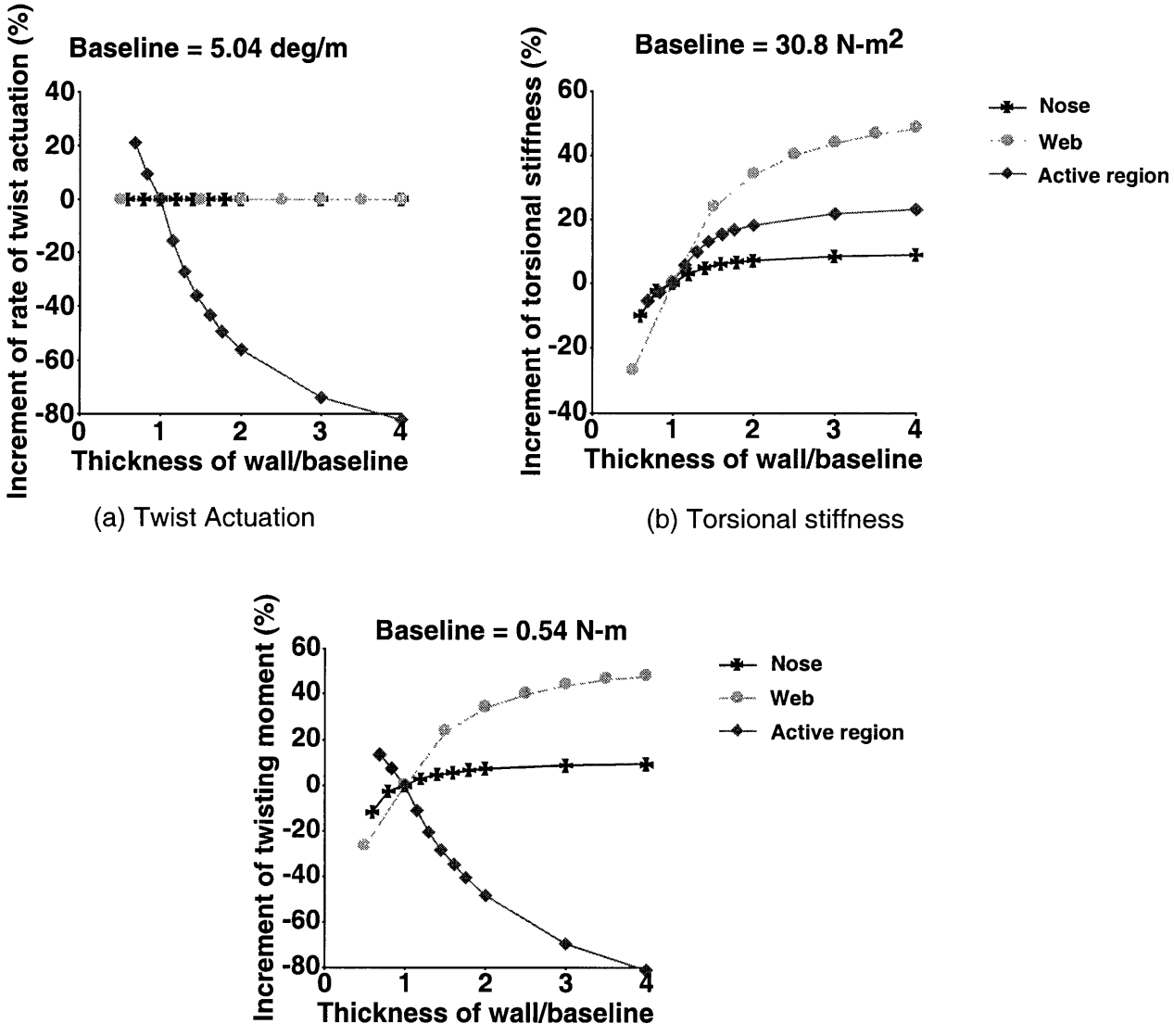


Figure 4-6: Baseline configuration of single-cell airfoil-shaped derivative beam (dimensions are in inches)

the front spar without carrying it to all aspects of the model will result in an incorrect prediction of the twist performance (notice the change on the baseline values for the torsional stiffness, active twisting moment, and twist actuation compared to reference baseline values presented before, Fig. 4-4).

Therefore, a conventional approximation using single-cell beam to predict multi-cell beam actuation behavior is not sufficient and can be seriously misleading. The single-cell model does not capture the complex interaction present in the multi-cell structure.

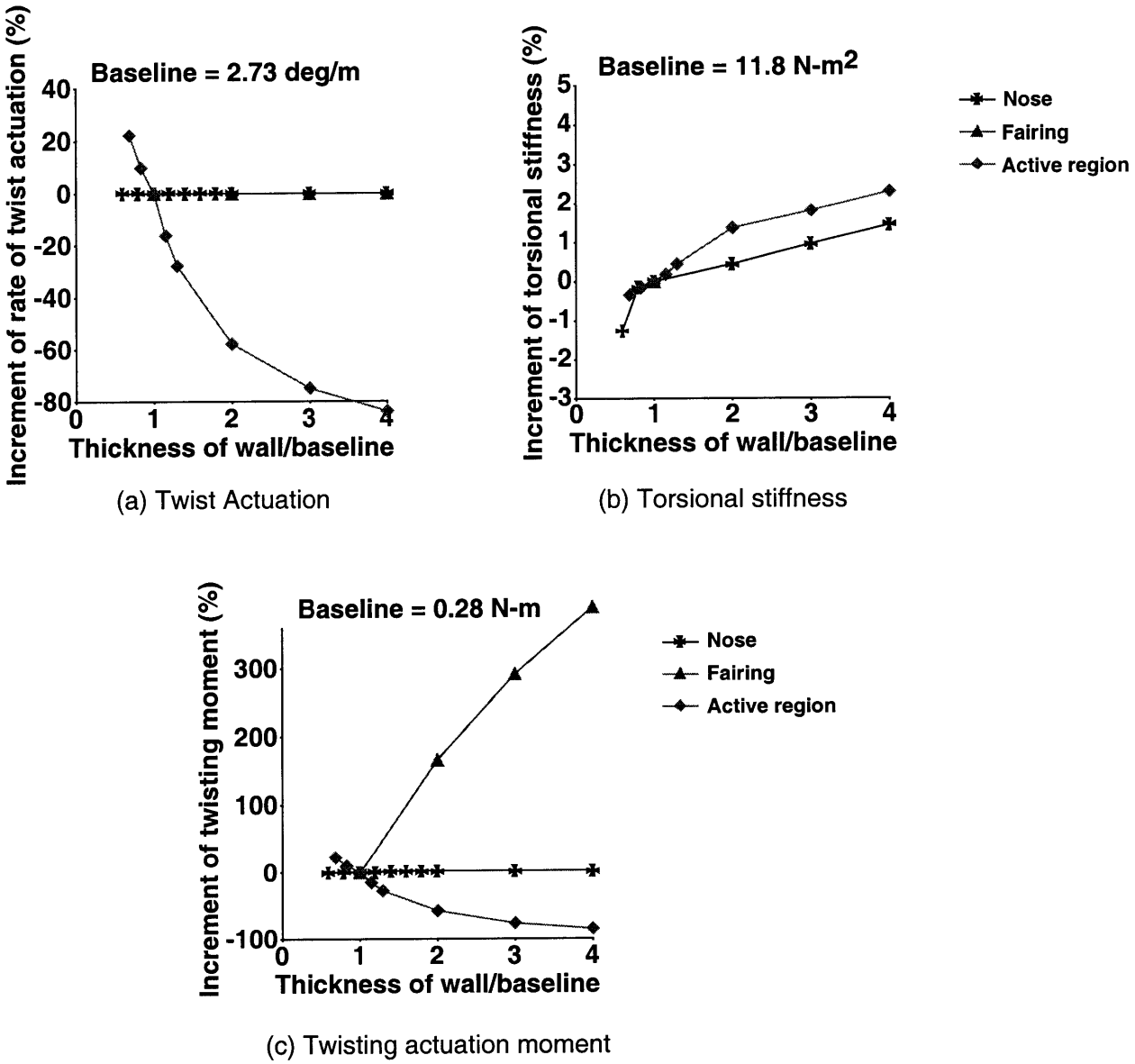


(a) Twist Actuation

(b) Torsional stiffness

(c) Twisting actuation moment

Figure 4-7: Twist actuation result of D-spar single-cell beam



(a) Twist Actuation

(b) Torsional stiffness

(c) Twisting actuation moment

Figure 4-8: Twist actuation result of single-cell airfoil-shaped beam

Chapter 5

Design Requirements and Procedure

5.1 Overview

The design and analysis of the ATR prototype blade is conducted using the tool developed by the present formulation. The new active blade is based on the external dimension and the aerodynamic properties of an existing passive blade. Therefore, there is a set of requirements that needs to be satisfied during design modifications to the existing baseline blade. Such design requirements are discussed in detail at first, and then a practical methodology for rotor blade design modification is presented. A design flowchart is devised in order to itemize the activities of the design/analysis tasks and arrange them in an appropriate flow, while at the same time checking if each of the requirements is satisfied.

5.2 Design Requirements

The new ATR blade is designed based on the external dimension and aerodynamic properties of an existing passive blade which is already in use for wind-tunnel testing at NASA Langley Research Center. Table 5.1 summarizes the general dimension and shape characteristics of the existing passive blade, and most of these properties will

be retained in the new design.

Table 5.1: General properties of the existing baseline rotor

rotor type	fully articulated
number of blades, b	4
blade chord, c	0.108 m
blade radius, R	1.397 m
solidity, $\sigma = bc/\pi R$	0.0982
airfoil section	NACA0012
blade pretwist	$-10°$ (linear from $0R$ to tip)
hinge offset	0.0762 m
root cutout	0.3175 m
pitch axis	25% chord
elastic axis	25% chord
center of gravity	25% chord
rotor rotational speed	687.5 RPM
rotor overspeed	756.25 RPM

Inertial and structural properties of the passive baseline blade are listed in Table 5.2, but some of the structural properties may be changed due to the design modifications which follow. Those changes of the structural properties are unavoidable in order to insert the active material into the existing passive structure. On the contrary, inertial properties should not be altered much from the baseline values because Lock number is one of the scaling parameters that should be kept unchanged. Detailed discussion about these design parameters is presented below.

Table 5.2: Structural properties of the existing baseline rotor blade (at $0.5R$)

property	baseline value
section mass per unit span length	0.696 kg/m
section torsional inertia per unit span length	$3.174\ 10^{-4}$ kg-m^2/m
spar area, A	$1.445\ 10^{-4}$ m^2
flapwise stiffness, EI_{flap}	$4.331\ 10^{1}$ N-m^2
chordwise stiffness, EI_{lag}	$7.026\ 10^{3}$ N-m^2
torsional stiffness, GJ	$4.847\ 10^{1}$ N-m^2
axial stiffness, EA	$2.0\ 10^{6}$ N

The rotor blade scaling parameters are summarized in Table 5.3, where the values of baseline passive blade are listed and the necessity of keeping the baseline values

during the design modification is shown for each parameter.

It is now necessary to discuss each issue of the rotor scaling parameters summarized in Table 5.3 and extract the practical requirements which will be considered in the further design process. They are as follows:

- In order to retain Lock number, γ, at a specified value, namely 4.55 here, the blade flapping inertia, I_β, should be kept within certain range since the aerodynamic forces are fixed once the airfoil section is selected. (Lock number is defined as the ratio between the aerodynamic forces and inertial forces acting on rotor blade.) This requirement, in turn, specifies a certain limit of the mass per unit span length.

- Three locations in the cross section, i.e., chordwise center of gravity, tension axis, and elastic axis should be placed at 25% chordwise position. This requirements are related with the aeroelastic stability of the rotor system.

  1. It is expected that the adjustment of c.g. location is accomplished by adding some tantalum ballast weights near either the nose or web, while the total mass per unit span length is constrained to give the target value.

  2. Tension axis is defined as the point for which the application of a tensile force will not produce any bending deformation, and is calculated using the following formula (see [15], and note that its formulation of single-cell beam is based on the reference to tension axis. See also [29]):

$$x_{ta} = \frac{\oint K_{11} x \, ds}{\oint K_{11} \, ds} \tag{5.1}$$

     where, K_{11} is the axial stiffness as in Eq. (2.21).

  3. Elastic axis is the locus of the shear centers, and shear center is defined as the point for which the application of a transverse shear force will not produce any torsional deformation. In order to obtain the elastic axis position, the stiffness constants in both the transverse shear and torsional components are required. However, it is not possible to calculate elastic axis in

Table 5.3: Summary of rotor blade scaling parameters

scaling parameter	description	baseline blade value	ATR design required to match ?
$EI_{flap}/m\Omega^2R^4$	ratio of flapwise elastic forces to centrifugal forces	0.00342	yes, approximately (can be varied if necessary, depending on rotating frequencies.)
$EI_{lag}/m\Omega^2R^4$	ratio of chordwise elastic forces to centrifugal forces	0.0555	no (usually take whatever we got, based on other design constraints)
$GJ/m\Omega^2R^4$	ratio of torsional elastic forces to centrifugal forces	0.00383	no (can be lowered to reach twist actuation target)
x_{ea}/c	elastic axis to chord ratio	0.25 (from LE)	yes (required)
x_{ta}/c	tension axis to chord ratio	0.25 (from LE)	yes (required)
x_{cg}/c	chordwise c.g. to chord ratio	0.25 (from LE)	yes (ballast as necessary to achieve this)
$\rho(5.73)cR^4/I_\beta$	Lock number, γ	4.55 (for $\rho = \rho_o$)	yes, approximately
k_m^2/R^2	nondimensional polar mass radius of gyration squared	$2.34\ 10^{-4}$	no
$\Omega R/a$	hover tip Mach number	0.603 (heavy medium)	matched implicitly
Ω^2R/g	variation of Froude number	680	matched implicitly
$V_\infty/\Omega R$	rotor advance ratio, μ	0–0.5	matched implicitly
c/R	ratio of chord to radius, and all geometric ratios	0.0771	matched implicitly
$\rho Vc/\mu$	Reynolds number		matched implicitly

the present formulation since the transverse shear stiffness constants are not explicitly available. On the other hand, in the Rehfield model [15], the transverse shear stiffness constants are provided for a single-cell beam as part of the 6 $\times$ 6 stiffness matrix. Therefore, the 4 $\times$ 4 stiffness matrix obtained from the current two-cell beam formulation will be augmented by two components of transverse shear components from Rehfield model considering only front spar in order to give fully-populated 6 $\times$ 6 matrix. In case structural material is concentrated at the front spar, such an augmentation gives a meaningful estimate of the stiffness matrix.

Once the 6 $\times$ 6 stiffness matrix is obtained with respect to an arbitrary point, the location of elastic axis relative to that point is calculated using the following procedure [30]. Consider

$$\begin{Bmatrix} F_B \\ M_B \end{Bmatrix} = \begin{bmatrix} K_1 & K_3 \\ K_3^T & K_2 \end{bmatrix} \begin{Bmatrix} \gamma \\ \kappa \end{Bmatrix} \tag{5.2}$$

which is the extended constitutive relation associated with Eq. (2.21) or Eq. (2.31), except that F_B in Eq. (5.2) is composed of two components of transverse shear forces as well as an axial force. From a transformation that makes the couplings between the forces and the resultant couples null, one gets a linear equation as follows:

$$[K_1][y] = -[K_3] \tag{5.3}$$

Then, the coordinates of the shear center becomes,

$$\text{shear center} = \begin{Bmatrix} x_1 = -y_{23} \\ x_2 = y_{13} \end{Bmatrix} \tag{5.4}$$

where y_{23} and y_{13} are the (2,3)-th and (1,3)-th element, respectively, of the 3 $\times$ 3 matrix y which is obtained in Eq. (5.3).

- The ratios of the three elastic moments, i.e., flapwise, chordwise, and torsional, may not need to be kept as the baseline values. However, since it is desirable that the dynamic characteristics of the newly design active blade be kept unaltered much from that of the original passive blade, especially for the torsional component, the first torsional natural frequency will be monitored in the design process. In general, the first torsional natural frequency of the rotor blade at normal rotor speed should not be smaller than N/rev from the viewpoint of the aeroelastic stability of the rotor system.

- Twist actuation performance is one of the most important requirements in the ATR blade design. It is known that $\pm 2^{\circ}$ at the tip is sufficient twist actuation for the helicopter vibration reduction application [3]. Therefore, the target value of the twist actuation performance is set as $\pm 2^{\circ}/m$ at peak-to-peak high voltage application since the current ATR blade is about 1m long. This requirement is imposed at both static and dynamic conditions, and here the dynamic condition means a rotating environment at maximum rotor speed because the rotation increases the torsional stiffness.

- Structural integrity of the new blade design should be checked using one of the worst loading conditions which are expected to occur within the helicopter operating envelope. In this design, forward flight with the maximum speed is selected as the loading criterion. A comprehensive rotorcraft analysis code, CAMRAD II, is used to simulate such a forward flight condition and extract the magnitude of the loads acting on the internal blade structure. Before conducting the CAMRAD II analyses, the basic structural properties of the newly designed ATR blade needs to be estimated using the present design tool, and provided to CAMRAD II. Then, the largest magnitudes of the aerodynamic loads are extracted and combined with the centrifugal loads in order to give the worst loading values with a safety factor of 1.5. The present design tool has an extended capability of converting the 1-D global beam loading into the stress/strain existing in constituent composite plies within the skin lay-up. By

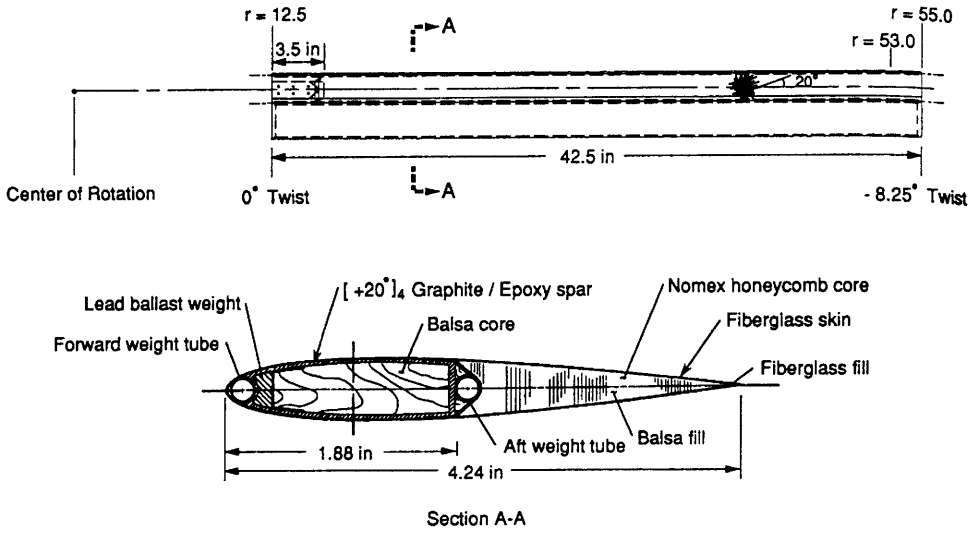


Figure 5-1: Original design of the baseline passive blade

adopting one of the appropriate failure theories related with static strength, for example, the maximum stress theory, the maximum strain theory, etc., the structural strength is confirmed. (Here, the maximum strain theory is adopted.)

5.3 Design Flowchart

According to the requirements set in the previous section, the practical design constraints need to be itemized and arranged in an appropriate flow. A resultant flowchart for the specific purpose of the current ATR blade design is devised and illustrated in Figs.5-2 and 5-3.

The design process starts with simplifying the baseline configuration given in the original passive blade because the original design has relatively complicated features such as different material used between the leading edge and trailing edge cores, and two weight tubes inserted near the nose and web which are to accommodate variable quantity of ballast weights (see Fig. 5-1). In an effort to reduce these complexities, foam will be used as material for the blade core at both leading edge and trailing edge because it is easy to fabricate into an airfoil shape and has sufficient stiffness and strength properties to be used as minor structural members.

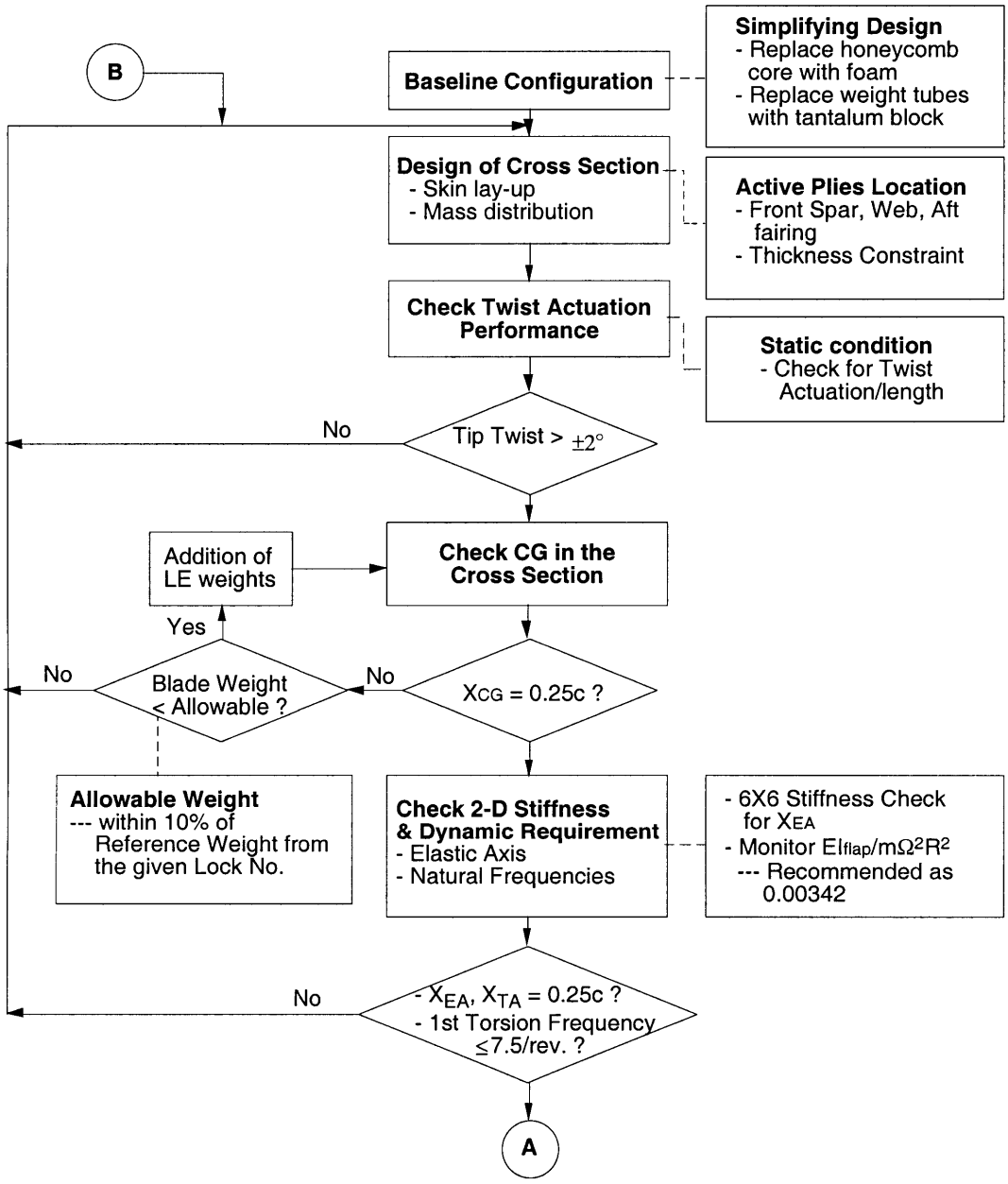


Figure 5-2: Flowchart of the ATR blade design tasks

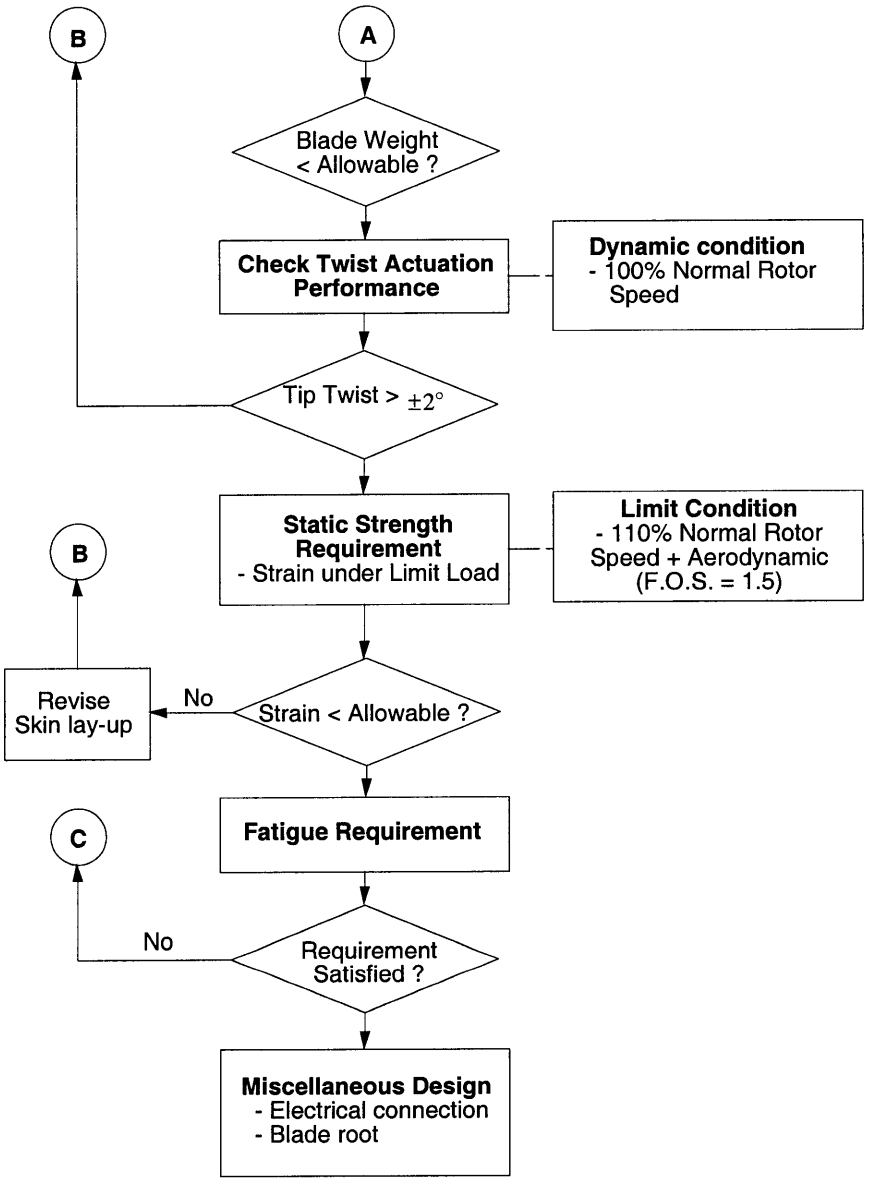


Figure 5-3: Flowchart of the ATR blade design tasks (cont'd)

The skin ply distribution in the cross section will be dealt with in the next step, and one of the most important issues is where to place the active material. This means to select which regions will contain the AFC plies, front spar skin, web plies, aft fairing skin or even another regions. The ply lay-up and active material distribution design are intimately related with all the requirements discussed above, therefore most of the returning loops which check the requirements and revise the lay-up design are extended to the very first activity of the design flowchart.

It is natural that the first check is conducted on the twist actuation performance at static condition. If the actuation performance is not satisfactory, a simple remedy that can be thought up is to add more AFC plies at the active region or to decrease torsional stiffness. However, it was found from the study on the twist actuation performance of the active beam that the latter is not necessarily true. (See Chapter 4.) Therefore, an iterative methodology is adopted implicitly to overcome such a complicated twist actuation performance problem.

The chordwise center of gravity in the cross section is estimated, and if it is not near the 25% chordwise position, ballast tantalum weights are added or deleted at both nose and web ply locations, while at the same time the total weight of the blade per unit span length is limited within the target value imposed from the specified Lock number,γ. At the beginning of the design process, the total weight of the blade per unit span is constrained within $\pm 10\%$ of the the target value, and more precise weight estimates will be sought later in the design process.

Then, the resultant stiffness properties and dynamic characteristics of the blade need to be checked. The location of the tension axis is calculated using Eq. (5.1), and a simple estimation of the elastic axis is performed by augmenting 4×4 stiffness matrix with two transverse shear components obtained from the Rehfield model considering only the single-cell structure of the front spar. The natural frequencies at normal rotor speed are also checked using the dynamic capability of the present formulation, especially the first torsional mode.

The twist actuation performance is computed in the dynamic condition to account for the actuation performance degradation due to the steady centrifugal force

generated at 100% normal rotor speed.

The structural integrity of the design is finally checked by applying the worst loading condition to the structure and comparing the stress/strain existing within the ply lay-up with the strength properties of the constituent material. If it turns out that a failure happens inside the structure, a reinforcement by adding more plies is generally required within the limit that the other requirements still be satisfied. It is expected that the active fiber material, PZT-5H, will be the most susceptible one to failure among those used in the ATR blade. Therefore, the lowest strength properties, which is the strength of the bare PZT-5H fiber without any structural reinforcement [10], are used as ultimate strength of the active fiber for a conservative structural design.

The fatigue requirement is an important design aspect even for model blades since the blade will be subject to cyclic loads during wind-tunnel testing. However, fatigue analysis is not considered to a full extent here since there is not enough data available regarding the cyclic loading and critical failure mode that are specific to the ATR blade construction. Nevertheless, one consideration is still included in the current design process: that the static strength considered in the structural integrity substantiation will use the strength value based on the endurance limit of the constituent materials. This should provide infinite life to the designed structure.

5.4 Structural Integrity Substantiation

It is necessary to establish the structural integrity substantiation procedure of the newly designed or modified ATR blade structure, and include it in the design tool. In the current design process, the maximum forward flight speed condition is selected as the worst loading case, and a helicopter comprehensive analysis code, CAMRAD II, is used to simulate such condition to extract the aerodynamic loads acting on the ATR blade. Prior to CAMRAD II analysis, the structural and inertial properties of the ATR design candidate are estimated by the formulation derived so far, and provided to CAMRAD II. As a result of CAMRAD II analysis, bending moments in

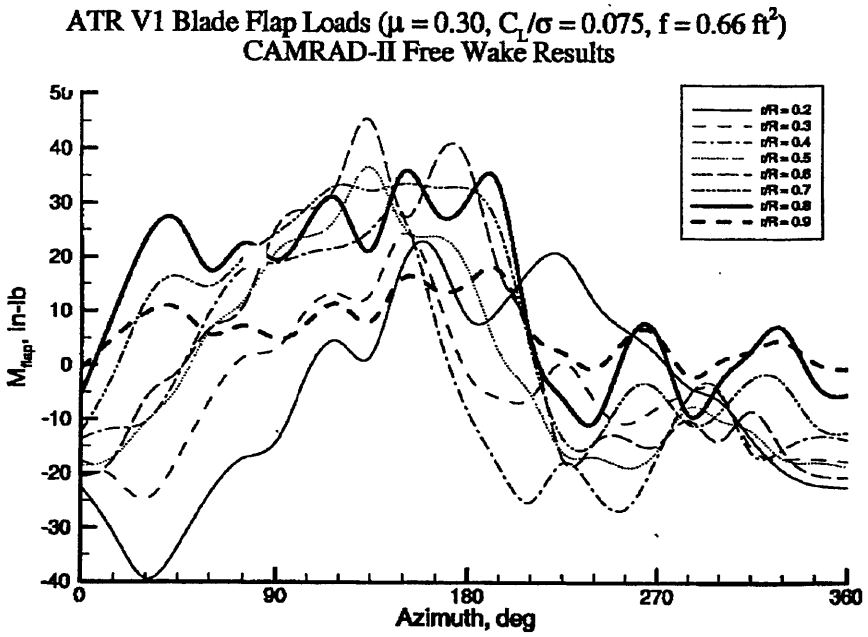


Figure 5-4: CAMRAD II prediction of flapwise bending moment

the two directions and torsional moments internal to the blade structure are predicted at discrete blade stations and azimuth locations. The distribution of flapwise bending moment, chordwise bending moment, and torsional moment are displayed in Fig. 5-4, 5-5 and 5-6, respectively.

The peak values of bending and torsional moments are selected among the distribution and combined with axial centrifugal load which is multiplied by a safety factor of 1.5 to give the worst case loads $\{F_B \; M_B\}^T$ as in Eq. (2.31). Using the procedure established in Section 2.4, the structural integrity of the designed blade under the set of worst loads can be analyzed.

Once the resulting stress level within the blade structure is compared with the ultimate strength of the constituent material, the structural integrity is completed. That will be also compared with the endurance limit of the material to check if the blade structure has an infinite life under the prescribed loading.

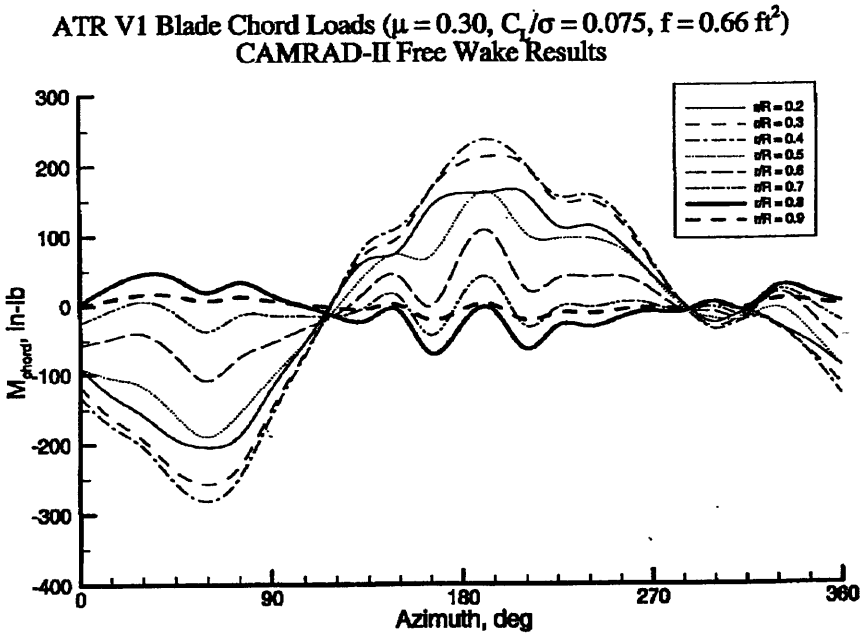


Figure 5-5: CAMRAD II prediction of chordwise bending moment

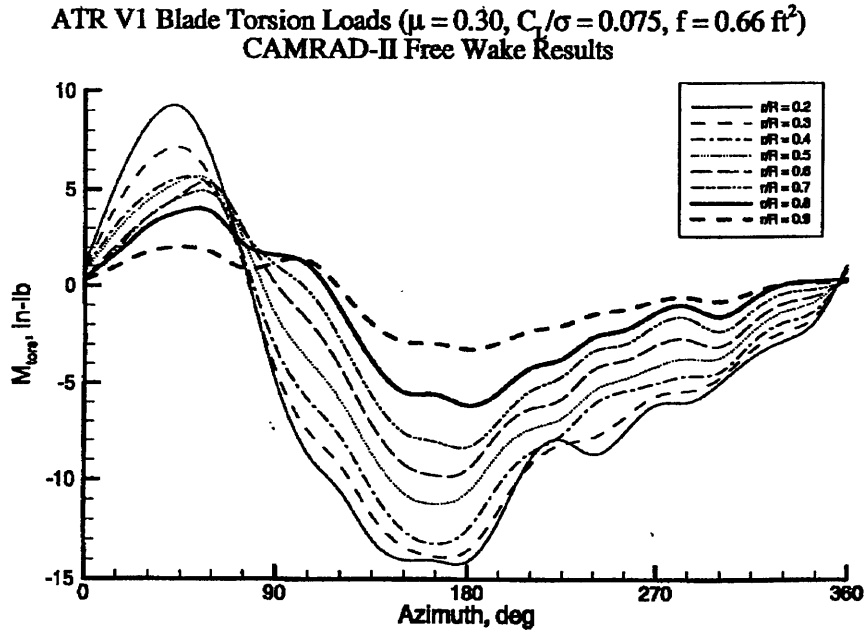


Figure 5-6: CAMRAD II prediction of torsional moment

Chapter 6

ATR Design Results

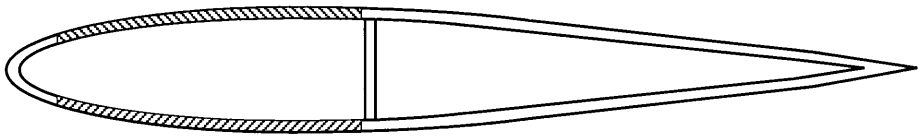
6.1 Overview

Schematic diagrams of three ATR design concepts to be analyzed are illustrated in Fig. 6-1.

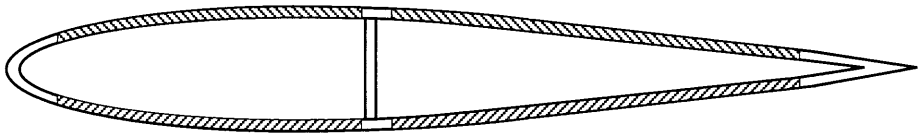
One simple design candidate is the one in which active layers are distributed only within the top and bottom skin plies of the front spar. This is called the '*active spar candidate*' since it has active structure concentrated within the front spar. It is expected that this concept will have its center of gravity and tension axis near the 25% chord, or easily adjusted to such.

A concept that can be extended from the first candidate is one which has active layers within the top and bottom skin plies of the fairing as well as the front spar, and it is called the '*active fairing candidate.*' It is apparent that this candidate will have a larger twist actuation compared to that of the active spar one. However, it will also present some difficulties associated with the location of the center of gravity and the other axes that may be displaced backward from 25% chord location.

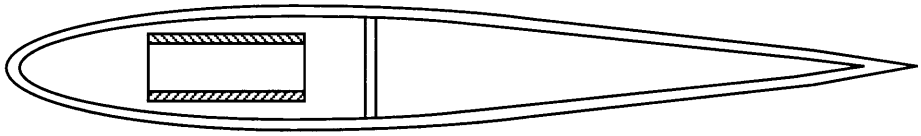
The third concept is one that has an active box beam inserted within the front spar and the twisting actuation moment of the box beam will be transmitted to the outer structure by some mechanism. This concept is called the '*active box beam candidate,*' and it might have a comparable twist actuation performance as the others, as well as benign characteristics to satisfy the design requirements. However, the mechanism of



(a) Classical candidate



(b) Active fairing candidate



(c) Active box beam candidate

Figure 6-1: Schematic diagram of the several ATR design candidates

the actuation moment transfer is not a trivial problem to be solved, increasing the risk associated with this concept.

The properties of the different materials used in each of the concepts are presented in Appendix C.

6.2 Active Spar Candidates and Variations

6.2.1 Analysis of the active spar candidates

The active spar candidates can be separated further in terms of the number of AFC layers inserted in the active region. The number of AFC layers will be considered in this design process to vary between 1 and 4 since more AFC plies than 4 layers in the active region turns out to give no significant increase on the twist actuation performance. (The actuation trend will be shown later.)

Table 6.1 summarizes the ply lay-up information of the four active spar candidates

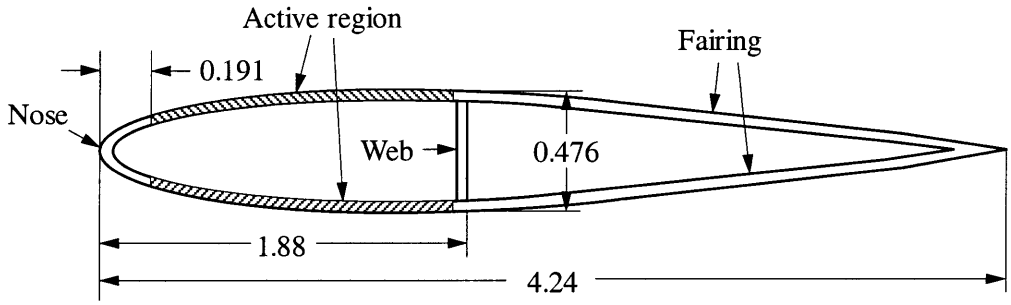


Figure 6-2: Schematic diagram of the active spar candidate (all dimensions are in inches).

under consideration, and a detailed diagram of these candidates including the dimensions of each region is shown in Fig. 6-2. It is apparent that the AFC plies should be oriented at $\pm 45°$ with respect to the blade radius in order to maximize torsional actuation moment. Next to each AFC ply, a layer of E-Glass is added to reinforce and electrically isolate the AFC plies. 0° E-Glass plies are also inserted at the top and bottom in order to provide axial strength.

Table 6.1: Lay-up information of four active spar candidates

	# 1	# 2	# 3	# 4
1) Active region	E-Glass 0° E-Glass +45° AFC −45° E-Glass 0°	E-Glass 0° AFC +45° E-Glass −45° E-Glass +45° AFC −45° E-Glass 0°	E-Glass 0° E-Glass +45° E-Glass −45° AFC −45° E-Glass +45° AFC +45° E-Glass −45° E-Glass 0°	E-Glass 0° AFC +45° E-Glass −45° AFC −45° E-Glass +45° AFC +45° E-Glass −45° AFC −45° E-Glass +45°
2) Nose, Web	E-Glass $[0°]_3$	E-Glass $[0°]_3$	E-Glass $[0°]_5$	E-Glass $[0°]_5$
3) Fairing	E-Glass [0°]	E-Glass [0°]	E-Glass [0°]	E-Glass [0°]

The analysis results of the four active spar candidates are summarized on Table 6.2. As mentioned in the previous chapters, ballast weights are added adequately in order to give the required Lock number, γ, and the center of gravity locations. Among the results, the twist actuation performance in both static and dynamic con-

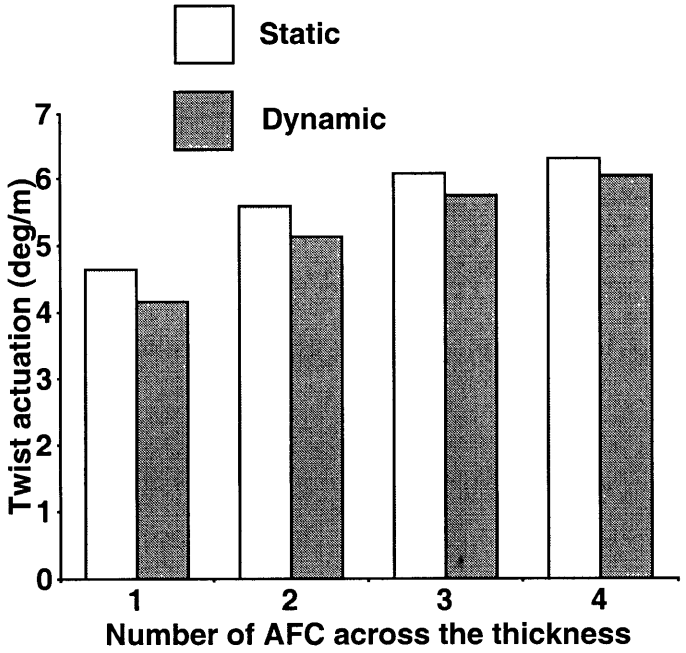


Figure 6-3: Twist actuation trend for the active spar ATR candidates with respect to the number of AFC packs embedded across the thickness

ditions are shown in Fig. 6-3. This plot shows a trend of actuation performance saturation at a certain point with the increase of AFC plies. This saturation happens once the addition of AFC plies increases the torsional stiffness of the blade, K_{22}, at the same rate as it increases the twisting actuation moment, $M_1^{(a)}$.

The analysis results of the active spar candidate No. 2 are compared with the values of the baseline passive rotor blade and design requirements on Table 6.3. Candidate No. 2 appears as one of the potential candidates which can be selected as a final design since it satisfies the requirements with a relatively small quantity of AFC packs (that directly impacts the cost of the blade). Furthermore, candidate No. 2 has an even number of AFC plies on top and bottom surfaces so that it can generate a symmetric twist actuation, a desirable feature when superimposing to the helicopter blade pitch angle variation.

Table 6.2: Analysis results of four active spar candidates ([1] cantilevered boundary condition at root)

	# 1	# 2	# 3	# 4
Mass per unit span (kg/m)	0.691	0.699	0.698	0.696
x_{CG}/c	24.9%	24.4%	24.6%	24.3%
x_{TA}/c	25.2%	24.2%	24.0%	23.9%
x_{EA}/c	25.5%	24.5%	24.3%	24.2%
EA (N)	$9.86\ 10^6$	$8.76\ 10^6$	$7.45\ 10^6$	$6.26\ 10^6$
GJ (N-m^2)	$1.49\ 10^1$	$1.98\ 10^1$	$2.87\ 10^1$	$3.71\ 10^1$
EI_{flap} (N-m^2)	$2.34\ 10^1$	$3.16\ 10^1$	$3.93\ 10^1$	$4.25\ 10^1$
EI_{lag} (N-m^2)	$5.58\ 10^3$	$4.90\ 10^3$	$4.07\ 10^3$	$3.40\ 10^3$
Lock No.	4.58	4.52	4.53	4.55
Section torsional inertia (kg-m^2/m)	$4.03\ 10^{-4}$	$3.79\ 10^{-4}$	$3.48\ 10^{-4}$	$3.23\ 10^{-4}$
1st flap bending frequency[1] @ 687.5 RPM	1.19/rev	1.19/rev	1.19/rev	1.19/rev
1st lead-lag bending frequency[1] @ 687.5 RPM	1.95/rev	1.91/rev	1.87/rev	1.83/rev
1st torsion frequency @ 687.5 RPM	4.35/rev	5.07/rev	6.29/rev	7.28/rev
Twist actuation @ 0 RPM (peak-to-peak, deg/m)	4.64°	5.58°	6.08°	6.31°
Twist actuation @ 687.5 RPM (peak-to-peak, deg/m)	4.17°	5.15°	5.76°	6.04°

Table 6.3: Comparison of candidate No. 2 against requirement

	Candidate # 2	Requirement/ baseline	% Difference
Mass per unit span (kg/m)	0.699	0.696	+0.45
x_{CG}/c	24.4%	25%	−2.4
x_{TA}/c	24.2%	25%	−3.2
x_{EA}/c	24.5%	25%	−2.0
EA (N)	$8.76\ 10^6$	$2.00\ 10^6$	+338
GJ (N-m^2)	$1.98\ 10^1$	$4.85\ 10^1$	−59.2
EI_{flap} (N-m^2)	$3.16\ 10^1$	$4.33\ 10^1$	−26.9
EI_{lag} (N-m^2)	$4.90\ 10^3$	$7.03\ 10^3$	−30.2
Lock No.	4.52	4.55	−0.66
Section torsional inertia (kg-m^2/m)	$3.7870\ 10^{-4}$	$3.1739\ 10^{-4}$	+19.31
1st flap bending frequency @ 687.5 RPM	1.19/rev	1.19/rev	0
1st lead-lag bending frequency @ 687.5 RPM	1.91/rev	1.57/rev	+21.65
1st torsion frequency @ 687.5 RPM	5.07/rev	7.37/rev	−31.21
Twist actuation @ 0 RPM (peak-to-peak, deg/m)	5.58°	4°	+39.5
Twist actuation @ 687.5 RPM (peak-to-peak, deg/m)	5.15°	4°	+28.75

6.2.2 Variations of the active spar candidates

New candidates are additionally considered at this point, and these are all based on the active spar candidates which has AFC plies concentrated within the front spar. The lay-up information of these new candidates are presented on Table 6.4.

One of the changes is the usage of fabric layers of E-glass instead of uni-directional ones. Therefore, the E-glass plies from the previous lay-up on Table 6.1 are changed as follows: $0°$ is changed to $0°/+90°$, and $+45°$ to $+45°/-45°$. This change has the advantage that one fabric layer will substitute two uni-directional layers. Only previous candidates No. 2 and No. 4 are considered here because they provide symmetric twist actuation.

A new candidate is formed by a combination of two previous ones, that is, candidates No. 2 and No. 3. This concept is established from the necessity of reinforcing the inboard side of the blade due to a larger centrifugal loading at the inboard. Therefore, the lay-up of the active spar candidate No. 3, which has more skin plies than those of No. 2, is used from Blade Station 22% radius to BS 44% radius, and those of No. 2 is used from BS 44% radius to BS 100% radius. This one is called '*reinforced candidate.*'

Another new concept is considered, which has two layers of active fibers in a single pack. For this reason, it is called '*candidate with doubled AFC.*' Since this concept of AFC ply has not been implemented in practice yet, only the theoretical performance improvement will be sought and compared with the other candidates in this study.

The analysis results of these variations are summarized on Table 6.5. On this table, only the static twist actuation performance, the first torsional natural frequency at the normal rotating speed, and the maximum strains existing at the worst loading condition are displayed because the other design parameters are already satisfied. The candidate No. 2 is still one of the finest candidates even though it shows relatively high strains under the worst loading condition.

According to the experimental testing of AFC fibers [11], the static strength of the bare AFC fiber and some reinforced forms are as appeared on Table 6.6, which

are only tensile strength results. However, static and spin testing of a small-scaled active rotor blade [28] revealed another data set for the static strength of AFC fibers as also included on Table 6.6. The latter set of the static strength data is selected as the reference in the current design process because the degree of AFC reinforcement in the ATR blade is similar to that. According to the criterion just selected, all the candidates on Table 6.5 satisfy the static strength requirements.

6.3 Analysis of the Active Fairing Candidates

It could be advantageous to add active material also to the fairing region in terms of twist actuation performance and structural integrity. Therefore, three new candidates are created using this concept and categorized as '*active fairing candidates.*' The lay-up information of these candidates are described on Table 6.7.

The analysis results of the active fairing candidates are presented on Table 6.8. As one can see, the twist actuation performance is obviously improved while restraining the first torsional frequency from significant increase. This is because the added AFC material at the fairing section increases the section torsional inertia as well as the torsional stiffness. Moreover, the maximum strains at the worst loading condition are a little smaller than those of the active spar candidates.

Despite the improved performance, the active fairing candidates have a common disadvantage that the center of gravity and the tension axis are located rearward, far more than the desirable 25% chordwise position. In fact, those points are located as far as near 50% chordwise positions for the proposed candidates. Center of gravity is not even able to be adjusted forward by adding or deleting the ballast weights in the present case. Moreover, the degree of twist actuation performance improvement is not significant compared with the quantity of the added AFC material. Since the cost of the system is drastically driven by the number of AFCs, the active fairing candidates were discarded in favor of the active spar ones for the application under consideration.

Table 6.4: Lay-up information of the variations of active spar candidates

	Candidate # 2	Candidate # 4
1) Active region	E-Glass 0°/+90° AFC +45° E-Glass +45°/−45° AFC −45° E-Glass 0°/+90°	E-Glass 0°/+90° AFC +45° E-Glass +45°/−45° AFC −45° E-Glass +45°/−45° AFC +45° E-Glass +45°/−45° AFC −45° E-Glass 0°/+90°
2) Nose, Web	E-Glass $[0°/+90°]_3$	E-Glass $[0°/+90°]_3$
3) Fairing	E-Glass [0°/+90°]	E-Glass [0°/+90°]
	Reinforced candidate (3-AFC + 2-AFC)	Candidate with doubled AFC
1) Active region	(22% – 44% R) E-Glass 0°/+90° AFC +45° E-Glass +45°/−45° AFC −45° E-Glass +45°/−45° AFC +45° E-Glass 0°/+90° (44% – 100% R) same as # 2	E-Glass 0°/+90° AFC +45° AFC +45° E-Glass +45°/−45° AFC −45° AFC −45° E-Glass 0°/+90°
2) Nose, Web	E-Glass $[0°/+90°]_3$	E-Glass $[0°/+90°]_3$
3) Fairing	E-Glass [0°/+90°]	E-Glass [0°/+90°]

Table 6.5: Analysis results of the variations of active spar candidates

	Candidate # 2	Candidate # 4	Reinforced candidate (3-AFC+ 2-AFC)	Candidate with doubled AFC
Twist actuation @ 0 RPM (peak-to-peak, deg/m)	4.86°	5.16°	4.89°	6.27°
1st torsion frequency @ 687.5 RPM	6.67/rev	5.16/rev	4.89/rev	6.27/rev
Maximum strain at the worst loading condition (Microstrain)	@ AFC	@ AFC	@ AFC	@ AFC
(1) Fiber direction	3,400	2,170	2,620	2,480
(2) Transverse direction	3,400	2,170	2,620	2,480
(3) Shear direction	6,470	4,170	5,130	4,760

Table 6.6: Ultimate strength data of AFC material

	Configuration	Mean Failure Strain
Ultimate tensile strength data from [10]	Baseline	1,250 μstrain
	Glass-reinforced Laminate	15,100 μstrain
		18,500 μstrain
	Direction	Static Failure Strain
Static Strength data from [28]	Fiber direction (tension)	4,000 μstrain
	Fiber direction (compression)	-3,000 μstrain
	Transverse direction	5,500 μstrain
	Shear direction	5,500 μstrain

Table 6.7: Lay-up information of the active fairing candidates

	Candidate # 2 + 1 AFC layer at fairing	Candidate # 2 + 2 AFC layers at fairing	Variation from # 2 + 2 AFC layers at fairing
1) Active region (D-spar)	E-Glass 0°/+90° AFC +45° E-Glass +45°/−45° AFC −45° E-Glass 0°/+90°	E-Glass 0°/+90° AFC +45° E-Glass +45°/−45° AFC −45° E-Glass 0°/+90°	E-Glass 0°/+90° AFC +45° E-Glass +45°/−45° AFC −45° E-Glass 0°/+90°
2) Active region (Fairing)	E-Glass 0°/+90° AFC +45° E-Glass +45°/−45°	E-Glass 0°/+90° AFC +45° E-Glass +45°/−45° AFC −45° E-Glass 0°/+90°	E-Glass 0°/+90° AFC +45° E-Glass +45°/−45° AFC −45° E-Glass 0°/+90°
3) Nose	E-Glass 0°/+90° E-Glass 0°/+90° E-Glass 0°/+90°	E-Glass 0°/+90° E-Glass 0°/+90° E-Glass 0°/+90°	E-Glass 0°/+90° E-Glass +45°/−45° E-Glass 0°/+90° E-Glass +45°/−45° E-Glass 0°/+90°
4) Web	same as nose	same as nose	E-Glass 0°/+90° E-Glass 0°/+90°
5) Trailing edge region	E-Glass 0°/+90°	E-Glass 0°/+90°	same as nose

Table 6.8: Analysis results of the active fairing candidates

	Candidate # 2 + 1 AFC layer at fairing	Candidate # 2 + 2 AFC layers at fairing	Variation from # 2 + 2 AFC layers at fairing
Twist actuation @ 0 RPM (peak-to-peak, deg/m)	5.45°	5.57°	6.4°
1st torsion frequency @ 687.5 RPM	6.27/rev	5.80/rev	6.32/rev
Maximum strain at the worst loading condition (Microstrain)	@ AFC	@ AFC	@ AFC
(1) Fiber direction	3,220	3,170	2,670
(2) Transverse direction	3,220	3,170	2,670
(3) Shear direction	6,180	6,040	5,080

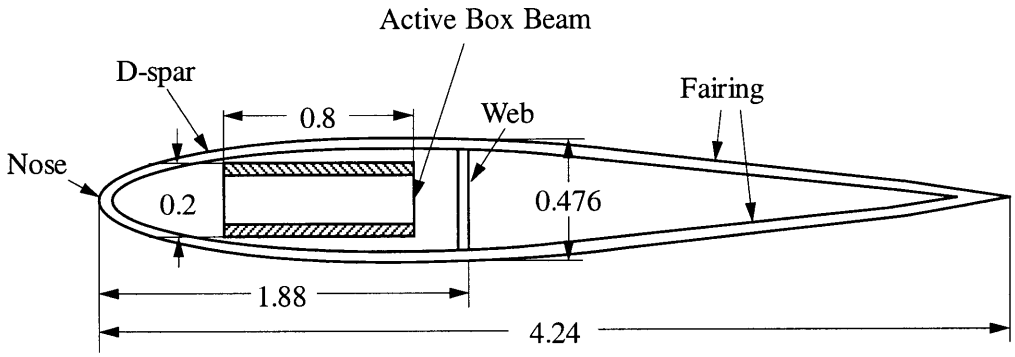


Figure 6-4: Schematic diagram of the active box beam candidate (all dimensions are in inches).

6.4 Analysis of the Active Box Beam Candidates

The final concept to be considered in this design study is the one which has the additional box beam structure with AFC plies on it. Detailed schematic diagram of this candidate is shown in Fig. 6-4. The shape and dimension of the active box beam here is determined through the trend study in order to give the maximum twisting actuation moment. As a result, the AFC plies can only be applied on the top and bottom walls of the box beam since the side walls are too narrow. However, it turns out that the lay-up of the side walls affects the twisting actuation moment considerably.

Since the outer airfoil skin structure contains no active material, the twisting actuation moment should be transferred from the inner box beam to the outer passive structure by some fixture. Four candidates are created following this concept, and the detailed lay-up information of them is given on Table 6.9.

The analysis of the active box beam candidates is not so straightforward as the previous ones because of the transferring mechanism of twisting actuation moment. The analysis is completed only by using a full three-dimensional finite element modeling including the transferring medium with active material capability, which has not been implemented in literature yet. Therefore, in this design process, the model developed in Chapter 2 is still adopted with the assumption that the actuation moment will be transferred to the outer skin structure completely without changing any component of the stiffness matrix. That means, the stiffness of the two structures - inner

Table 6.9: Lay-up information of the active box beam candidates

	2 AFC layers at Box Beam + 1 E-Glass at Airfoil skin	3 AFC layers at Box Beam + 1 E-Glass at Airfoil skin
1) Box Beam - Upper & lower walls	AFC +45° E-Glass +45°/−45° AFC −45°	AFC +45° E-Glass +45°/−45° AFC −45° E-Glass +45°/−45° AFC +45°
- Side walls	E-Glass 0°/+90° E-Glass 0°/+90° E-Glass 0°/+90°	E-Glass 0°/+90° E-Glass 0°/+90° E-Glass 0°/+90°
2) Outer Airfoil skin - D-spar, nose	E-Glass 0°/+90°	E-Glass 0°/+90°
- Web, fairing	E-Glass 0°/+90°	E-Glass 0°/+90°
	2 AFC layers at Box Beam + 2 E-Glass at Airfoil skin	3 AFC layers at Box Beam + 2 E-Glass at Airfoil skin
1) Box Beam - Upper & lower walls	AFC +45° E-Glass +45°/−45° AFC −45°	AFC +45° E-Glass +45°/−45° AFC −45° E-Glass +45°/−45° AFC +45°
- Side walls	E-Glass 0°/+90° E-Glass 0°/+90° E-Glass 0°/+90°	E-Glass 0°/+90° E-Glass 0°/+90° E-Glass 0°/+90°
2) Outer Airfoil skin - D-spar, nose	E-Glass 0°/+90° E-Glass 0°/+90°	E-Glass 0°/+90° E-Glass 0°/+90°
- Web, fairing	E-Glass 0°/+90°	E-Glass 0°/+90°

box and outer airfoil skin structure - will be calculated separately and then combined to give the stiffness of the whole structure. Regarding the actuation constants, only the inner box beam will be analyzed. This approach is simple and the analysis can be performed within the present framework. The fundamental question remains on how to fabricate such a perfect transferring medium. Using this approach, the analysis results of the active box beam candidates are shown on Table 6.10.

The twist actuation performance shows significant increase compared with the previous candidates, while holding the first torsional natural frequency at a relatively low range. Also, the maximum strain level at both AFC and passive plies under the worst loading condition shows acceptable values.

The active box beam candidate has an obvious advantage that it requires a smaller quantity of active material than the previous candidates in order to obtain the same degree of twist actuation. There is also a possibility that the active box beam can be repaired and re-inserted within the spar in case of electric breakdown of the AFC packs. However, in order to obtain all the advantages listed above, a special moment transfer mechanism or attachment must be included, which makes the structure quite complicated and result in manufacturing difficulties. It requires further refined analysis of the moment transfer mechanism, which certainly affects the torsional stiffness and the actuation moment. This evidently results in a twist actuation loss. Because of these uncertainties and complexities, the active box beam candidates were discarded by now.

Table 6.10: Analysis results of the active box beam candidates

	2 AFC layers at Box Beam + 1 E-Glass at Airfoil skin	3 AFC layers at Box Beam + 1 E-Glass at Airfoil skin
Twist actuation @ 0 RPM (peak-to-peak, deg/m)	5.9°	6.1°
1st torsion frequency @ 687.5 RPM	4.92/rev	5.73/rev
Maximum strain at the worst loading cond. (Microstrain)		
- at box beam (AFC)		
(1) Fiber direction	4,300	2,890
(2) Transverse dir.	4,300	2,890
(3) Shear direction	8,200	5,430
- at outer airfoil skin (E-Glass)		
(1) Fiber direction	9,900	7,200
(2) Shear direction	950	880

	2 AFC layers at Box Beam + 2 E-Glass at Airfoil skin	3 AFC layers at Box Beam + 2 E-Glass at Airfoil skin
Twist actuation @ 0 RPM (peak-to-peak, deg/m)	4.7°	5.0°
1st torsion frequency @ 687.5 RPM	5.38/rev	6.08/rev
Maximum strain at the worst loading cond. (Microstrain)		
- at box beam (AFC)		
(1) Fiber direction	3,340	2,360
(2) Transverse dir.	3,340	2,360
(3) Shear direction	6,300	4,370
- at outer airfoil skin (E-Glass)		
(1) Fiber direction	7,600	5,830
(2) Shear direction	860	690

6.5 Selection of the Final Design and Improvement

Considering both the analysis results of the previous candidates introduced on Tables 6.1, 6.4, 6.7, 6.9, and the cost effectiveness of the active material usage, the active spar candidate No. 2 is selected as the final design for the ATR blade. One of the reasons to reach the selection is the simplicity of the active spar candidate No. 2 which makes it easy to manufacture, and the fact that it satisfies the design requirements with relatively small quantity of active material.

In order to make it even easier for manufacturing, some design modification has been added. The first one is a lapping of the front spar section and the aft fairing section, since those two parts are to be fabricated separately in the manufacturing sequence. Therefore, a new region is required at the joint of the three regions, i.e., front spar, fairing, and web; all the plies from the three regions are to be overlapped to make a strong lap. In the schematic diagram of the modification result (Fig. 6-5), the new region is denoted as '*Wrap Joint Region*'.

Also, in the '*Nose*' region, one ply of S-Glass is inserted to compensate the considerable thickness difference between '*Nose*' and '*Active Region*'. To counteract the stiffness increase from the S-Glass insertion, one ply of E-Glass is removed of the '*Web*' region. The final result of this modification is illustrated in Fig. 6-5, where the size and locations of two ballast weights are also displayed.

The analysis result of the final selected design is presented on Table 6.11, along with the original design requirements or baseline values. As one can see, the final design satisfies all the requirements. Particularly, the level of actuation shows a margin of 0.52 deg/m above the requirement. The maximum strain shows an acceptable level compared with the reference values on Table 6.6.

Table 6.11: Result of the final design compared with requirements

	Final design	Requirement/ baseline	% Difference
Mass per unit span (kg/m)	0.6960	0.6959	+0.01
x_{CG}/c	24.9 %	25 %	−0.4
x_{TA}/c	30.8 %	25 %	+23.2
EA (N)	$1.637\ 10^6$	$2.0\ 10^6$	−18.2
GJ (N-m^2)	$3.622\ 10^1$	$4.8468\ 10^1$	−25.3
EI_{flap} (N-m^2)	$4.023\ 10^1$	$4.3306\ 10^1$	−7.1
EI_{lag} (N-m^2)	$1.094\ 10^3$	$7.0264\ 10^3$	−84.4
Lock No.	4.55	4.55	0.
Section torsional inertia (kg-m^2/m)	$3.307\ 10^{-4}$	$3.1739\ 10^{-4}$	+4.2
1st torsion frequency @ 687.5 RPM	7.38/rev	7.37/rev	−0.1
Twist actuation @ 0 RPM (peak-to-peak, deg/m)	4.52°	4°	+13.0
Maximum strain at the worst loading condition (Microstrain)	@ AFC		
(1) Fiber direction	2,730		
(2) Transverse direction	2,730		
(3) Shear direction	5,170		

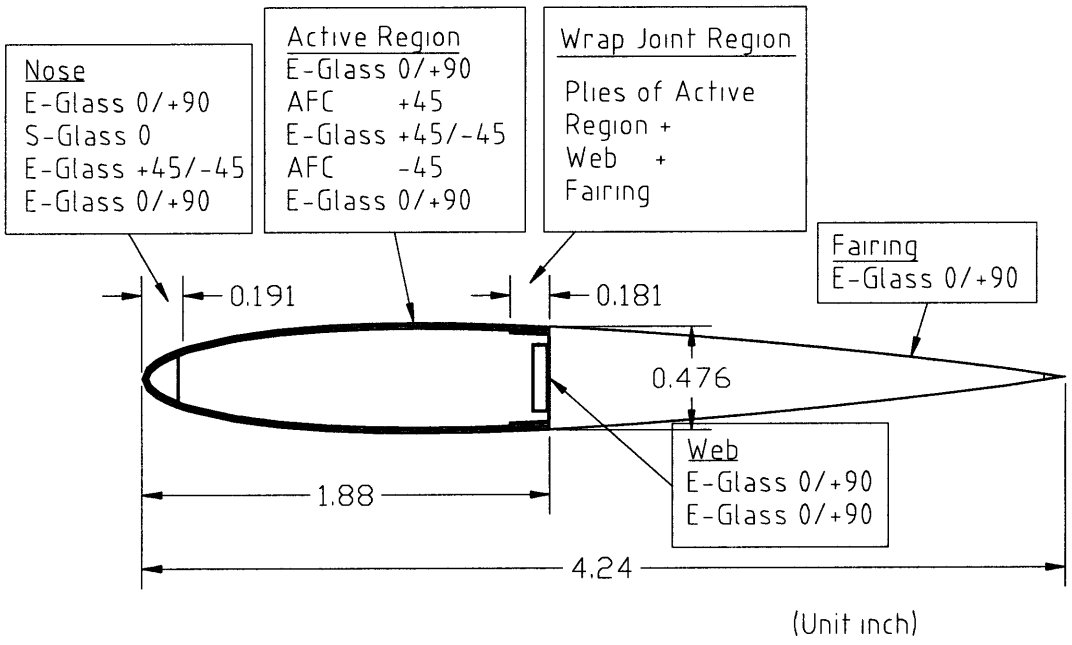


Figure 6-5: Schematic diagram of the final selected design

Chapter 7

ATR Prototype Blade Manufacturing

7.1 Overview

The prototype blade was manufactured according to the final design described in Chapter 6. The aluminum blade mold used for the original baseline blade manufacturing was used again for this prototype. Besides the details described in Chapter 6, there are some additional miscellaneous elements which need to be designed or modified from the original baseline blade. Therefore, such activities are addressed in detail first in this chapter.

7.2 Miscellaneous Items

7.2.1 Integral blade root

Among the different elements that needed special attention during this phase, one of special importance is the blade root, which is totally modified from the original metal block attachment of the baseline blade. The concept adopted for this blade uses an integral graphite/epoxy construction in the exact external airfoil shape, with a small Rohacell foam core inserted between the graphite stacks to provide the back pressure

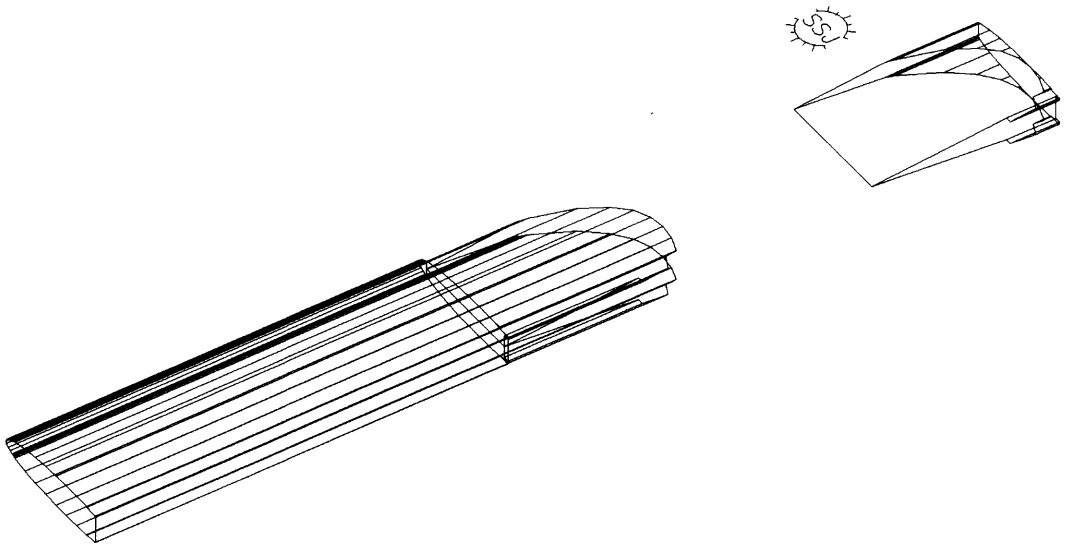


Figure 7-1: Drawing of 3-dimensional blade root stack

during cure. A total of 80 plies of IM7 unidirectional graphite/epoxy were cut and laid-up to form the $[0°, +45°, -45°, 90°]_{10}$ symmetric laminate stack about the foam core. This is chosen in order to provide enough strength for tensile, bending and torsional loads. Also, for continuity of the outboard lay-up, the root stack is wrapped around by the continuous skin E-Glass plies of the outboard constant cross-section. Fig. 7-1 shows the design of 80-ply graphite stack in 3-dimensional airfoil shape, and an inboard wedge-shaped part of the spar core which is merged with the root stack. Fig. 7-2 shows the graphite part of the root prior to cure. Finally, three bolts in tandem do the mounting of the blade root with the hub attachment. The corresponding holes that go through the root block are drilled using a diamond drill bit after the root stack is cured.

7.2.2 AFC packs

Regarding the AFC packs used for this prototype blade, similar design and manufacturing procedures adopted for the Boeing/MIT CH-47D integral actuated blade [28] were used. The new blade geometry, however, required new pack dimensions and minor modifications on the gap between the AFC packs and the location of the solder flaps. The final geometry of the AFC packs is presented in Fig. 7-3. The

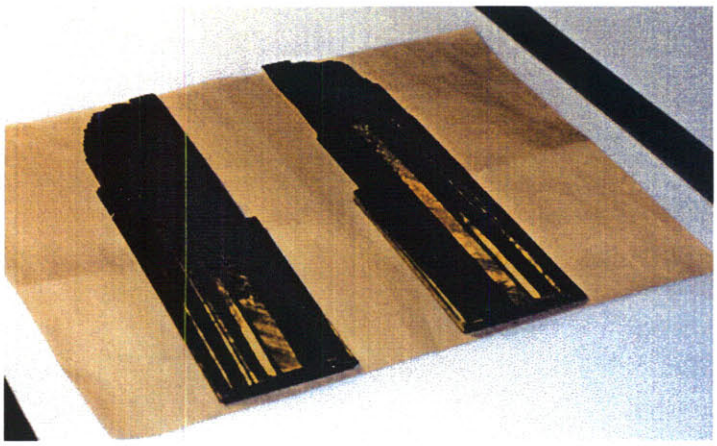


Figure 7-2: Detail of the blade root construction

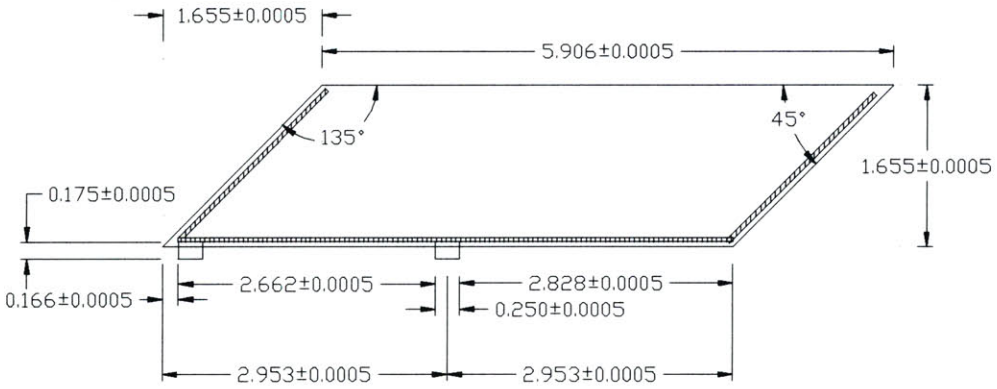


Figure 7-3: Final AFC pack design used in the ATR prototype blade

manufacturing of all 24 individual AFC packs were performed by Continuum Control Corp., Cambridge, Massachusetts, according to the specifications. Before using the packs on the composite construction, each of them were individually tested and their actuation and capacitance characterized at two different cycles: 3,000 V_{pp}/600 V_{DC} ("representative cycle") and 4,000 V_{pp}/1,200 V_{DC} ("extended cycle") for 1 and 10 Hz. The average free strain for the extended cycle was 1278 μstrain with a standard deviation of 228 μstrain. Fig. 7-4 shows the process of inserting the first layer of the AFC packs (composed of 6 packs) at the top surface during the prototype manufacturing.

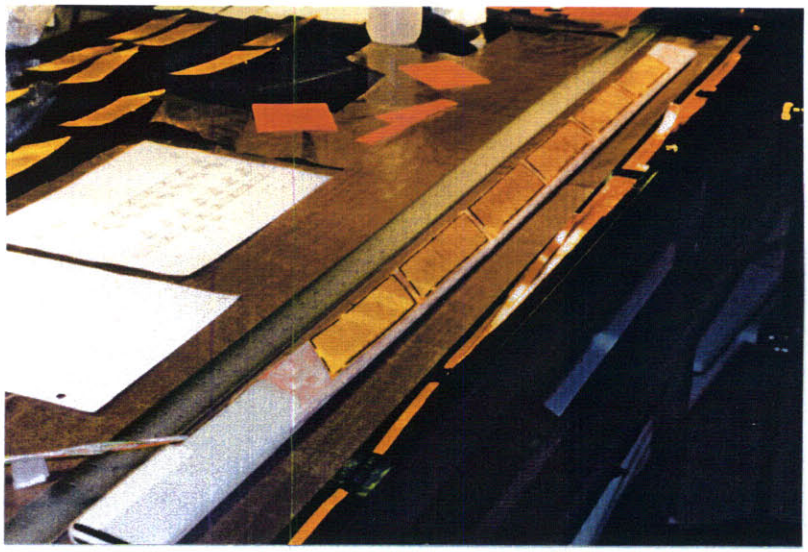


Figure 7-4: AFC packs being inserted during the prototype manufacturing

7.2.3 Flexible circuit

To get the high voltage into the packs, a flexible circuit is inserted in the blade assembly and runs along the blade web. A total of six plies of such circuits were designed, each of which has 8 copper leads inside a kapton insulation. In order to avoid the electrical shorting between the copper lines when they are delivering high voltage, the gap between the lines are maximized. In this particular case, the gap is designed to be 15 mil (instead of 10 mil in the flexible circuit used in the CH-47D active blade [28]). The six circuit plies are not bonded initially together in order to avoid damage due to an extreme bending curvature near the blade root when the lay-up assembly is inserted inside the blade mold for the fairing cure.

All Flex Inc., Northfield, Minnesota manufactured the flexible circuits according to the specifications. They were successfully tested for high voltage isolation prior to the blade construction. Once the flex circuits are in place, their square-solder pads are soldered to the flaps (connectors) on the AFC packs, and each individual circuit layer is attached together and to the web using film adhesive cured at 250°F. Detailed drawing of the flexible circuit is shown in Appendix D, where the location of each solder pad is also provided.

7.2.4 Foam cores and ballast weights

Finally, the fabrication of the Rohacell foam core inserts and the tantalum ballast weights for the leading edge and web are described. The Rohacell foam blocks were machined at NASA Langley's Advanced Machining Development Laboratory to the desired airfoil section, with an extra 10-15 mil oversize to ensure the right back compression of the laminate against the mold walls during cure. The foam blocks for the fairing were hand cut and sanded using belt sander and a metal template tool. These foam blocks are then dried in the oven at 250°F for 90 minutes in order to eliminate any humidity trapped in the bulk foam material. All the foam pieces are 5.5-inches long in the spanwise direction, and they are bonded to each other using 5-min. epoxy. Even though the foam cores have initially straight shape with no twist along the span, the pretwist existing in the blade mold deforms the lay-up assembly and the foam cores into the desired twisted shape.

The ballast weights were also fabricated at NASA Langley. The leading edge weights were machined to the desired shape, and the web ones were cut as small plate-like pieces. They are all chopped into 1-inch long pieces before placed into the leading edge and web regions in order to minimize the increase on the blade stiffness. For a strong structural bond between the chopped tantalum pieces and the lay-up assembly, film adhesive is used to wrap the leading edge tantalum weights before they are inserted in the spar assembly. For the web weights, it was not possible to wrap them due to insufficient room near the web, and they were added directly to the foam core.

Drawings of the foam cores and the ballast weights designed according to the above considerations are shown in Appendix D.

7.3 Testing Articles

Two testing articles were constructed prior to the final active prototype blade: a 1/3-span blade spar and a half-span blade spar (non-working AFC packs were used). Both were built with an aluminum attachment at the tip for gripping at the tensile

testing machine. The first one was used primarily to debug the manufacturing process, including mold handling and usage, vacuum bagging of the mold, and autoclave curing cycle (250°F, 90 min., 50 psi of external pressure, and -25 psi of vacuum pressure were also used to support the final closing of the mold), sliding of AFC packs in the prepreg laminate, the survivability of the AFC contact flaps through the curing cycle, the root construction, the Rohacell foam sizing and placement, and the attachment of strain gages on those foam pieces. It was found that the thickness of airfoil shape in the blade mold is larger around the root section than that of the constant section by observing insufficient back pressure imposed on root section. Therefore, thicker foam cores were designed for that section, and a foam core plate was inserted between the two 40-ply blade root stacks to compensate for such difference.

The second testing blade was used primarily for testing the root strength and implementing modifications needed to the process identified from the first attempt. The improved manufacturing technique details used on the second blade checked all the steps to be followed on the full active blade. After the tensile test, the second spar assembly was sliced to see any delamination of the plies or any voids trapped inside the assembly near the strain gages, and none were found. Also the weight of the spars was measured and compared with the target weight per unit length. Similarly, experiments were conducted to assess the spar torsional stiffness. Finally the fairing assembly of the same span length was attached and cured to the second spar successfully.

The listing of the activities for the ATR blade manufacturing are summarized in Appendix E, which were fundamentally based on the experiences acquired in building those two testing articles.

7.4 Prototype blade

Now that the whole manufacturing process is well established, the fabrication of the ATR prototype blade followed.

First, the Rohacell foam core pieces were checked for the dimensions, and then went through the drying procedure. Seven pieces of both front and rear foam cores were bonded together to give enough span length. Extra span length was trimmed after the manufacturing process was completed and torsional stiffness measurements were done. The extra length is required at the blade tip to install a grip to apply the tip torque.

Before starting the wrapping of the prepreg plies around the foam, sensors need to be properly installed and tested. A total of 10 sets of full-bridge strain gauge sensors are embedded into the foam core surface and the wires run through a small trough in the foam along the web. Such a small trough was fabricated with a 1/4-in-diameter ball mill at the web side of the foam below a bigger trough which accommodates the web tantalum weights. Fig. 7-5 shows the arrangement of some strain gauge bridges and the connecting signal wires running along the surface of the foam cores. The wires are structurally bonded to the front spar foam core using the Epon-9309 epoxy.

The 10 bridges are divided in six torsional strain gauges, three flap-bending strain gauges, all located at different spanwise stations, and one chordwise-bending strain gauge near the blade root. Detailed drawing with the location of theses 10 strain gauge bridges is shown in Appendix D. In order to guarantee that all the sensors work well after blade manufacturing, the resistances of each strain gauge bridge were checked at each step and recorded. These strain gauges will be used to monitor the deformation and load level during spinning on the hover stand and in the wind tunnel. They are also helpful for monitoring individual pack actuation during bench tests.

The manufacturing of the spar assembly is conducted next. The two types of tantalum weight pieces are aligned and attached at the nose and rear web to give the desirable chordwise CG location and weight distribution. One layer of film adhesive is used to wrap the front spar foam core and keep the alignment of the tantalum

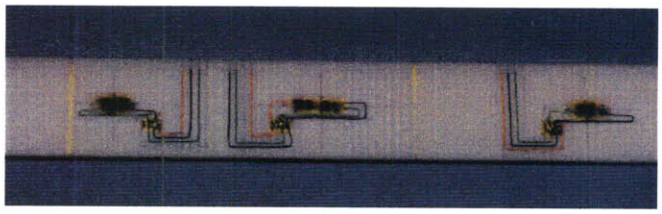


Figure 7-5: Strain gauges attached upon the foam cores

weights before putting the skin plies. At the blade root, two stacks of 40 graphite plies each are inserted at top and bottom of the foam stab. Now, the E-Glass skin plies and active layers comprising of six AFC packs are inserted orderly one by one. The exact location of the six AFC packs of each active layer is defined in association with other elements, particularly the flexible circuit, and is shown in Appendix D.

The E-Glass plies are cut long enough to cover from the blade root to tip so that it can wrap the root stack laminates. This conforms to the intention of 'integral' blade root design. Fig. 7-4 shows an intermediate stage during the manufacturing process that the innermost E-Glass ply was wrapped around the assembly of blade root and front spar foam core, followed by the first layer of AFC packs inserted on top of the E-Glass ply. The large gap between the AFC packs and the root region is filled with S-Glass plies (details are also shown in Appendix D), as well as small strips of S-Glass are used at the gaps between the AFC packs.

The blade mold is cleaned with Acetone and a thin film of mold release agent, Frekote 700-NC, is applied at least three times. To give an indentation necessary at the wrap joint region, a strip of 5 mil thick aluminum tape is attached at the right location of the top and bottom blade mold surfaces (see Fig. 7-6). Peel-ply strips of the same width are also attached on the spar assembly at the same position in order to give a rough surface which makes a stronger bond with the E-Glass ply for the fairing assembly.

The spar assembly is put inside the blade mold and sealed with vacuum tape so that some vacuum can be built in the mold when inside the autoclave. The whole assembly is put inside MIT Technology Laboratory for Advanced Composites' 3ft $\times$ 5ft autoclave and cured according to the cycle tested before. Once the spar is cured,

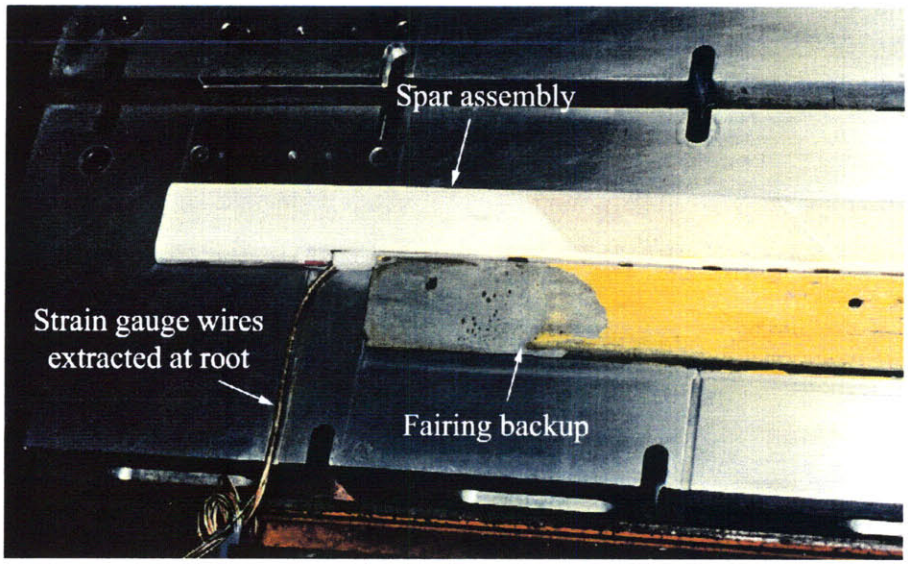


Figure 7-6: Blade mold in which the spar assembly is sitting with dummy fairing backup and strain gauge wires are extracted at root along the small trough

peel-ply strip is detached and the extra skin plies which extrude out of the exact shape are eliminated using a cutter and No. 600 sand paper. For the AFC pack soldering connection, extra resin which covers the flap surface of the packs is scrubbed out carefully under the microscope.

Next, the six flex circuit layers are soldered to the corresponding AFC flap connectors using high-temperature solder. At some locations, an auxiliary, tiny copper strip is used to compensate for the mismatch of both soldering spots. To ensure the soldering connection, the capacitance of each AFC pack was checked at the entry spot of the flexible circuit and recorded. (The record of each AFC pack's capacitance is included in Appendix C.) The layers are then bonded to each other and to the web using strips of film adhesive. Since the selected film adhesive was to be cured at 250°F, the spar plus the flexible circuit assembly was put in an oven for 90 minutes. Due to the mismatch of thermal expansion coefficients between the flex circuit (mostly composed of copper) and the composite spar assembly, an undesirable chordwise bending deflection resulted. Deflection at the tip was about 8mm to the rearward chordwise direction; however, such a small deflection should not significantly vary the structural and aerodynamic characteristics of the blade. The main problem with it was that the deflected spar would not fit into the blade mold any more for fairing cure. Therefore,

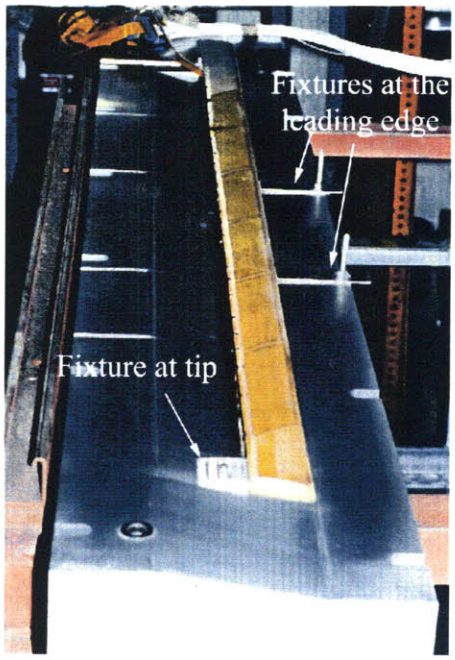


Figure 7-7: Prototype spar sitting inside the blade mold clamped with the fixtures at the leading edge and the tip

a few fixtures were used to hold the spar assembly in the straight blade mold while handling the fairing assembly for lay-up (see Fig. 7-7). The chordwise deflection was reduced to about half after the fairing was attached and cured to the spar.

Before the attachment of the fairing assembly to the prototype spar, a shorter fairing section was manufactured and attached to the second testing spar to clarify the manufacturing issues. It was found that the fairing foam cores were not thick enough. Therefore, new foam cores with oversize thickness of about 40–50 mil were fabricated using the template guide tool. Lay-up of skin plies and autoclave curing for fairing followed the same procedure as in the spar assembly.

After completing the fairing cure, the extra glass-epoxy coming out of the trailing edge was trimmed using the sand paper. The extra length at the tip of the blade was cut out using the diamond wheel after the torsional stiffness measurement was completed. The final shape of the ATR prototype can be seen in Fig. 7-8, and no major consequences are expected from the slight curvature present in the chordwise direction. The future wind tunnel blades will use a room temperature curing epoxy for the attachment of the flexible circuit layers to avoid this problem.

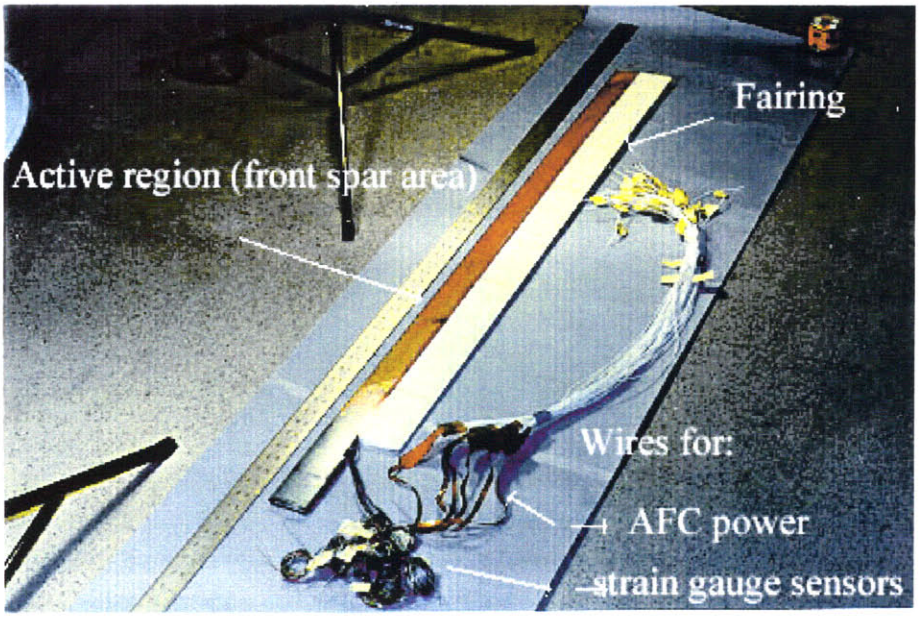


Figure 7-8: Final ATR prototype blade

7.5 Summary of Manufacturing Issues and Recommendations

During the testing articles and prototype blade manufacturing, a few problems appeared and most of them were fortunately solved during the process. However, few issues still remain to be solved for future ATR blade manufacturing. Here are the summary of such issues and the recommendations.

- Attachment of the flexible circuit to the spar assembly became a big issue. This caused the chordwise deflection, which made the subsequent process harder associated with fairing fabrication. As mentioned above, use of room temperature curing epoxy is recommended to avoid this problem.

- The length of the AFC flaps are sometimes insufficient to match with the solder pads of the flexible circuit. An auxiliary copper strip was used in such locations. It is recommended to have an extra length for the AFC flap, and that can be trimmed out later in case of being unnecessarily long.

- Wrapping the tantalum weights with 0° S-Glass was the original design, which

should help support the locally concentrated centrifugal loads induced by the tantalum weights. However, due to an insufficient space at the web location, the wrapping plan was abandoned during the prototype blade manufacturing. If any symptom of structural failure is found around this area by the non-destructive inspection after the spin test, it is necessary to revise the wrapping idea for future blade manufacturing.

Chapter 8

ATR Prototype Blade Testing

8.1 Overview

In what follows, different characterization tests were performed on the ATR prototype blade in order to validate the design and manufacturing procedures, and to verify the performance of the prototype article. Tests included:

- Tensile testing was conducted to verify if the designed structure can withstand the combined loading of the centrifugal load from rotation and the external aerodynamic load induced by forward flight condition. This test is especially critical to authenticate the integral blade root design.

- The torsional stiffness of the blade section - constant section which contains the active material - was measured and compared with the model predictions. This comparison tells the accuracy of the model analysis, and gives some perspective on variations of the twist actuation performance from model prediction.

- High voltage was applied to the AFC packs to induce the twist actuation, and the twist at the tip was measured under the static condition. Also it was compared with model prediction. Before the actuation test, all the packs were checked for their capacitance if the soldering connections still work well. The torsional strain gauges embedded inside the blade were monitored to see the actuated pack working.

- Frequency response of the prototype blade was acquired by monitoring either the strain gauge output or tip twist actuation when varying the sinusoidal high voltage excitation frequency. This provides dynamic characteristics of the blade in a transfer function.

8.2 Blade Root Test

As mentioned in the previous chapter, the second testing article spar was used for tensile testing of simulated centrifugal loads. This would primarily validate the root strength of the prototype blade. From the blade design phase, estimates of the laminate ply strains at critical sections were performed based on the final assembly (spar and fairing). Those estimates combine the centrifugal loads resulting from the rotation of the blade at maximum nominal speed (687.5 rpm) and the worst forward flight aerodynamic loading (coming from CAMRAD II). Based on this information, an equivalent tensile load is calculated in order to reproduce the worst case strain condition at the critical sections. Theoretical values based on maximum strain/first-ply failure criteria are calculated on the developed framework, and the results are presented in Table 8.1 for three critical blade section (BS) locations.

The half-span spar is assembled in the Instron machine so that the root is attached through three bolts to a metal assembly simulating the hub attachment, and the tip has a metal insert that is gripped directly to the moving head of the machine. Load was applied on increments of 100 lb (444.8 N) up to 1,000 lb, and then on increments of 50 lb up to catastrophic failure. The spar broke at the uniform active cross-section region, at the middle of a bank of AFC packs. The fractured region

Table 8.1: Tensile load test on 3/4-radius blade spar (blade station in inches)

Critical Section Location	**Tensile Load (N)**
BS 6.87 (root inboard end)	4,608
BS 12.5 (root transition region)	3,848
BS 15.0 (root outboard end)	3,234
Experimental Failure Load (< BS 15.0)	7,082

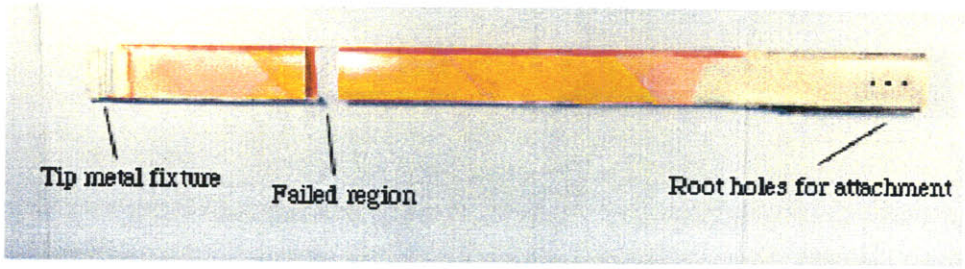


Figure 8-1: Testing article showing catastrophic failure under tensile loading

was nearly perpendicular to the applied tensile load direction (see Fig. 8-1). The measured maximum tensile load was 1592 lb (7,082 N), a factor of 1.54 higher than the worst case condition at the root and 1.47 higher than the worst design case condition for the active region. This result meets the NASA Langley Handbook wind tunnel model requirement of 1.25 factor of safety with respect to centrifugal loads for 110% overspeed [31].

8.3 Blade Torsional Stiffness Measurement

Since the blade torsional stiffness is an important parameter associated with the actuation authority of the blade, special attention is given to it. Tests were performed on the prototype blade before and after the fairing is attached. The tests were conducted on a specially built rig that applied a controlled couple at the tip of the blade, which stands vertically and is clamped at the root. A pair of laser sensors (Keyence LB-12, 2 μm resolution, 30-50 mm effective distance) was used to extract the rotation of a given station of the blade. Measurements were performed at different (active) stations at known radius separations, and at constant cross-sectional characteristics, for different levels of applied torque at the tip. Fig. 8-2 and 8-3 show the arrangement of the ATR prototype blade clamped at the test rig around the blade root, and a pair of laser sensors and a reflecting strip attached at the surface of the ATR blade, respectively. A summary of the results in presented in Fig. 8-4, where the predicted results based on the developed thin-walled cross-sectional analysis and the more generic finite-element based VABS [15] are shown. As one can see, there is a significant increase (over 17%) on the blade torsional stiffness with the addition of

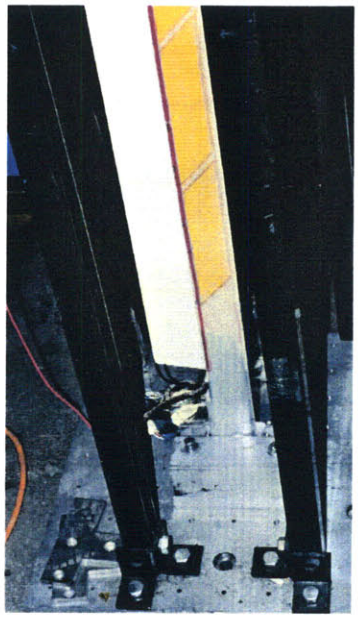


Figure 8-2: ATR prototype clamped at root with the rig

the fairing. There is a considerably good overall correlation considering that the experimental data has a spread of approximately ± 2 N-m^2 for the spar measurements and ± 4 N-m^2 for the complete blade (difficulties were found on the load attachment device at the tip of the blade). The thin-walled approximation developed in this study (Chapter 2) consistently under-predicts the torsional stiffness by 20%. Some of that is due to the model not accounting for the foam core, ballast weights, and the presence of the flexible circuit. The results of VABS based on a finite element discretization of the warping field and including the effects of the foam core, show better correlation with the experimental data [32].

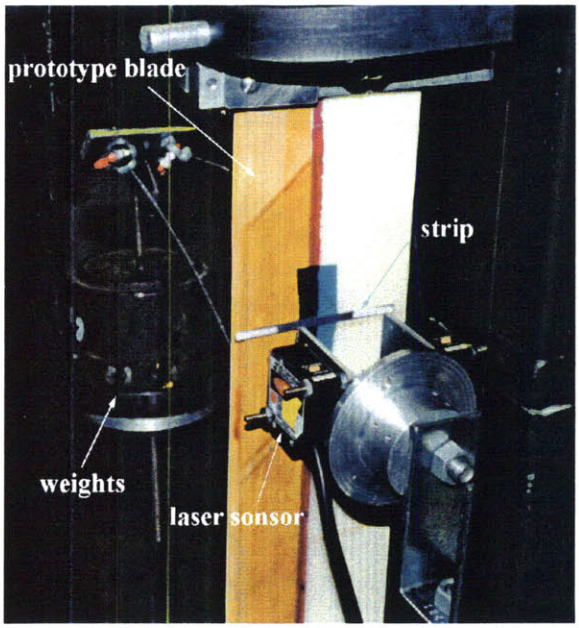


Figure 8-3: ATR prototype blade clamped at the testing rig with the laser sensors illuminating the reflecting strips (weights hung at the end of cables for torque the blade tip are also shown).

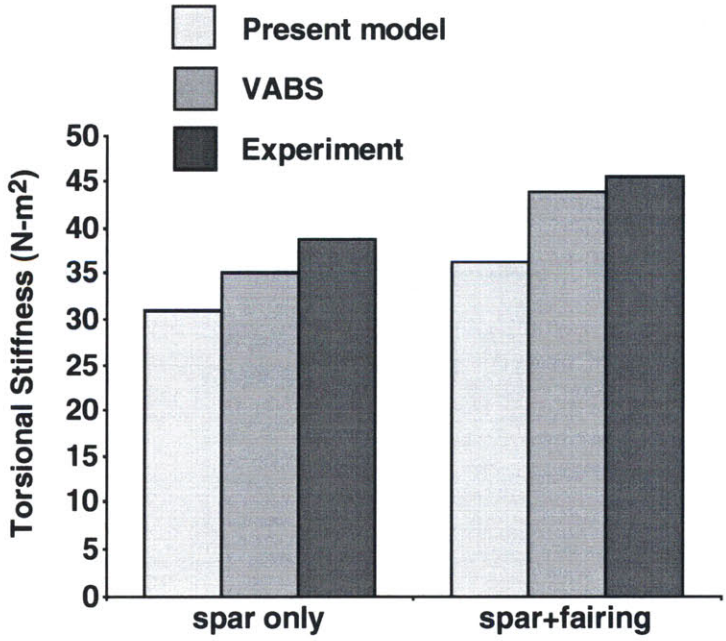


Figure 8-4: Torsional stiffness results for the spar and full blade - comparison between measurements and theoretical results

8.4 Bench Actuation Test

With the prototype blade mounted on the same rig as used for the stiffness measurements, electrical power was applied to the packs and a pair of laser sensors was used to measure the rotation angle at the tip of the blade. The amplifier used in these tests was a TREK 663A, ± 10 kV, 20 mA, 40 kHz limiting current and frequency, respectively. These tests were performed on the spar first, and then on the whole assembly (spar + fairing).

The voltage was varied on increments of 500 V_{pp}, and the signal frequency was 1 Hz and 10 Hz for each voltage level (higher frequency tests were not possible with the given amplifier due to the current limitation). For voltages above 2,000 V_{pp}, a DC offset is used to avoid depolarization of the piezoelectric fibers. For 4,000 V_{pp} the scheduled DC offset is 800 V. During tests, however, AFC packs started short-circuiting once the voltage amplitude crossed 1,500 V. A total of five AFC packs short-circuited during the spar tests, while trying to establish the 2,000 V_{pp}/800 V_{DC} (the very first attempt to raise the voltage from 2,000 V_{pp}/0 V_{DC} to the 3,000 V_{pp}/800 V_{DC} was responsible for the first loss. All others happened at the 1,500 V_{pp}/800 V_{DC} and 2,000 V_{pp}/800 V_{DC}).

The sequence of the AFC pack failure during the actuation test is described on Table 8.2 and a location diagram of each specific pack in the prototype blade is shown in Fig. 8-5. As one can see, four AFC packs out of the total five lost during the tests were located at the outermost layer of the bottom surface. However, the reason for such a locally concentrated breakdown of the AFC packs is not known yet, and no specific correlation among the failed packs was observed besides the voltage level. Similar problems were reported in another integral-twisted active blade [28], but all the attributed causes were eliminated from the present prototype blade. Further investigation on this issue is under way. Due to scheduled hover tests of this prototype blade, a decision was made to limit the maximum voltage applied at that point.

With 19 out of the original 24 AFC packs working, a summary of the voltage tests is presented in Fig. 8-6 for 1 Hz and 10 Hz excitation signals. As one can see

Table 8.2: Sequence and condition of AFC pack failure during the actuation test

Failing sequence	Pack No.	Condition
1	15	3,000 V_{pp}, 1 Hz, 600 V_{DC} offset
2	26	1,500 V_{pp}, 1 Hz, 800 V_{DC} offset
3	3, 9, 17	2,000 V_{pp}, 1 Hz, 800 V_{DC} offset

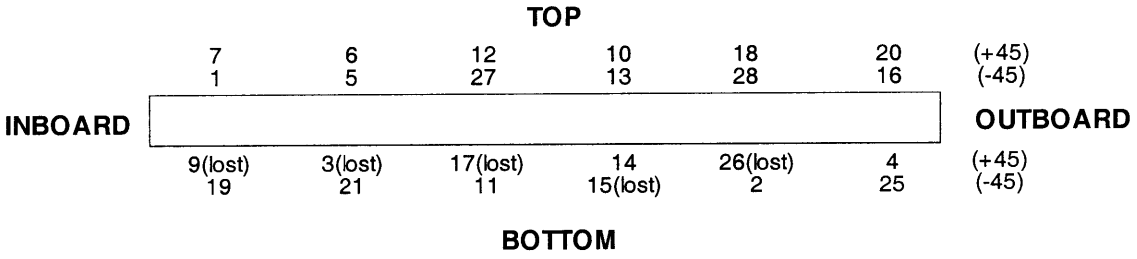


Figure 8-5: Distribution diagram of each specific AFC pack in the prototype blade

from that plot, the 10 Hz response is consistently lower than the corresponding 1 Hz one. This was expected based on a lower free strain response of the AFC packs with higher excitation frequency. Table 8.3 presents the twist rate for the spar alone and for the complete blade obtained from experimental measurements and from the model predictions (taking into account the five failed packs). The addition of the fairing had a small effect on the measured actuation level (~10% decrease), which indicates that the additional torsional stiffness (~17%) that comes along with the inclusion of the fairing is compensated by an increase in the twist actuation moment. As one can also see, the model overpredicted the actuation levels by a significant margin. Most of it can be associated with the fact that the predictions are based on linearized piezoelectric constants experimentally obtained at high fields (when 4,000 V_{pp} is used). The known nonlinear piezoelectric response as function of the electric field will result in a lower effective d_{11} then the value reported in Table C.1 (Appendix). However, the AFC packs used were not characterized for that and the

Table 8.3: Twist actuation of the ATR prototype blade (°/m, 2,000 V_{pp}/0 V_{DC})

	Model prediction	Experiments
Spar only	2.0	1.1
Spar + fairing	1.8	1.0

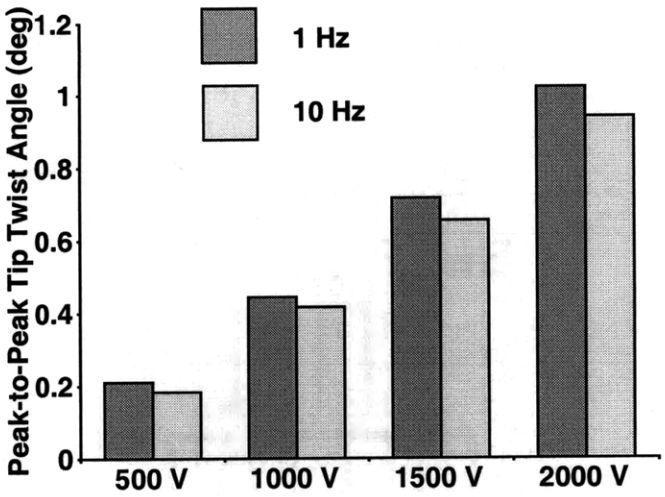


Figure 8-6: Actuation results of the ATR prototype blade having only 19 out of the 24 AFC packs working (voltage levels are peak-to-peak, no DC offset)

data are, therefore, not available.

Other contribution to the actuation error was already identified when predicting the torsional stiffness. Since the active twist rate is directly related to the torsional warping, similar problem found for the stiffness is reflected here (for example, the effects of the foam core that are neglected in the analysis). VABS is being upgraded to calculate the actuation strain constants, and will be a more realistic analysis tool. It is worth noting that the thin-walled multi-cell analysis formulation established in this study (Chapters 2 and 3 and [33]) has been validated previously against other experiments, showing a reasonably good correlation. The level of discrepancy here is way beyond previously found and may indicate a potential AFC pack delamination from the composite laminate. No experimental evidence (other than the questioning above) has been found, and further non-destructive evaluation (NDE) tests will be performed. Finally, a typical twist actuation response for the ATR prototype blade is presented in Fig. 8-7.

8.5 Frequency Response Test

In order to obtain the dynamic characteristics of the prototype blade, such as a transfer function, frequency responses were obtained by applying sinusoidal high voltages

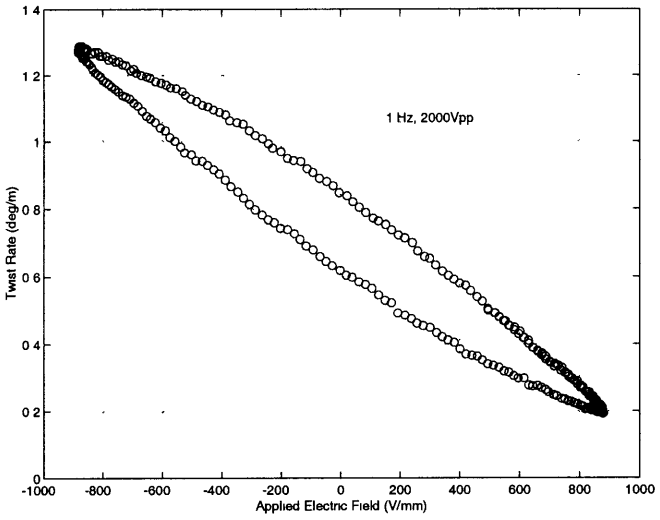


Figure 8-7: ATR prototype blade tip twist response as function of applied electric field (no DC offset)

into the AFC packs and monitoring the strain gauges embedded or measuring tip twist. These tests were performed at NASA Langley due to the limitations on the available high-voltage amplifiers at MIT.

At first, the strain gauge readings were recorded during the excitation voltage variation of the twist actuation (see Fig. 8-8). The first torsional mode was found to be around 85 Hz, and this result matches well with the model prediction. The flapping bending gauges also showed a great deal of bending-torsion coupling at the same frequency, although it showed small peaks around the expected flapping bending natural frequencies (actuation of the remaining 19 AFC packs caused non-symmetric response).

The dynamic tip twist actuation was measured while applying the same sinusoidal pattern but the with smaller voltage amplitude (see Fig. 8-9). Even at a low electric fields, the dynamic twist response of the prototype blade increases a lot around the first torsional natural frequency. This increase results from resonance, and it signifies that there is a potential possibility of large dynamic response around the natural frequencies of the blade. It will be investigated in future experiments whether such an increase in dynamic response can be used to beneficially influence the blade behavior or not.

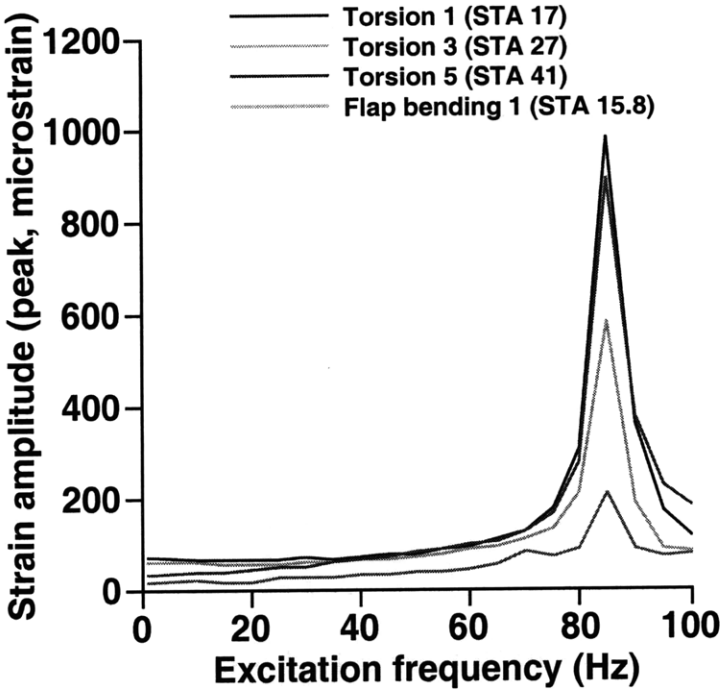


Figure 8-8: ATR prototype blade bench response of embedded strain gauges vs. AFC excitation frequency

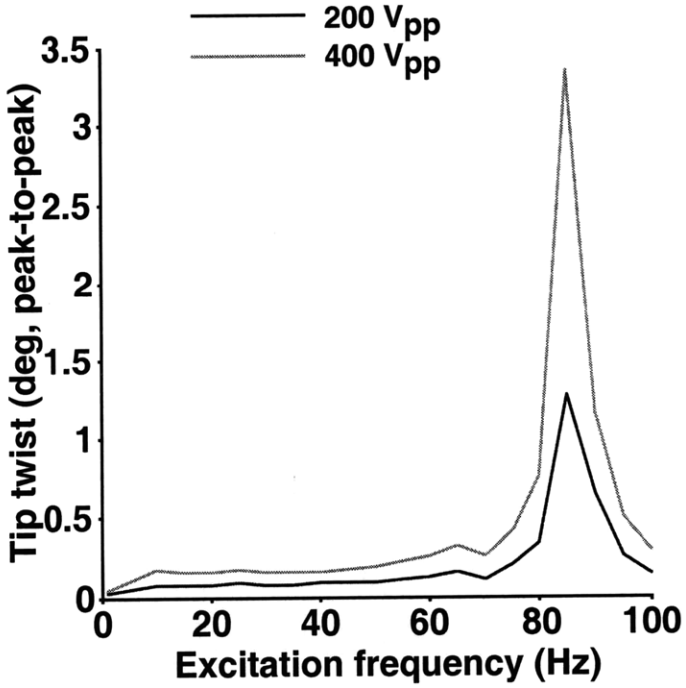


Figure 8-9: ATR prototype blade bench tip twist actuation response vs. AFC excitation frequency

Chapter 9

Conclusions and Recommendations

9.1 Summary

This thesis presents the use of anisotropic piezoelectric twist actuation of a helicopter rotor blade as a potential mechanism to accomplish individual blade control for vibration or noise reduction. The suggested structural modeling, design, manufacturing, and preliminary bench test results of the prototype blade will serve as the basis for further development of the desired aeroelastic research system composed of a four-bladed fully articulated rotor for wind-tunnel tests, with each blade being integrally twisted by direct strain actuation. This is accomplished by distributing embedded piezoelectric active fiber composites along the span of the blades.

This thesis has addressed several issues related to the ATR blade research, which are:

1. Development of a design framework for an active multi-cell rotor blade
2. Investigation of actuation trend by changing the ply lay-up in the two-cell active rotor blade in order to draw a maximum twist actuation
3. Design and optimization of the ATR prototype blade for a set of requirements and goal
4. Manufacturing procedure of the ATR prototype blade

5. Non-rotating test of the ATR prototype blade and identification of potential performance degradation sources

The framework proposed for integrally twisted rotor blade design proved to be very suitable. The two-cell thin-walled active beam model developed in this thesis shows good agreement with other models and experimental data. However, it also turns out that this model has limited capabilities upon handling rather complicated structures, such as thick-walled beam, miscellaneous elements like ballast weights, foam cores. The test results indicate that it is also required to include to the analysis the non-linear characteristics of the active material.

The actuation trend of the multi-cell active rotor blade was studied by examining the developed formulation, and verified by conducting a number of numerical examples. Such a trend study was directly beneficial to the iterative task of the ATR blade design, especially with regard to the twist actuation versus the lay-up design of each wall.

Before entering the full-extent design stage, the requirements for the ATR prototype blade were established by considering both the general requirements to the model-scaled helicopter rotor blade and the specific ones to the current active blade. An appropriate design flowchart was also organized to access the process systematically and efficiently.

ATR prototype blade design started with the selection of several different candidate concepts. The analyses were conducted using the model developed, and each candidate was checked against the requirements. At the same time, further aspects such as manufacturing complexity and cost-effectiveness of active material were also considered. Once the final design was determined, more modifications were added in order to make the manufacturing easier and more practical.

Several structural elements in the prototype blade needed to be modified or designed in addition to the skin lay-up, for example, blade root, AFC packs, the ballast weights, etc. To verify their design and performance, two testing articles were fabricated before the full-span prototype was manufactured. These testing articles were also used to define the manufacturing procedure. The final prototype was successfully

completed, even though it still presented a few manufacturing difficulties.

The prototype blade and the testing articles were tested in order to see if they satisfied the design requirements and to extract the mechanical characteristics of the blade for correlation with the model prediction. Various tests were conducted, such as tensile test, torsional stiffness measurement, bench twist actuation test, and frequency response test.

9.2 Conclusions

A number of conclusions can be drawn from the current ATR blade research, and they are summarized as follows.

- The framework of an active multi-cell active blade proposed in this thesis proved to be appropriate in the current ATR blade design.
- The analytical model established in the present thesis showed an appropriate degree of agreement with the other models and the experimental data. However, refinements are desirable due to its limited capability to handle the core material and the ballast weights, along with piezoelectric nonlinearities.
- The actuation trend of multi-cell active rotor blade turned out to be different from the estimated behavior considering a single-cell model. The correct behavior from the current multi-cell model should be reflected in the design process, and as a result, an optimized ATR design can be obtained.
- The final selected ATR blade design meets the requirements, and also features a manufacturing simplicity and efficient use of active material (including cost).
- Tensile test proved that the structural design, especially the new integral blade root, is so that the blade can withstand the combination of centrifugal load and the external aerodynamic load expected in the worst loading condition.

- Experimental structural characteristics of the prototype blade compare well with design goals, and modeling predictions correlate fairly with experimental results.

- Preliminary bench actuation tests show lower twist performance than that originally expected, and are due to electric failure of the active fiber composite actuators at high electric fields. A maximum twist of 1.5°/m (peak-to-peak) was reached at half of the operating voltage while all the actuators were working. The electric breakdown of the actuators is under intensive investigation at MIT and more tests need to be conducted on specially designed active coupons to narrow down the causes of failure under these circumstances.

9.3 Recommendations

From the effort to solve the remaining problems encountered during this study, some recommendations follow, which will be beneficial to improve future active rotor blade development.

- Refinement of the present multi-cell active beam model is recommended since a significant discrepancy was found between the model prediction and the experimental data acquired in torsional stiffness measurement. This discrepancy was caused from the neglect of the foam cores and the ballast weights in the current model. On the other hand, VABS showed a more realistic estimation than the present model. Therefore, VABS can used as a reference to correlate further refinement of the current model.

- More precise characterization of the AFC packs at different levels of electric field is recommended. This information should be incorporated in the analytical model, improving the simple linear estimation from high electric field used in the present analysis. This simplification is regarded as one of the major factors responsible for the discrepancy in the twist actuation results between model estimation and experiments.

- Identification of the electric breakdown of the AFC packs is required, which happened when they are embedded into the blade assembly. Along with the effort of failure identification, an improvement of the AFC material and its manufacturing procedure is recommended. The selection of bonding agent and its curing cycle should be clearly established in terms of the structural integrity of AFC.

- Attachment of the flexible circuit to the spar assembly caused the chordwise deflection, which made the subsequent process harder associated with fairing fabrication. Use of room temperature curing epoxy is recommended to avoid this problem.

- It is desirable to use the ATR prototype blade as a preliminary testing article for hover testing with three other dummy passive blades. From this test, the ATR performance can be fully evaluated, and its dynamic characteristics identified. Twist actuation will be commanded, and the effectiveness of vibration reduction will be assessed. A detailed listing of such tasks suggested by NASA Langley Research Center is presented on Table 9.1. Once all the tests are successfully done, the ATR prototype blade will clear the way for the manufacturing of four new blades to be used for further studies.

Table 9.1: Hover test plan for the ATR prototype blade (TDT at Langley)

Task description	Method	Frequency	RPM	Collective	C_T/σ
In Air/Heavy Gas/Vacuum					
• Non-rotating					
- Static actuation check	Quasi-static	0	0	0	0
- Actuation vs. frequency	Sine dwell	0,1,2,...,10P	0	0	0
- Frequency response	Sine sweep	0-10P	0	0	0
• Track and balance					
• Rotating					
- Actuation vs. frequency	Sine dwell	0,1,2,...,10P	0-Ω_o	$\leq$ 10 deg.	$\leq$ 0.100
- Frequency response	Sine sweep	0-10P	0-Ω_o	$\leq$ 10 deg.	$\leq$ 0.100

Appendix A

Cross-Sectional Formulation

Explicit expressions of the two-cell thin-walled active beam cross-sectional model shown in Chapter 2 are provided for some of the relevant variables used in the development, including the stiffness coefficients K_{ij} which have some corrections from the original expressions presented in [20]:

$$
\begin{aligned}
K_{11} &= \oint (A - \frac{B^2}{C})\, ds - 4a_3 \oint_I \frac{B}{C}\, ds - 4a_4 \oint_{II} \frac{B}{C}\, ds \\
K_{12} &= 4a_1 \oint_I \frac{B}{C}\, ds + 4a_2 \oint_{II} \frac{B}{C}\, ds \\
K_{13} &= -\oint (A - \frac{B^2}{C}) z\, ds - 4a_7 \oint_I \frac{B}{C}\, ds - 4a_8 \oint_{II} \frac{B}{C}\, ds \\
K_{14} &= -\oint (A - \frac{B^2}{C}) y\, ds - 4a_3 \oint_I \frac{B}{C}\, ds - 4a_4 \oint_{II} \frac{B}{C}\, ds \\
K_{22} &= -4a_1\, A_{eI} - 4a_2\, A_{eII} \\
K_{23} &= 4a_7\, A_{eI} + 4a_8\, A_{eII} \\
K_{24} &= -4a_5\, A_{eI} - 4a_6\, A_{eII} \\
K_{33} &= \oint (A - \frac{B^2}{C}) z^2\, ds + 4a_7 \oint_I \frac{B}{C} z\, ds + 4a_8 \oint_{II} \frac{B}{C} z\, ds \\
K_{34} &= -\oint (A - \frac{B^2}{C}) yz\, ds - 4a_5 \oint_I \frac{B}{C} z\, ds - 4a_6 \oint_{II} \frac{B}{C} z\, ds \\
K_{44} &= \oint (A - \frac{B^2}{C}) y^2\, ds + 4a_5 \oint_I \frac{B}{C} y\, ds + 4a_6 \oint_{II} \frac{B}{C} y\, ds
\end{aligned}
$$

where

$$
\begin{aligned}
a_1 &= -\frac{c_3}{c_1} \\
a_2 &= \frac{(b_1+b_2)a_1+b_4}{b_2} \\
a_3 &= -\frac{c_2}{c_1} \\
a_4 &= \frac{(b_1+b_2)c_4+b_3}{b_2} \\
a_5 &= \frac{b_5 \oint_I by\ ds + b_2 d_1}{e_1} \\
a_6 &= \left(\frac{b_1+b_2}{b_2}\right) d_3 - \frac{\oint_I by\ ds}{b_2} \\
a_7 &= \frac{b_5 \oint_I bz\ ds + b_2 d_2}{e_1} \\
a_8 &= \left(\frac{b_1+b_2}{b_2}\right) d_4 - \frac{\oint_I bz\ ds}{b_2}
\end{aligned}
$$

and

$$
\begin{aligned}
b &= -2\frac{B(s)}{C(s)} \\
b_1 &= 4\int_0^{s_1} c(s)\ ds \\
b_2 &= 4\int_{s_1}^{s_2} c(s)\ ds \\
b_3 &= \oint_I b(s)\ ds \\
b_4 &= -2A_{eI} \\
b_5 &= 4\int_{s_2}^{s_3} c(s)\ ds \\
b_6 &= \oint_{II} b(s)\ ds \\
b_7 &= -2A_{eII}
\end{aligned}
$$

$$
\begin{aligned}
c &= -2\frac{1}{C(s)} \\
c_1 &= b_1 + \frac{(b_1+b_2)b_5}{b_2}
\end{aligned}
$$

$$
\begin{aligned}
c_2 &= b_3 + b_6 + \frac{b_3 b_5}{b_2} \\
c_3 &= b_4 + b_7 + \frac{b_4 b_5}{b_2}
\end{aligned}
$$

$$
\begin{aligned}
d_1 &= \oint_{I+II} by \; ds \\
d_2 &= \oint_{I+II} bz \; ds \\
d_3 &= \frac{b_5 \oint_I by \; ds + b_2 d_1}{e_1} \\
d_4 &= \frac{b_5 \oint_I bz \; ds + b_2 d_2}{e_1}
\end{aligned}
$$

$$
e_1 = b_1 b_2 + (b_1 + b_2) b_5
$$

Appendix B

1-D Blade Formulation

Considering the expressions of the element functions [22] presented in Eq. (2.34) and modification due to the inclusion of the piezoelectric forcing vector, one may write the inverse of the constitutive relation, Eq. (2.31), as follows:

$$\begin{Bmatrix} \gamma \\ \kappa \end{Bmatrix} = \begin{bmatrix} r & t \\ t^T & s \end{bmatrix} \begin{Bmatrix} F_B + F_B^{(a)} \\ M_B + M_B^{(a)} \end{Bmatrix}$$

The modified element functions become:

$$\begin{aligned}
f_{\psi_i} &= -C^T C^{ab} M_i - \frac{\Delta l_i}{2} C^T C^{ab} \cdot [e_1 + \{r(F_i + F_i^{(a)}) \widetilde{+ t}(M_i + M_i^{(a)})\}] F_i + \dots \\
f_{F_i} &= u_i - \frac{\Delta l_i}{2} [C^T C^{ab} \cdot (e_1 + \{r(F_i + F_i^{(a)}) + t(M_i + M_i^{(a)})\}) - C^{ab} e_1] \\
f_{M_i} &= \theta_i - \frac{\Delta l_i}{2} (\Delta + \frac{\tilde{\theta}_i}{2} + \frac{\theta_i \theta_i^T}{4}) C^{ab} \cdot \{t^T (F_i + F_i^{(a)}) + s(M_i + M_i^{(a)})\} \\
f_{\psi_{i+1}} &= C^T C^{ab} M_i - \frac{\Delta l_i}{2} C^T C^{ab} \cdot [e_1 + \{r(F_i + F_i^{(a)}) \widetilde{+ t}(M_i + M_i^{(a)})\}] F_i + \dots \\
f_{F_{i+1}} &= -u_i - \frac{\Delta l_i}{2} [C^T C^{ab} \cdot (e_1 + \{r(F_i + F_i^{(a)}) + t(M_i + M_i^{(a)})\}) - C^{ab} e_1] \\
f_{M_{i+1}} &= -\theta_i - \frac{\Delta l_i}{2} (\Delta + \frac{\tilde{\theta}_i}{2} + \frac{\theta_i \theta_i^T}{4}) C^{ab} \cdot \{t^T (F_i + F_i^{(a)}) + s(M_i + M_i^{(a)})\}
\end{aligned}$$

Appendix C

Material Properties

The following two tables present the material properties of the structural constituents of the ATR prototype blade.

Table C.1: Properties of the AFC packs

Thickness	203.2 μm
Density	4,060 kg/m^3
d_{11}*	309 pm/V
d_{12}*	-129 pm/V
E_L	30.18 GPa
E_T	14.91 GPa
ν_{LT}	0.454 GPa
G_{LT}	5.13 GPa

$*$ based on high-field linearization

Table C.2: Properties of the composite materials used in the ATR protype blade

	E-Glass	**S-Glass**	**Graphite IM7** (root)
Resin	F-155	SP-381	SP-381
Weave	Fabric	Uni-tape	Uni-tape
Thickness (μm)	114.3	228.6	139.7
Density (kg/m^3)	1,700	1,850	1,550
E_L (GPa)	19.3	43.4	14.2
E_T (GPa)	19.3	12.0	8.3
ν_{LT}	0.148	0.28	0.34
G_{LT} (GPa)	4.1	3.6	4.9

Table C.3: Capacitance history of the AFC packs

Pack No.	after poling	before spar cure	after spar cure	after flex circuit attaching	after first failure	after fairing cure
1	3.03	3.25	3.08	2.56	2.48	2.53
2	2.50	2.67	2.57	2.26	2.29	2.33
3	3.30	3.67	3.31	2.55	2.54	2.62
4	2.69	2.92	2.76	1.77	1.76	1.92
5	2.99	3.10	2.93	1.86	1.88	1.91
6	3.30	-	3.26	2.66	2.84	2.83
7	3.07	3.25	3.03	2.62	2.77	2.84
9	3.24	3.58	3.21	2.49	2.52	-
10	2.74	2.93	2.71	2.46	2.51	2.52
11	2.91	3.15	2.88	2.70	2.77	2.75
12	3.25	3.65	3.12	2.86	3.08	3.06
13	2.46	2.65	2.54	1.69	1.69	1.73
14	2.71	2.98	2.63	2.27	2.18	2.24
15	2.80	3.05	2.85	2.61	2.31	-
16	2.28	2.54	2.33	1.85	1.88	1.92
17	2.58	2.98	2.56	2.37	2.33	-
18	2.56	2.86	2.53	2.26	2.34	2.39
19	2.80	3.10	2.73	2.60	2.53	2.56
20	2.29	2.40	2.33	2.16	2.13	2.17
21	2.55	2.80	2.60	2.40	2.35	2.35
25	2.20	2.40	2.20	2.02	2.35	2.11
26	2.41	2.60	2.45	1.97	2.02	-
27	2.60	2.65	2.67	2.38	2.35	2.38
28	2.19	2.40	2.33	1.86	1.98	2.01

Appendix D

Detailed Dimensions of the ATR Prototype Blade

Table D.1: Part list of ATR prototype blade lay-up

Part name	**Type**	**Length** (inches)	**Width** (inches)	**Orientation**	**Remark**
Nose S-Glass	S-Glass	48.13	0.4916	0°	
Forward wrap	Adhesive film	42.5	4.153		Front tantalum weights wrapping
E-Glass 1	E-Glass	48.13	3.9126	0°/90°	See Fig. D-5.
E-Glass 2	E-Glass	48.13	3.8658	+45°/ − 45°	See Fig. D-5.
E-Glass 3	E-Glass	48.13	3.8542	0°/90°	See Fig. D-5.
Web 1	E-Glass	48.13	0.7773	0°/90°	
Web 2	E-Glass	48.13	0.7594	0°/90°	
Fairing top	E-Glass	42.5	2.5671	0°/90°	
Fairing bottom	E-Glass	42.5	2.5671	0°/90°	
Filling plies	S-Glass			+45°/ − 45°	See Fig. D-6.
Filling core	Foam	5.63	2.126		0.175 inch-thick plate-shape between two root stacks

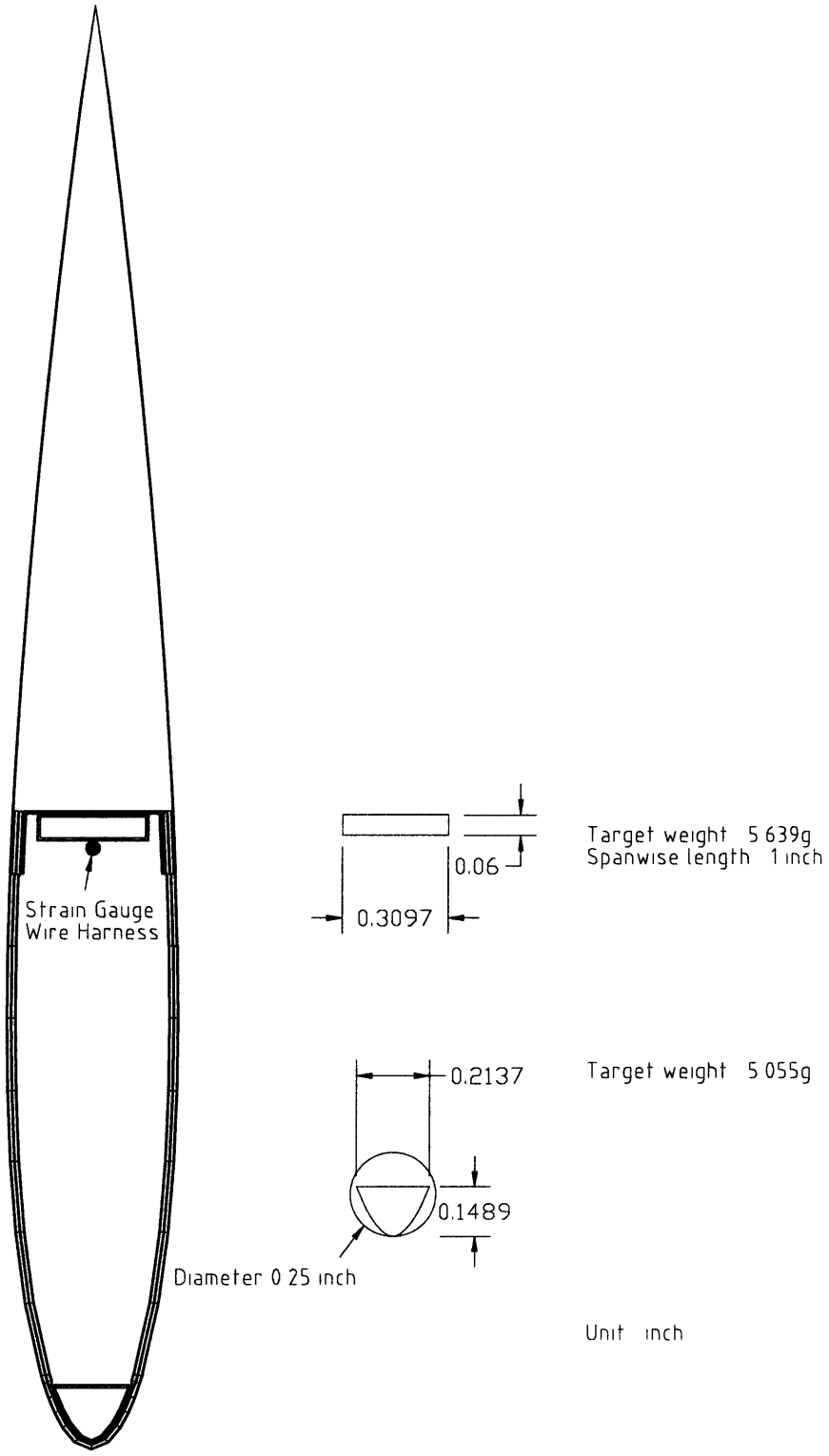


Figure D-1: Cross-section schematic of the ATR blade and the dimension of the ballast weights

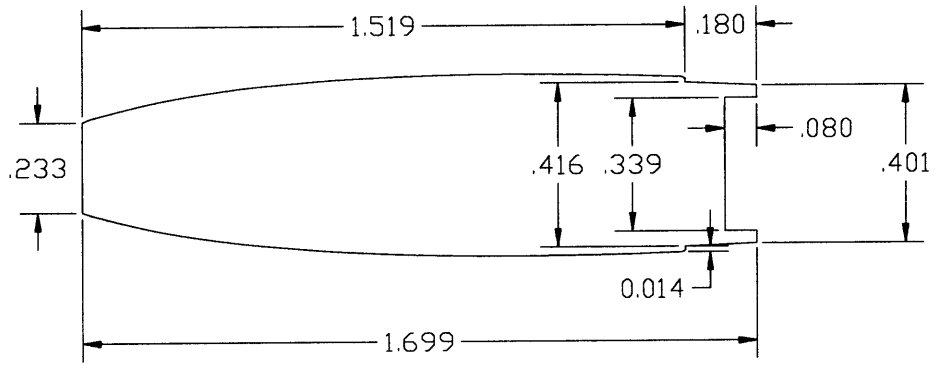


Figure D-2: Cross-section schematic of the front spar foam core (dimensions include oversize)

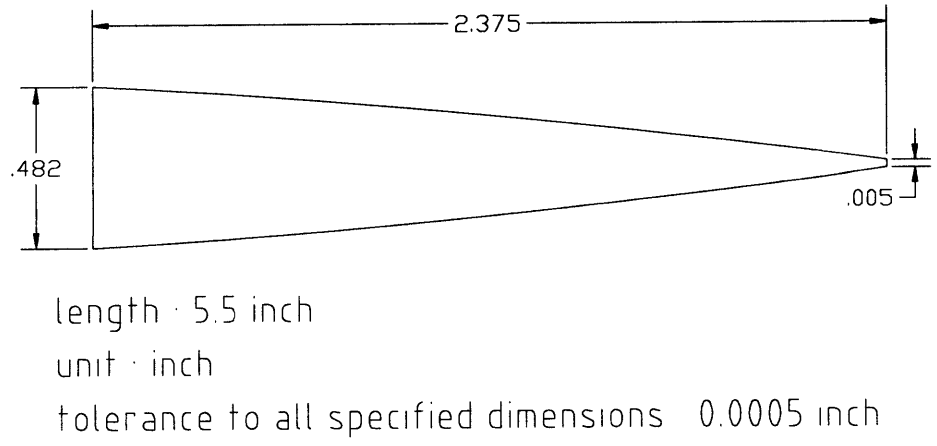


Figure D-3: Cross-section schematic of the fairing foam core (dimensions include oversize)

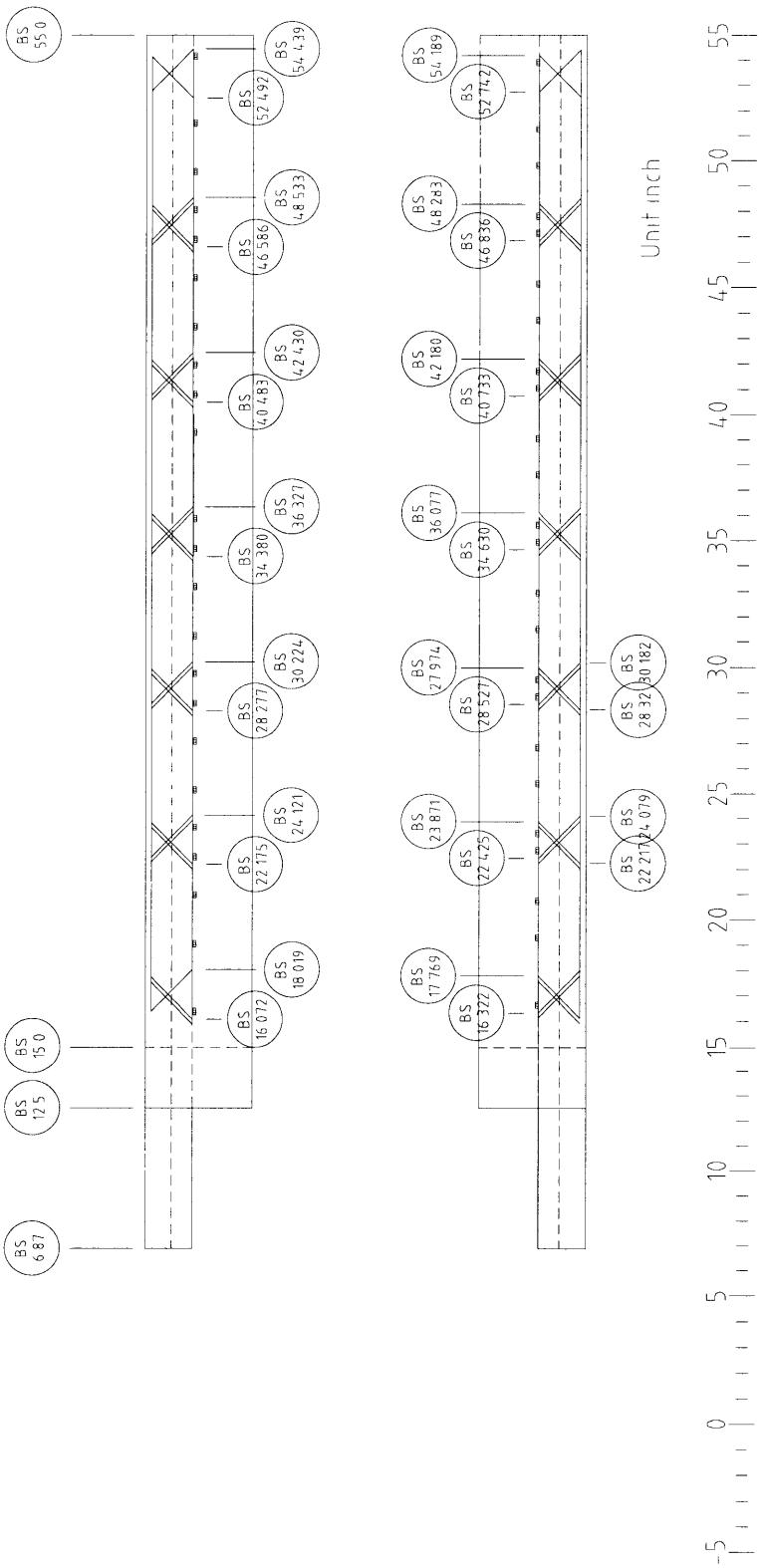


Figure D-4: Spanwise distribution of the 24 AFC packs at the top and bottom surface of ATR prototype blade

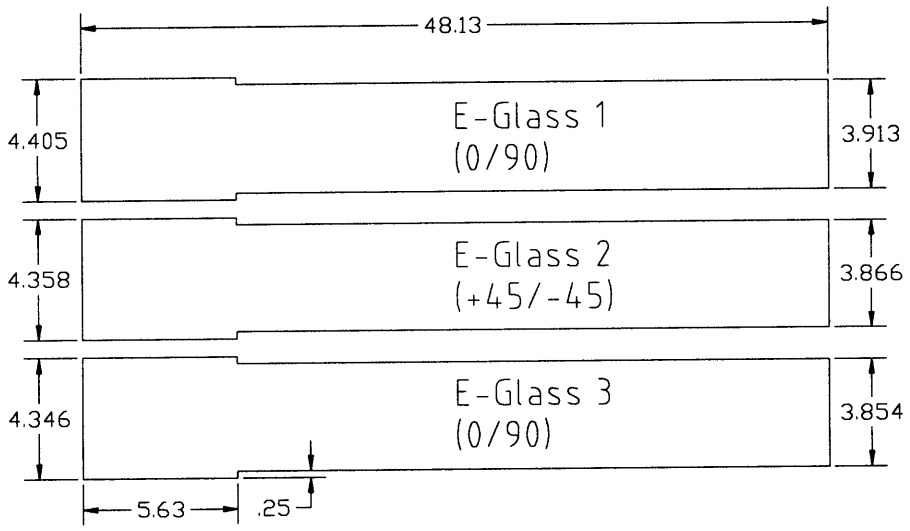


Figure D-5: Drawing of the three E-Glass skin plies which cover the whole span (all dimensions are in inches)

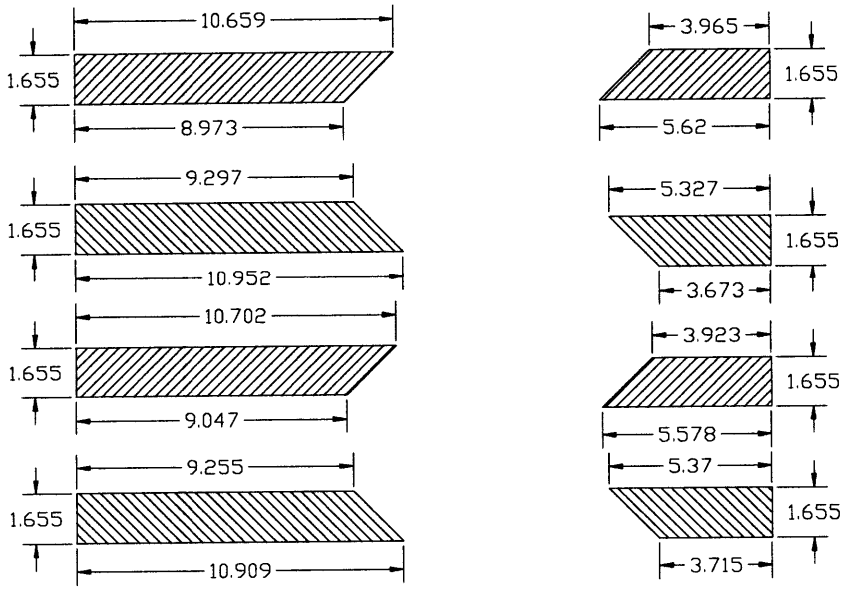


Figure D-6: Drawing of the auxiliary S-Glass pieces which fill the gap between inboard/outboard end and the first/last AFC pack space (all dimensions are in inches)

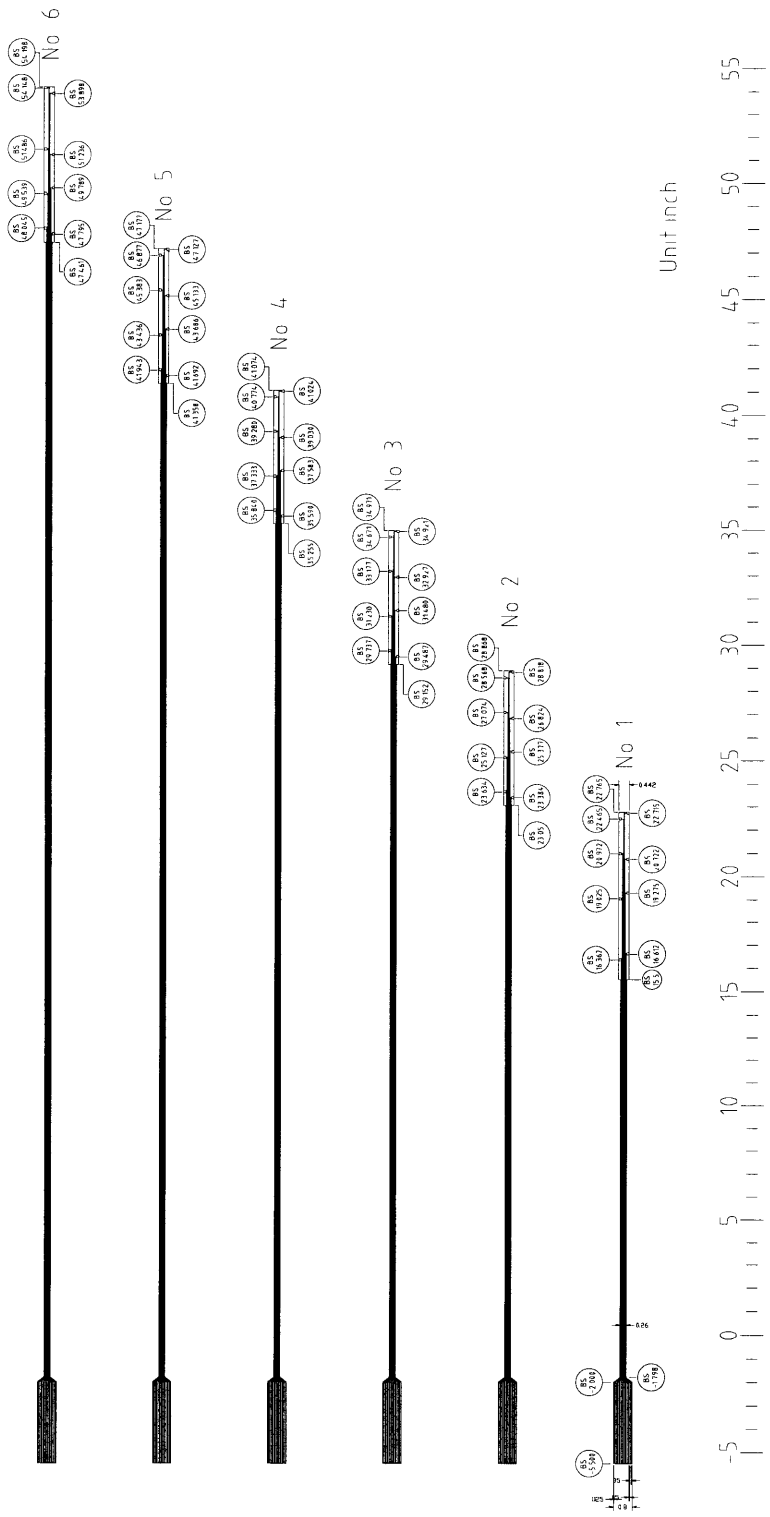


Figure D-7: Drawing of six-layer flexible circuit showing the location of each solder pads

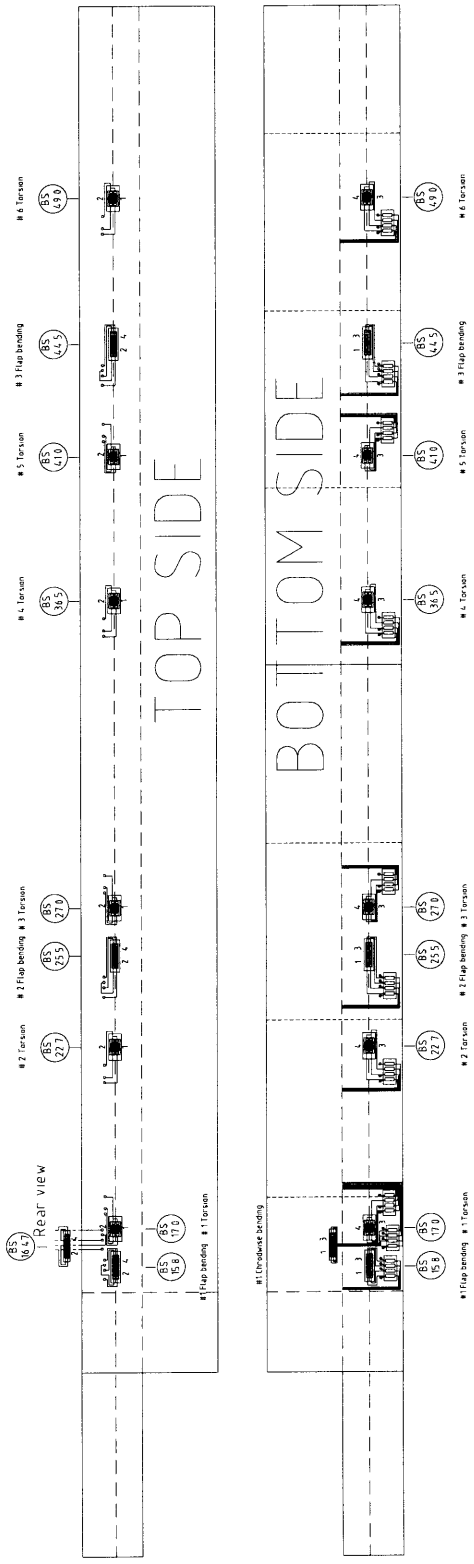


Figure D-8: Location of the strain gauge bridges along the span of ATR prototype blade

Appendix E

Activities Listing of the Prototype Blade Manufacturing

1. **Front spar manufacturing**

   - Fabrication of front spar foam cores
   - Machining trough for accommodating rear tantalum weights and strain gauge wires
   - Drying procedure of foam cores
   - Bonding 5–6 pieces and root plate of foam cores
   - Preparation of strain gauge bridge
   - Attaching strain gauges and wires
   - Checking strain gauges (resistance and dynamic behavior)
   - Checking AFC pack (capacitance and strain performance)
   - Checking flexible circuit (high voltage)
   - Cutting blade root plies and stack lay-up
   - AFC pack preparation for lay-up (cleaning flap and initial bending)
   - Cutting front spar plies and lay-up
   - Preparation of blade mold (cleaning, release agent, aluminum strip)

- Sealing of blade mold
- Spar cure
- Trimming the extra extruded plies
- Removing extra resin from AFC flap
- Connecting high voltage wires to flexible circuit and testing
- Attaching flexible circuit to spar assembly
- Checking the connection between AFC flap and flexible circuit (capacitance)
- Torsional stiffness measurement and twist actuation test of active spar

2. **Fairing manufacturing**

- Fabrication of fairing cores
- Drying procedure of foam cores
- Bonding 5–6 pieces of foam cores
- Cutting fairing plies and lay-up
- Preparation of blade mold (cleaning, release agent)
- Sealing of blade mold
- Fairing cure
- Trimming the extra extruded plies
- Torsional stiffness measurement and twist actuation test of active blade
- Trimming the extra length at tip

Bibliography

[1] R. G. Loewy. Helicopter vibrations: A technological perspective. *Journal of the American Helicopter Society*, 29(4):4–30, 1984.

[2] P. P. Friedmann. The promise of adaptive materials for alleviating aeroelastic problems and some concerns. In *Proceedings of Innovation in Rotorcraft Technology*, pages 10.1–10.16, London, United Kingdom, June 24–25 1997. Royal Aeronautical Society.

[3] R. Bielawa. *Rotary Wing Structural Dynamics and Aeroelasticity.* American Institute of Aeronautics and Astronautics, 1992.

[4] R. G. Loewy. Recent developments in smart structures with aeronautical applications. In *Proceedings of the 37th Israel Annual Conference on Aerospace Sciences*, February 26–27 1997.

[5] J. P. Rodgers, N. W. Hagood, and D. B. Weems. Design and manufacture of an integral twist-actuated rotor blade. In *Proceedings of the 38th AIAA Structures, Structural Dynamics, and Materials Conference*, Kissimmee, Florida, 1997. AIAA Paper No. 97–1264.

[6] J. P. Rodgers and N. W. Hagood. Hover testing of a 1/6th Mach-scaled CH-47D blade with integral twist actuation. In *Proceedings of the 9th International Conference on Adaptive Structures and Technologies*, Cambridge, Massachusetts, October 14–16 1998.

[7] A. A. Bent and N. W. Hagood. Piezoelectric fiber composites with interdigitated electrodes. *Journal of Intelligent Material Systems and Structures*, 1996.

[8] P. C. Chen and I. Chopra. A feasibility study to build a smart rotor: Induced-strain actuation of airfoil twisting using piezoceramic crystals. In *Proceedings of the Society of Photo-Optical and Instrumentation Engineers*, pages 238–254, San Diego, California, Vol. 1917 1993.

[9] I. Chopra and P. C. Chen. Hover testing of smart rotor with induced-strain actuation of blade twist. *AIAA Journal*, 35(1):6–16, 1997.

[10] J. P. Rodgers, A. A. Bent, and N. W. Hagood. Characterization of interdigitated electrode piezoelectric fiber composites under high electrical and mechanical loading. In *Proceedings of the Society of Photo-Optical and Instrumentation Engineers*, San Diego, California, 1996.

[11] A. J. duPlessis and N. W. Hagood. Modeling and experimental testing of twist actuated single cell composite beams for helicopter blade control. AMSL 96-1, Massachusetts Institute of Technology, February 1996.

[12] O. Song and L. Librescu. Vibrational behavior of rotating helicopter blades incorporating adaptive capabilities. In *Proceedings of SPIE Smart Structures and Materials Conference*, Vol. 1917 1993.

[13] W. K. Wilkie, W. Belvin, and K. C. Park. Aeroelastic analysis of helicopter rotor blade incorporating anisotropic piezoelectric twist actuator. In *ASME 1996 World Congress and Exposition*, 1996.

[14] L. W. Rehfield. Design analysis methodology for composite rotor blades. In *Proceedings of the Seventh DoD/NASA Conference on Fibrous Composites in Structural Design*, Denver, CO, June 1985. Grant NAG-2-238.

[15] C. E. S. Cesnik and D. H. Hodges. VABS: a new concept for composite rotor blade cross-sectional modeling. *Journal of the American Helicopter Society*, 42(1):27–38, 1997.

[16] W. K. Wilkie. *Anisotropic Piezoelectric Twist Actuation of Helicopter Rotor Blades: Aeroelastic Analysis and Design Optimization.* PhD dissertation, University of Colorado, Department of Aerospace Engineering Sciences, December 1997.

[17] R. C. Derham and N. W. Hagood. Rotor design using smart materials to actively twist blades. In *Proceedings of the American Helicopter Society 52nd Annual Forum*, Washington, DC, June 4–6 1996.

[18] D. H. Hodges. A mixed variational formulation based on exact intrinsic equations for dynamics of moving beams. *International Journal of Solids and Structures*, 26(11):1253 – 1273, 1990.

[19] D. H. Hodges, X. Shang, and C. E. S. Cesnik. Finite element solution of nonlinear intrinsic equations for curved composite beams. *Journal of the American Helicopter Society*, 41(4):313–321, 1996.

[20] A. M. Badir. Analysis of two-cell composite beams. In *Proceedings of the 36th AIAA Structures, Structural Dynamics, and Materials Conferences*, pages 419–424, New Orleans, 1995. AIAA Paper No. 95-1208-CP.

[21] V. L. Berdichevsky. Variational-asymptotic method of shell theory construction. *PMM*, 43(4):664 – 687, 1979.

[22] X. Shang and D. H. Hodges. Aeroelastic stability of composite rotor blades in hover. In *Proceedings of the 36th Structures, Structural Dynamics and Materials Conference*, New Orleans, Louisiana, April 10 – 12 1995.

[23] B. Jaffe, W. R. Cook, and H. Jaffe. *Piezoelectric Ceramics.* Academic Press, New York, 1971.

[24] D. H. Hodges, A. R. Atilgan, C. E. S. Cesnik, and M. V. Fulton. On a simplified strain energy function for geometrically nonlinear behavior of anisotropic beams. *Composites Engineering*, 2(5 – 7):513 – 526, 1992.

[25] R. M. Jones. *Mechanics of Composite Materials.* Hemisphere, New York, 1975.

[26] V. L. Berdichevsky, E. A. Armanios, and A. M. Badir. Theory of anisotropic thin-walled closed-section beams. *Composites Engineering*, 2(5 – 7):411 – 432, 1992.

[27] C. E. S. Cesnik and S.-J. Shin. On the cross-sectional modeling of active helicopter blades. In *Proceedings of PACAM VI*, Rio de Janeiro, Brazil, January 4 – 8 1999.

[28] J. P. Rodgers and N. W. Hagood. Development of an integral twist-actuated rotor blade for individual blade control. AMSL 98-6, Massachusetts Institute of Technology, October 1998.

[29] L. W. Rehfield, A. R. Atilgan, and D. H. Hodges. Nonclassical behavior of thin-walled composite beams with closed cross sections. *Journal of the American Helicopter Society*, 35(2):42 – 50, 1990.

[30] V. Giavotto, M. Borri, M. Mantegazza, G. Ghiringhelli, V. Carnaschi, G. C. Maffioli, and F. Mussi. Anisotropic beam theory and applications. *Computers and Structures*, 16(1 – 4):403 – 413, 1983.

[31] Anonymous. Wind-tunnel model system criteria. LHB 1710.15, NASA Langley Research Center, May 1992.

[32] C. E. S. Cesnik, S.-J. Shin, W. K. Wilkie, M. L. Wilbur, and P. H. Mirick. Modeling, design, and testing of the NASA/ARMY/MIT active twist rotor prototype blade. In *Proceedings of the American Helicopter Society 55th Annual Forum*, Montreal, Canada, May 25–27 1999.

[33] C. E. S. Cesnik and S.-J. Shin. Structural analysis for designing rotor blades with integral actuators. In *Proceedings of the 39th AIAA Structures, Structural Dynamics, and Materials Conference*, Long Beach, California, April 20–23 1998. AIAA Paper No. 98–2107.

3421-5